Selection of Permanent Scatterer Candidates for Deformation Monitoring

Amplitude Calibration of ERS SLC SAR images

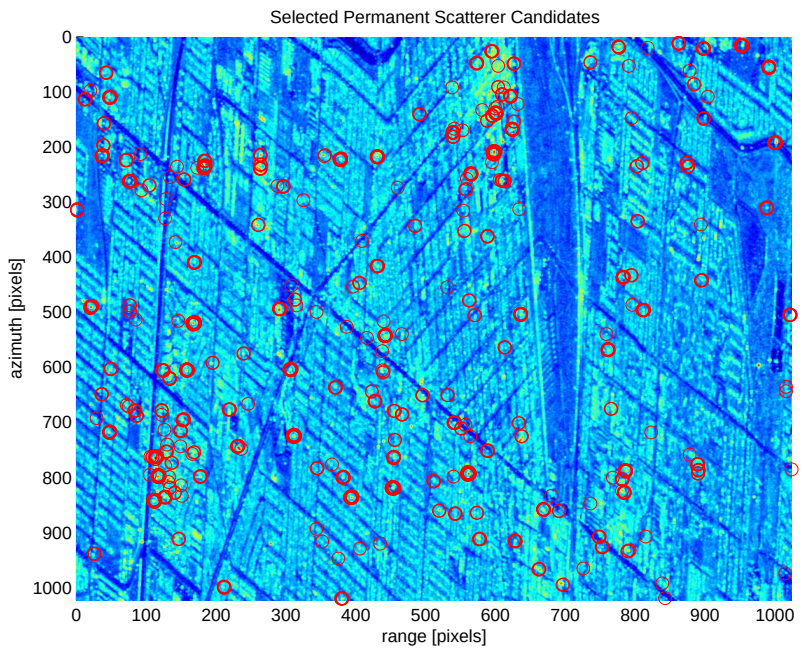

MSc. thesis

B.N. Cassee
September 2004

Section of Mathematical Geodesy and Positioning
Faculty of Civil Engineering and Geosciences
Delft University of Technology

Selection of Permanent Scatterer Candidates for Deformation Monitoring

Amplitude Calibration of ERS SLC SAR Images

Supervisors: Dr.ir. R.F. Hanssen
Ir. V.B.H. Ketelaar
Professor: Prof.dr.ir. P.J.G. Teunissen

MSc. thesis

B.N. Cassee
September 2004

Section of Mathematical Geodesy and Positioning
Faculty of Civil Engineering and Geosciences
Delft University of Technology

Preface

This thesis presents the results of the final research project of my study Geodetic Engineering, part of the faculty of Civil Engineering and Geosciences of the Delft University of Technology. During almost a year I have been working on the calibration of ERS SAR imagery, to enable the selection of permanent scatterer candidates from large time series of amplitude data. These selected points can be used in the permanent scatterer processing to provide deformation measurements of millimeter accuracy. As it was decided to stop the 5-year education program and sell the Geodesy building, I finished the last stage of my study at the building of the faculty of Aerospace Engineering, to which the section Mathematical Geodesy and Positioning, supervised by professor Peter Teunissen, moved last year.

I would like to thank many people who helped me during the realization of my thesis and research work. First of all, thanks go to my supervisors Ramon Hanssen and Gini Ketelaar for their useful advise and critical remarks on my work. Whenever there was a problem, they were always willing to help me solve it. I had the privilege to work amongst people who all work on radar topics. The new ideas and suggestions they gave me during the discussions in the weekly group meetings inspired me a lot. In special, I would like to thank Freek van Leijen and Gini Ketelaar, who helped a lot with the processing of the data. Furthermore, I would like to thank Ralph Cordey from ESA-ESTEC Noordwijk (Wave Interaction & Propagation Section) for providing articles and explanation on the ESA calibration method, and Bert Kampes for his help to adapt DORIS to obtain calibration parameters. Finally, thanks go to professor Teunissen for his remarks on my work, and to professor Klees and Ben Gorte, who were willing to be members of my graduation committee.

Bianca Cassee
Delft, 18 September 2004

Contents

Summary

Images acquired by Synthetic Aperture Radar (SAR) can be used to monitor deformation of the Earth's surface. Conventional techniques are based on combinations of two or three SAR images from different satellite passes. Interferometric processing, using phase differences, can provide deformation measurements with centimeter accuracy. Unfortunately, the accuracy of InSAR is limited by influences from atmosphere, and geometric and temporal decorrelation. To measure deformation with a smaller signal (mm/yr), another technique that uses long time series of radar acquisitions can be used. The processing of this technique, known as the permanent scatterer technique, is based on a set of points that show a high phase coherence over time: the permanent scatterer candidates (PSCs). However, the points that show a high phase coherence over an image time series, can only be assessed after estimation and removal of different phase contributors, as ,e.g., atmosphere and orbit inaccuracies. As the amplitude values are almost insensitive to most of the contributors, an initial set of PSCs is selected using time series analysis of amplitude data. Based on an analysis of amplitude statistics, scatterers with a high and stable amplitude over a large time interval are selected.

To perform a time series analysis of amplitude data, differences in amplitude between the images caused by, e.g., different satellite geometry or sensor characteristics have to be removed. which is performed by calibrating the SAR data. This study emphasizes on the question how calibration for ERS SAR imagery should be implemented in order to perform a selection of reliable permanent scatterer candidates.

Calibration is one of the preprocessing steps have to be performed before PSCs can be selected. First, the raw ERS SAR data needs to be processed to obtain complex SAR data. Subsequently, the SAR data are oversampled to avoid aliasing effects, and amplitude values are calculated from the complex data, followed by the amplitude calibration and coregistration of the SAR images. Coregistration parameters need to be determined very accurately to enable time series analysis of the amplitudes on pixel base. A set of PSCs with stable amplitude behavior over time is selected using the dispersion index D_A, which is defined as the ratio between the standard deviation and the mean of the amplitudes per pixel over time. Pixels with $D_A < 0.25$ are selected and marked as PSCs.

Two different calibration methods are implemented and tested. The *ESA calibration method* consists of several correction factors that have to be applied to the amplitude data. The factors for varying incidence angle, range spreading loss and antenna pattern gain vary with range direction. The correction for powerloss vary in range and azimuth direction, and the corrections for replica pulse power and calibration constant K are constant per image. Most of the ESA correction factors can be obtained from look-up tables that are derived from external calibration campaigns, and differ per sensor, and processing and acquisition date of the SAR images. As the overlap of the SAR images in range direction is maximum several km, the correction factors of the ESA calibration method that vary in range direction are not important for the calibration in this study. The variation of these correction factors between the images is low compared to the variation of the constant correction factors of the ESA method. The constant K has the most influence on reducing the differences in amplitude, especially between ERS-1 and ERS-2 imagery. Besides, if only the constant K is applied to the data, better results for the PSC selection are obtained than if all ESA calibration correction factors are applied. The best and fastest way to implement

the ESA calibration method for the calibration in this study is the restriction of the ESA method to only constant K.

The second calibration method is the *empirical calibration method*. This method calculates a constant calibration factor c_k per image from time series of amplitude data of an initial set of PSCs. These PSCs are selected from the oversampled SAR data, show stable amplitude behavior, and are Gaussian distributed ($D_A < 0.25$). The c_k values are calculated by taking the mean of the ratio between the amplitude values of all initial selected PSCs and their mean over the image time series. Next, all amplitude values whithin a image are scaled by the factor c_k. After the calibration a new set of PSCs is selected using again the threshold value of 0.25 on the dispersion index. The implementation of the empirical calibration method has two limitations. First, the calibration cannot be performed on one single SAR image, as the calibration factors c_k are calculated from time series of amplitude data. To ensure the reliability of the c_k calculation and the selection of PSCs a minimum number of images is required. Secondly, images that have high Doppler centroid frequencies should not be used in the empirical calibration method. These images appear to have much lower amplitude values than other SAR images, which will disturb the estimation of the c_k factors of other images.

To decide which of the implemented calibration methods, or elements of these methods, are most suitable for the calibration purpose of this study, - diminish the differences between the amplitude data of stacked images to enable time series analysis on amplitude data that are not influenced by different sensor characteristics or satellite geometry - , a crop of 2×10 km of Las Vegas of 48 SAR images is calibrated using both calibration methods. As the constant factors are the most important, it does not matter of which part of the image the crop is made: the tests results are representative for the entire image.

The ESA and empirically calibrated data sets and the derived sets of PSCs are compared using three criteria:

- *Detection rate of PSCs.*
  The detection rate is specified as the number of PSCs that are selected using a specific calibration method as a percentage from the total number of different PSCs selected from all data sets (oversampled raw, ESA and empirically calibrated data). The detection rate of PSCs after calibration should be as high as possible. As the selection of PSCs is based on pixels with low dispersion index ($D_A = \frac{\sigma_A}{\mu_A}$) the amplitudes per point scatterer over the image time series has to be stable.

- *False detection rate of PSCs.*
  The false detection rate is defined as the percentage of selected PSCs (based on amplitude data) that do not show a coherent phase behavior. The calibration method with the lowest false detection rate is preferred. If the false detection rate is low, more PSCs with a coherent phase behavior are selected that can be used in the permanent scatterer analysis, i.e., the selected PSCs are assumed to be more reliable.

- *Computation time.*
  The computation time of the calibration processing should be as low as possible.

Based on these criteria, the empirical calibration method appears to be the best method for the calibration in this study. First of all, the empirical calibration method shows the lowest *false detection rate*. Tests are performed by selecting points with stable amplitudes ($D_A < 0.25$) and from these PSCs, scatterers are selected that show coherent phase behavior (with a threshold of 0.75) by using a first version of a program to perform permanent scatterer analysis. Only 0.92% of the pixels that were marked as PSCs after the empirical calibration method did not show a coherent phase behavior (2.73% for the ESA calibration method). The selection based on the empirically calibrated data results in more reliable PSCs: more points show also a coherent phase behavior. Regarding the *computation time* it is obvious that the restricted ESA calibration method is faster, as the amplitude data is only multiplied by a constant factor using a look-up table. The empirical method takes more time, as it calculates the calibration factor

per image from the amplitude data. However, the most time consuming step is the oversampling of the complex SAR data. Improvement of this step in further research can lead to an important reduction of the total processing time to select PSCs.

Furthermore, the *detection rate of PSCs* is almost similar for the ESA and empirical calibration method (67.3% vs. 66.7%). Both calibration methods improve the detection rate of PSCs: the ESA method detects 30.3% and the empirical calibration method 29.1% more PSCs than before the images were calibrated, which indicates that calibration of ERS SAR imagery is crucial for the selection of PSCs. The empirical calibration method provides the most stable amplitude values over the image time series. The standard deviation of the mean of all PSCs over time is 0.49 dB. (cf. 0.99 dB for the ESA calibration method and 1.00 dB for the uncalibrated oversampled data). However, the scaling based on the ESA calibration method has a physical interpretation and is therefore more legitimate to use than a calculated scaling factor.

Summarized, assumed that there are enough images available that have low Doppler centroid frequencies, the empirical calibration method is the best method to use for the calibration to select PSCs. If this is not the case, the restricted ESA method should be used that contains only the constant calibration factor K.

In further research additional tests need to be performed to evaluate the effect the calibration methods have on non urban areas, as, e.g., agricultural fields, deserts or mountainous areas. Furthermore, the empirical calibration method should be improved to enable a critical analysis on the accuracy of this calibration method. Besides, improved versions of a program to perform permanent scatterer analysis needs to be applied to the data. In this study only a first version to analyze the phase behavior of the PSCs is used. If improved versions are used, more accurate information on the false detection rate, the criterion on which the reliability of the selected set of PSCs is based, can be derived.

Samenvatting

Beelden ingewonnen door Synthetic Aperture Radar (SAR) kunnen worden gebruikt om deformatie van het aardoppervlak te monitoren. Conventionele technieken zijn gebaseerd op combinaties van twee of drie SAR beelden van verschillende satellietoverkomsten. Interferometrische verwerking van deze beelden, gebruik makend van faseverschillen, kan deformatiemetingen verschaffen met een precisie op centimeter niveau. Helaas is de nauwkerigheid van InSAR beperkt door atmosferische invloeden en geometrische en temporele decorrelatie. Om deformatie van een kleiner signaal (mm/jaar) te meten kan een andere techniek worden toegepast, waarbij gebruik wordt gemaakt van lange tijdseries van radar beelden. Deze techniek, de permanent scatterer techniek, is gebaseerd op een set van punten met een hoge fase coherentie over tijd: de permanent scatterer candidates (PSCs). Deze punten met een hoge coherence kunnen alleen geselecteerd worden nadat een aantal effecten die een bijdrage leveren aan de fase waarneming zijn geschat en verwijderd, als bijvoorbeeld invloeden van de atmosfeer of baanonnauwkeurigheden. Daar de amplitude waarnemingen bijna ongevoelig zijn voor deze invloeden, wordt een tijdserie analyse van de amplitude data gebruikt om PSCs te selecteren. Met behulp van een statistische analyse van de amplitude data worden reflecties met een hoge en stabiele amplitude over een lang tijdsinterval geselecteerd.

Om een tijdserie analyse van amplitude data uit te voeren moeten de verschillen in amplitude tussen de beelden, veroorzaakt door bijvoorbeeld afwijkende satelliet geometrie of andere sensor eigenschappen, worden verwijderd. Dit wordt gedaan door de SAR beelden te calibreren. Dit onderzoek richt zich op de vraag hoe calibratie van ERS SAR beelden geïmplementerd moet worden om de selectie van betrouwbare 'permanent scatterer candidates' mogelijk te maken.

Calibratie is een van de voorbewerkingsstappen die uitgevoerd moeten worden voordat de PSCs geselecteerd kunnen worden. Ten eerste moet de ruwe ERS SAR data worden verwerkt tot complexe SAR data. Vervolgens moet de SAR beelden worden oversampled om aliasing effecten te voorkomen en worden amplitude waarden berekend van de complexe data. Daarna wordt de amplitude data gecalibreerd en gecoregistreerd. De coregistratie parameters dienen erg nauwkeurig te worden bepaald om een tijdserie analyse van de amplitude waarden op pixel niveau mogelijk te maken. Uiteindelijk kan een set van PSCs geselecteerd worden met behulp van de dispersie index D_A, gedefinieerd als de verhouding tussen de standaardafwijking en het gemiddelde van de amplitudes over de tijdserie van beelden. Pixels die voldoen aan $D_A < 0.25$ worden geselecteerd als zijnde PSCs.

Twee verschillende calibratiemethoden zijn geïmplementeerd en getest. De *ESA calibratiemethode* bestaat uit verschillende correctiefactoren die toegepast dienen te worden op de amplitude data. Deze factoren zijn de correcties voor veranderende invals hoek, 'range spreading loss', 'antenna pattern gain' (allen variërend in range richting), de correctie voor 'powerloss' (variërend in range en azimuth richting) en de constante correctiefactoren voor het gebruik van de 'replica pulse power' en de calibratie constant K. De meeste ESA correctiefactoren kunnen worden gehaald uit tabellen die zijn opgesteld naar aanleiding van externe calibratiecampagnes en verschillen per sensor, verwerkings en inwinningsdatum van de beelden. Daar de overlap tussen de SAR beelden in range richting maximaal een aantal km is, zijn de correctiefactoren van de ESA calibratiemethode die variëren in range richting niet belangrijk voor het doel van de calibratie in dit onderzoek. De variatie van deze correctiefactoren tussen de beelden is namelijk laag in vergelijking met

de variatie van de constante correctiefactoren. De constante K heeft de meeste invloed op de reductie van de verschillen tussen de SAR beelden, met name de verschillen tussen ERS-1 en ERS-2 beelden. Daarnaast levert de calibratie met alleen de calibratieconstant K betere resultaten voor de selectie van PSCs dan voor het geval wanneer alle ESA correctiefactoren worden gebruikt. De beste en snelste manier om de ESA calibratiemethode toe te passen voor de calibratie in dit onderzoek is de ESA methode te beperken tot alleen de calibratie constante K.

De tweede calibratiemethode is de *empirische calibratiemethode*. Deze methode berekent een constante calibratiefactor c_k per beeld uit tijdseries amplitude data van een initiële set PSCs, geselecteerd van oversampelde SAR data. Deze PSCs hebben een stabiele amplitude en zijn Gaussisch verdeeld ($D_A < 0.25$). De waarden voor c_k zijn berekend door het gemiddelde te nemen van de verhouding tussen de amplitude waarden van alle initiële PSCs en hun gemiddelde over de tijdserie van beelden. Alle amplitude waarden binnen het beeld worden geschaald met deze c_k factoren. Na de calibratie wordt een nieuwe set van PSCs geselecteerd op basis van dezelfde drempelwaarde voor de dispersie index van de gecalibreerde data. De implementatie van de empirische calibratiemethode heeft een tweetal beperkingen. Ten eerste kan de calibratie niet uitgevoerd worden op een enkel SAR beeld, omdat de calibratiefactoren c_k berekend worden uit tijdseries van amplitude data. Om de betrouwbaarheid van de c_k berekening en de selectie van PSCs te garanderen is een minimaal aantal beelden nodig. Daarnaast is het belangrijk dat beelden met een hoge 'Doppler centroid' frequentie niet worden opgenomen in de empirische calibratie methode. Deze beelden tonen namelijk veel lagere amplitude waarden dan de andere SAR beelden, die de schatting van de c_k factoren van andere beelden verstoren.

Om te kunnen beslissen welke van de geïmplementeerde calibratie methoden, of elementen van deze methoden, het meest geschikt zijn om toe te passen voor de het doel van de calibratie in dit onderzoek, - het verminderen van de verschillen tussen de amplitude data in series SAR beelden om een tijdserie analyse van amplitude data mogelijk te maken die niet beïnvloed wordt door afwijkende sensor eigenschappen of satelliet geometrie - , is een uitsnede van 2×10 km gemaakt van 48 SAR beelden van Las Vegas en vervolgens gecalibreerd met beide calibratiemethoden. Daar de constante correctiefactoren per beeld het meest belangrijk zijn, maakt het niet uit van welk deel van het SAR beeld de uitsnede gemaakt wordt. De testresultaten zijn representatief voor heel het beeld.

De ESA en empirisch gecalibreerde data sets en de geselecteerde sets met PSCs zijn vergeleken op basis van drie criteria:

- *'Detection rate' van PSCs.*
  De 'detection rate' is gedefinieerd als het aantal PSCs dat geselecteerd wordt met een bepaalde calibratie methode als percentage van het totaal aantal verschillende PSCs dat geselecteerd is uit alle datasets (oversampled raw, ESA and empirisch gecalibreerde data). De 'detection rate' van de PSCs na de calibratie moet zo hoog mogelijk zijn. Daar de selectie van PSCs gebaseerd is op pixels met een lage dispersie index ($D_A = \frac{\sigma_A}{\mu_A}$) dient de amplitude over de tijdserie van beelden stabiel te zijn.

- *'False detection rate' van PSCs.*
  De 'false detection rate' is gedefinieerd als het percentage geselecteerde PSCs (gebaseerd op amplitude data) dat geen coherent fase gedrag vertoont. De calibratiemethode met de laagste 'false detection rate' verdient de voorkeur. Indien de 'false detection rate' laag is worden meer PSCs met een coherent gedrag geselecteerd die gebruikt kunnen worden in de permanent scatterer analyse. Met andere woorden, de geselecteerde PSCs zijn betrouwbaarder.

- *Berekeningstijd.*
  De berekeningstijd van de calibration procedure dient zo laag mogelijk te zijn.

Naar aanleiding van deze criteria blijkt de empirische calibratiemethode de beste methode voor het doel van de calibratie in dit onderzoek. Ten eerste heeft de empirische calibratiemethode de laagste *'false*

detection rate'. Testresultaten hiervoor zijn verkregen door het vergelijken van het aantal geselecteerde punten die een stabiel amplitude gedrag vertonen ($D_A < 0.25$) met het aantal punten uit deze dataset die ook een coherent fase gedrag hebben (coherentie hoger dan 0.75). Hiervoor is een eerste versie van een programma gebruikt waarin permanent scatterers geanalyseerd worden. 0.92% van de pixels die aangeduid werden als zijnde PSCs na de empirische calibratiemethode vertoonden geen coherent fase gedrag (voor de ESA calibratiemethode was dit 2.73%). De selectie van PSCs uit de empirisch gecalibreerde data resulteert in een groter aantal betrouwbare PSCs: punten die ook coherent fase gedrag vertonen. Wat betreft de berekeningstijd is het duidelijk dat de beperkte ESA calibratiemethode sneller is, omdat de amplitude data alleen vermenigvuldigd wordt met een constante factor uit een tabel. De empirische calibratiemethode zal meer tijd vragen omdat in deze methode de calibratiefactor per beeld berekend wordt met behulp van de amplitude data. De meest tijdrovende stap is echter de oversampling van de complexe SAR data. Verbetering van deze stap in nader onderzoek kan tot een belangrijke afname van de totale berekeningstijd leiden.

Daarnaast kan geconcludeerd worden dat de *'detection rate of PSCs'* bijna gelijk is voor de ESA en empirische calibratiemethode (67.3% vs. 66.7%). Beide calibratie methoden zorgen voor een verbetering van de 'detection rate'. De ESA methode detecteert 30.3% meer PSCs en de empirische calibratiemethode 29.1% meer PSCs dan de calibratie van de beelden, wat aangeeft dat de calibratie van ERS SAR beelden is een onmisbare stap voor de selectie van PSCs. De empirische calibratie methode geeft de meest stabiele amplitude waarden over de tijdserie. De standaard afwijking van het gemiddelde van alle PSCs over tijd is 0.49 dB (ter vergelijking: 0.99 dB voor de ESA calibratiemethode en 1.00 dB voor de ongecalibreerde oversampelde data). Opgemerkt dient te worden dat de schaling van de ESA calibratiemethode een fysische interpretatie kent en het gebruik van de schaling beter onderbouwt is dan de schaling waarbij een calibratie factor berekend wordt.

Samengevat, verondersteld dat er genoeg beelden beschikbaar zijn met een lage 'Doppler centroid' frequentie, blijkt de empirische calibratiemethode de beste methode om toe te passen voor de selectie van PSCs. Indien dit niet het geval is dient de beperkte ESA methode met alleen de constante calibratie factor K gebruikt te worden.

Aanvullende tests in verder onderzoek moeten het effect aantonen van de calibratiemethoden te testen in niet-stedelijk gebied, als bijvoorbeeld in landbouwgebieden, woestijd of berggebied. Daarnaast dient de empirische calibratie methode verbeterd te worden om een kritische analyse uit te kunnen uitvoeren omtrent de nauwkeurigheid van de calibratiemethode. Het toepassen van verbeterde versies van programma's voor permanent scatterer analyse op de geselecteerde sets PSCs kan nauwkeurigere informatie geven over de 'false detection rate', het meest belangrijkste criterium om de betrouwbaarheid van de calibratiemethode en de selectie van PSCs af te leiden.

Chapter 1

Introduction

1.1 Motivation

Many different geodetic measurement techniques are available to study deformation of the Earth's surface with different levels of accuracy. One of these techniques is the interferometric processing of signals from Synthetic Aperture Radar (InSAR). Since the late eighties InSAR has been used to study and measure different deformation processes, such as deformation caused by volcanism or earthquakes, and land subsidence as a consequence of, e.g., oil and gas extraction or ground water flow. InSAR is a technique based on microwave pulses that are emitted by the SAR instrument, reflected at the Earth's surface and received again by the SAR antenna. The received signals consist of an amplitude value, a measure for the intensity of the reflection on Earth, and a phase, which contains information on the distance.

Conventional methods are based on combinations of two or three SAR images from different satellite passes. The phase differences are used as a measure of the deformation. This method, the so-called repeat-pass principle, is very suitable to monitor deformation patterns of several centimeters per year, but not for measuring deformation with a smaller signal (mm/yr). There are three important limitations that make it practically impossible to measure such a small deformation signal with conventional InSAR techniques (see, e.g., Colesanti et al. (2003) and Ferretti et al. (2001)). First, the signals are delayed when propagating through the *atmosphere*. Although radar signals are not hindered by clouds, they are in particular influenced by the variable distribution of water vapor in the atmosphere, which results in spatial varying errors in each SAR image up to several centimeters. Next, *geometrical decorrelation* introduces noise, caused by the different incidence angles that appear from different geometry of the signal path from the orbits to the same resolution cell on the ground, which limits the number of image pairs that can be used for interferometric applications. Besides, changing scatter characteristics per resolution cell with time, due to differences in the structure of the Earth's surface, causes temporal decorrelation. These *temporal decorrelation* effects often occur in strongly vegetated or agricultural areas and make most pixels in these areas useless for interferometry, as interferometry is based on the coherence between pixels.

Another technique to measure deformation uses long time series of radar acquisitions of all available data within a certain area. This technique, known as permanent scatterers technique, performs an analysis on pixel base and focuses only on the points that have the most coherent phase behavior over a long time period. These points, the permanent scatterers, are minimally affected by temporal and geometrical decorrelation and, as a consequence, a large stack of available acquisitions can be used in the deformation estimation. Even images with baselines larger than the critical baseline, the maximum horizontal distance between the satellite orbits in order to perform conventional interferometry, can be

used in stacked processing when only this grid of sparse distributed stable point scatterers is used. Points that show phase stability over an image time series can only be assessed after estimation and removal of different phase contributors, as atmosphere, DEM errors and, orbit inaccuracies. As the amplitude values are almost insensitive to most of these contributors, an initial set of permanent scatterers, the permanent scatterer candidates, is selected based on amplitude statistics. The phase information of this network of permanent scatterer candidates is then used to estimate and remove unknown parameters as, e.g., atmosphere. Finally, a set of permanent scatterers is selected based on an evaluation of the phase coherence over time, and used to estimate deformation profiles per permanent scatterer (Ferretti et al., 2000, 2001).

One of the problems of the permanent scatterer technique is to make a first selection of points that have a stable backscattering behavior. This selection is an important step in the permanent scatterers procedure as subsequent processing is based on these points. A single SAR image consists of millions of pixels and a combination of tens of images, often from different sensors or processed by different processing systems, is needed to find stable point scatterers. The selection of permanent scatterer candidates in this study is based on an analysis of the amplitude time series of ERS-1 and ERS-2 images. To enable the use of all images in time series analysis, differences between the images, caused by, e.g., the use of different sensors as ERS-1 and ERS-2, or deviating satellite geometry, needs to be eliminated. Therefore, calibration of ERS SAR images has to be integrated as a processing step in the permanent scatterer selection procedure.

1.2 Objective

This study is an attempt to describe a well-defined and reliable procedure to identify consistently stable scatterers using a time series of amplitude data. It can be assumed that points with a high and stable amplitude over a long time series of SAR images also have a stable phase behavior, as the amplitude influences the phase variance and the phase variation is significantly less for higher amplitudes values than for lower amplitudes, assuming a same error ellipse. The use of amplitudes instead of phase observations has the advantage that amplitude values are less influenced by a number of contributions as atmosphere, topography and orbit errors. Thus, there is no need for removal or prior estimation of these unknown parameters before the first selection of permanent scatterer candidates is carried out. In order to make a selection of permanent scatterer candidates some preprocessing steps have to be performed, as, e.g., oversampling, calibration and coregistration of the SAR data. This study emphasizes on the calibration of ERS SAR imagery.

> *How should calibration of ERS SAR imagery be implemented in order to perform a selection of reliable permanent scatterer candidates?*

To answer this question several sub-questions are derived to give further direction to this study:

1. What are reliable permanent scatterers candidates and how are they used in deformation monitoring using the permanent scatterer technique?

To perform an accurate deformation profile estimation using the permanent scatterer technique, it is important to specify the demands on the initial data set of points that is needed as input for the permanent scatterer processing procedure. It is important that enough points scatterers are selected to enable permanent scatterers processing, i.e., the detection probability should be as high as possible. On the other hand, these points should have a coherent phase behavior: the percentage of selected permanent scatterer candidates, based on amplitude statistics, that are affected by decorrelation noise should be as low as possible. Insight in the selection procedure of permanent scatterer candidates and the relation to the subsequent permanent scatterer processing is needed to enable a critical evaluation of the selected sets of permanent scatterer candidates.

2. What preprocessing steps have to be performed before a selection of permanent scatterer candidates can be made?

To place the calibration procedure of ERS SAR imagery in a bigger picture, a good understanding of all processing steps that are needed to perform a selection of permanent scatterer candidates is necessary. A clear overview of all consecutive preprocessing steps should be given, before they can be implemented and tested.

3. Which calibration methods can be used to calibrate ERS SAR imagery?

There are many different methods to calibrate ERS SAR imagery, depending on the purpose of calibration. The main purpose of calibration in this study is to reduce the differences between ERS-1 and ERS-2 imagery to enable time series analysis of stacks of amplitude data. To develop a conceptual approach for such a calibration method, two different calibration methods will be implemented and tested in this study. First, a calibration method, developed by ESA, is studied and implemented. Next, an empirical method will be developed and tested. The different processing steps of both calibration methods and their limits and benefits will be described.

4. How does the calibration influence the selection of the permanent scatterer candidates?

After the ESA and empirical method are implemented a selection of permanent scatterer candidates can be made. In this study a test area of about 20 squared kilometers is chosen to limit the computation time. To perform a critical analysis of the influence of both calibration methods on the selection of permanent scatterer candidates, a comparison of the derived data sets of permanent scatterer candidates before and after the calibration methods will be performed. Besides, statistical properties of the amplitude data can be evaluated. Using these results, a proposal for the implementation of a calibration method for ERS SAR imagery for the selection of permanent scatterer candidates can be made.

These questions are answered by theoretical analysis and performing tests in a small area of 2 by 10 km. A crop from a data set of fifty SAR images of the area around Las Vegas city (Nevada, USA) is used to describe and implement the different processing steps that have to be performed to make a selection of permanent scatterer candidates. The Las Vegas data set consists of images from the European Remote Sensing Satellites (ERS) 1 and 2 and covers a time span of about ten years, with the first acquisition in April 1992 and the last in February 2002. The large amount of data and limited computing memory for processing force the use of smaller crops of the images for processing and testing purposes. To enable the use of all images from both ERS-1 and ERS-2 in amplitude time series analysis and diminish the differences, a calibration procedure needs to be set up. In this study the implementation of different image calibration methods based on amplitude observations and their influence on the final selection of permanent scatterer candidates will be described.

To analyze the amplitude behavior per pixel, the coregistration between the images over time needs to be determined very accurately. Every resolution cell should represent the same area with backscatterers in every image. In this study the available coarse and fine coregistration step within the in Delft developed software for radar processing DORIS (Delft Object-oriented Radar Interferometric Software) is used. DORIS uses a polynomial to coregister all images to one master image. In areas with much topography, as, e.g., steep mountains, it might be possible that the use of a polynomial not fully represents the topography and underestimates the coregistration parameters. As a refinement of the coregistration falls outside the scope of this study, test areas with little topography are chosen to minimize possible coregistration errors. In this study it is assumed that there are no coregistration errors that influence the evaluation of the implemented calibration methods and the selection of permanent scatterer candidates. The DORIS software and its tool 'cpxfiddle' are used to process and make crops from the available SAR data. New developed modules are implemented in Matlab.

1.3 Structure

This study focuses on the implementation and verification of amplitude calibration methods that enable the use of stacked processing of ERS-1 and ERS-2 radar data. Besides, a manual for the use of the calibration scripts written in Matlab to perform the ESA amplitude calibration is added to this thesis in Appendix C.

In the following chapter a brief overview is given of the principles of conventional InSAR techniques for deformation monitoring, as well as an overview of the more accurate permanent scatterers technique that enables deformation studies of Earth's surface on millimeter level. The available test data set of Las Vegas and the deformation pattern in this test area are described here as well. Chapter 3 discusses the implementation of two different amplitude calibration methods. First, a method developed by ESA and the correction factors used in this method are discussed in more detail. Next, an empirical approach to calibrate ERS SAR imagery is described. In Chapter 4 some test results of the ESA calibration method are described in order to give insight in the influence of the different correction factors on the data. The calibration method is tested by analyzing histograms and the statistical properties of the amplitude data before and after calibration. The results from the ESA calibration method are compared with the results obtained from the implemented empirical method and a first selection of permanent scatterer candidates is performed. Furthermore, an approach and some recommendations for the use of calibration in order to select permanent scatterer candidates are presented. Finally, in Chapter 5 conclusions are drawn from the presented test results and some recommendations for further research are given.

Chapter 2

Deformation Monitoring using SAR

2.1 Introduction

Each technique to monitor deformation of the Earth's surface has its advantages and disadvantages, depending on the measurement purpose. Levelling is a very accurate technique to determine changes in height, but it is time consuming and it provides only deformation information of a few network points on which measurements are made. InSAR, however, can give height change information on every pixel in a SAR image. Although InSAR has the advantage of a very high spatial resolution, it has a rather poor temporal resolution compared to continuous GPS. The latter technique provides long time series of almost continuous observations, but only on a restricted number of pre-defined points. The limits and potentials of InSAR compared to other geodetic techniques are discussed in more detail by Hanssen and Klees (1998).

In this chapter a brief overview is given of two different approaches to monitor deformation using SAR. First, in Section 2.2, conventional InSAR is discussed, followed by the permanent scatterer technique in Section 2.3. Also some limitations and advantages of both approaches will be outlined here. Finally, in Section 2.4 a description of the data set of Las Vegas test data set will be given, as well as a brief overview of the deformation in this area.

2.2 Principles of SAR Interferometry

Radar instruments like SAR actively emit microwaves pulses down to Earth and record these pulses after they are reflected back by the Earth's surface. From a height of about 800 kilometers the ERS SAR obtains 100 km wide strips of high-resolution imagery to the right of the satellite track. This is shown in Figure 2.1 where the image geometry of a SAR is given. On-ground signal processing is used to build up a complex image from the backscattered energy, which primarily depends on the roughness and properties of the illuminated area. As the ERS SAR has a polar orbit and radar has the advantage of being able to see through cloud and darkness, images can be acquired of the entire Earth whenever the satellite passes.

The single look complex (SLC) SAR images that are used in this research are arrays of complex numbers. The modulus of the complex values produce the radar intensity images, where variations of the brightness or *amplitude* of the signal reflect spatial variations of the physical characteristics of the ground surface. In each SAR image resolution cell, the *phase*, which is the argument of the complex value, is related to the distance between the radar antenna and the ground as a fraction of known radar wavelength (5.6 cm for ERS). Actually, the observed phase for a single resolution cell consists of two important

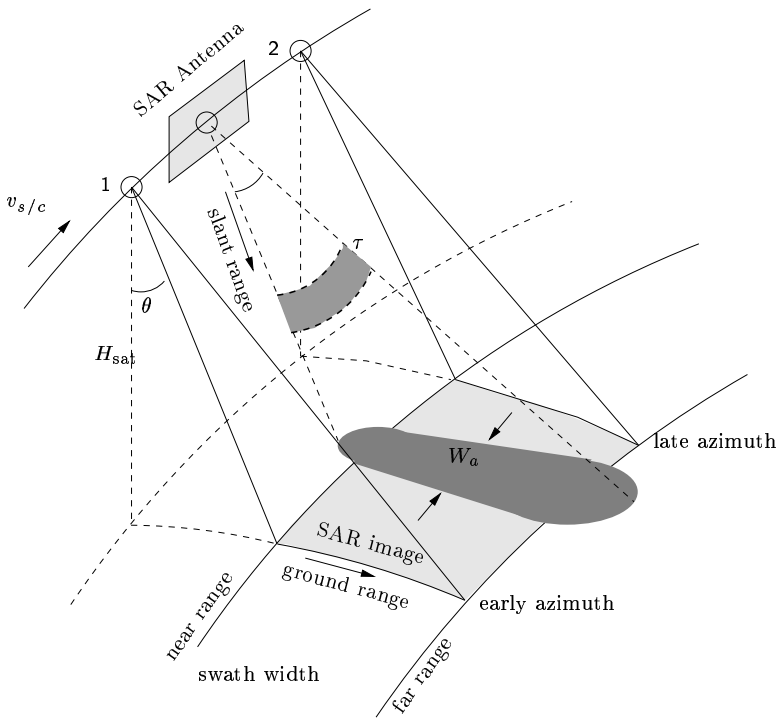

Figure 2.1: Imaging geometry of a SAR acquisition. Due to the spacecraft velocity $v_{s/c}$ the pulses, with pulse length τ, illuminate a swath parallel to the right of the satellite track under look angle θ. W_a is the radar footprint width in azimuth direction. The dark shaded area indicates the footprint of a single pulse. The total SAR image starts in azimuth at the "early azimuth" time, and lasts until the "late azimuth" time. In range direction, it covers an interval from "near range" to "far range", which corresponds to the light shaded area in ground range (after Hanssen (2001)).

contributions: the phase proportional to the distance and the phase due to the scattering characteristics of the resolution cell. If the phase measurements are repeated under exactly the same conditions, the contributions of the unpredictable scattering component are the same and cancel when obtaining the phase difference between two sensors. Interferograms are formed by the product of one complex SAR image and the complex conjugate of another image after sub-pixel coregistration. The phase of each pixel in an interferogram is the difference of the phases of the corresponding pixels in the two SAR images. Interferometric fringes within the interferogram depict variations of the path length differences between the two images. These fringes give information on possible deformation. This method is also called the repeat-pass method, as it uses radar images acquired by one antenna from different satellite passes.

As the satellite repeat orbits are in general not exactly the same, the two images are acquired from slightly different locations with a certain perpendicular baseline $B_\perp$ (see Figure 2.2). Interferometry can only be performed with images that have a nearly identical acquisition geometry, i.e., small baselines are required to ensure coherence between two observations. The maximum or so-called critical baseline $B_{\perp,\text{crit}}$ is for ERS approximately 1.1 km assuming a flat horizontal terrain. If the horizontal separation of the two satellites becomes too wide, there will be a loss of phase correlation or coherence between the radar signals. The interferometric phase is sensitive to the surface topography as points on Earth are observed from a slightly different geometry. If the two images are acquired at two different times, the interferometric fringe is sensitive to any displacement of the ground parallel to the radar line of sight during the acquisition time interval. The sensitivity of the interferogram to topography increases with the spatial separation of the two orbits, whereas the sensitivity to ground displacement is independent of the satellite configuration. Sensitivity to ground displacement is in general larger than the sensitivity to topography, allowing detection of ground displacement of a few millimeters.

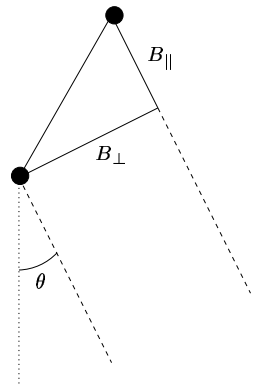

Figure 2.2: Perpendicular baseline $B_{\perp}$ and parallel baseline $B_{\|}$ between two satellites. The parameter $B_{\perp}$ is an important parameter to select images for interferogram creation (after: Hanssen (2001)).

The phase observation per resolution cell is actually a summation of the phases of all scattering elements within this area. The interferometric phase can be composed by a number of contributors (Hanssen, 2001),

$$\begin{aligned} \phi &= 2\pi k + \phi_{topo} + \phi_{defo} + \phi_{orb} + \phi_{atm} + \phi_{scat} + \phi_{noise} \\ &= 2\pi k + \frac{4\pi B_{\perp}}{\lambda R sin(\theta)} H + \frac{4\pi}{\lambda} D + \phi_{orb} + \phi_{atm} + \phi_{scat} + \phi_{noise}, \end{aligned} \tag{2.1}$$

with $2\pi k$ the phase ambiguity or unknown integer number of full phase cycles, λ the radar wavelength, R the slant range distance, θ the look angle, H the height and D the deformation in the radar line-of-sight for that observation. The so-called flat earth component and residual orbit errors are denoted by ϕ_{orb} and the atmospheric delay by ϕ_{atm}. The term ϕ_{scat} represents the signal due to changes in the scatter characteristics of the Earth's surface between two observation times and ϕ_{noise} includes remaining noise terms like thermal noise and coregistration errors.

To determine the deformation parameter, it is necessary to estimate and remove the other components that are given in Eq. (2.1) as good as possible. First, the topographic signal ϕ_{topo} needs to be separated from the deformation signal. To remove the topographic reference phase, two techniques can be used. When an external digital elevation model (DEM) is available, this model can be used to remove the phase term due to topography from the observed phase. This is the so-called "two-pass technique" as it requires besides the DEM only two passes of the satellite over the study area. In areas where DEMs are not available or poor of quality it is possible to combine three radar images of the same area. Two of these SAR images, which have a short temporal baseline, are used to estimate and remove the topographic phase signal. With one of these images and the third image another interferogram is formed. If a ground displacement event occurs during the time interval between the first and last interferogram this is reflected by the difference between these interferograms, as the topographic fringes common to both interferograms are eliminated. This method is called the "three-pass principle" because three images are required. When the orbit configuration is not favorable to the three-pass method, it is possible to use four images to produce the two interferograms that are subsequently differenced. A residual topographic phase can be left after the removal of the topographic reference phase, due to, e.g., inaccuracy of the used DEM. After the removal of the influence of topography, the unknown integer number of full phase cycles has to be resolved in the phase unwrapping procedure. Besides, the other unknown parameters have to be estimated and removed as good as possible, after which the remaining deformation signal can be obtained. More information on this topic can be found in Hanssen (2001).

In Chapter 1 some factors that limit the applicability of InSAR techniques are given. The variable state of the atmosphere, as well as geometrical and temporal decorrelation often prevents InSAR from being an operational tool for measuring deformation signals with millimeter accuracy per year. Therefore, other techniques are being explored that can provide that accuracy. One of them is the permanent scatterer technique that uses a multitude of radar acquisitions of the same area over a large time span.

2.3 Principles of Permanent Scatterer Technique

The starting point for the permanent scatterer technique is the differential InSAR technique, described in the previous section. Instead of using all pixels in only a few SAR images, this technique uses measurements from a limited set of inhomogeneously distributed points that show a stable phase behavior over long time intervals to provide high accuracy deformation information. Many of these points, known as Permanent Scatterers (PS), are man-made and therefore the use of this technique is very suitable in urban areas, where over 100 PS per km^2 can be identified. See Ferretti et al. (2001, 2000) and Hanssen (2003).

While conventional InSAR techniques are limited by atmospheric inhomogeneities, which affect the quality of the interferogram, and temporal and geometrical decorrelation that make a lot of available images useless for deformation monitoring, the PS technique can use all these images as this technique is less affected by them. On the selected points that are supposed to be stable sub-meter DEM accuracy and millimeter terrain motion detection can be achieved. Even if no fringes can be seen in interferograms, reliable elevation and deformation measurements can be obtained on this subset of image pixels. It is possible to estimate and remove atmospheric effects from the data using these stable network points. The dimension of the PS is often smaller than the resolution cell. Consequently, the coherence is good even for interferograms with baselines larger than the decorrelation one and all available images from the ERS dataset can be successfully exploited. If one wants to measure in areas that show large temporal decorrelation, as, e.g., in agricultural fields, the PS technique that is based on individual point scatterers can be a solution. Although not as much PS will be available as in urban areas, there might be enough for performing the PS processing.

The permanent scatterer processing can be split into different steps (Ferretti et al., 2000). First, the available $N+1$ images need to be calibrated and coregistered on a uniquely chosen master image. A DEM is estimated and used to remove topographic effects after which N different interferograms between all SAR images and the master are computed. Next, a subset of pixels, the permanent scatterer candidates (PSCs), is selected that shows a stable phase behavior over the image time series. A phase unwrapping procedure is performed on the sparse PSC grid, resulting in a set of unwrapped phase values relative to all interferograms. Atmospheric effects are estimated on the PSC grid and removed from the interferograms. Then, precise estimation of the heights and velocities of the PSCs with respect to a reference pixel of known elevation and motion is carried out. Evaluation of the phase coherence per pixel over the image time series results in the final group of pixels marked as permanent scatterers. PSC selection is important key step in the whole procedure. If the selected PSCs are too noisy or if too few PSCs are identified the estimation of atmospheric effects cannot be carried out successfully, compromising the accuracy of the deformation profile estimation per PS.

In the PSC selection procedure points are being selected that show stable phase behavior over long time intervals, i.e., ϕ_{scat} in Eq. (2.1) should be approximately zero. A method to select PSCs is coherence thresholding, as long time coherence implies stability of phase. PS identification is then carried out by means of a time series analysis of the phase values. Using this method a lot of noisy pixels are selected to be PSCs and a number of PSs can be neglected, as single coherent targets cannot be identified due to space averaging of the data when estimating coherence. However, there is no loss of resolution when performing the selection based on time series analysis of amplitude data. When using amplitudes instead of phase observations there is no need to remove or estimate the contributors given in Eq. (2.1) that influence the

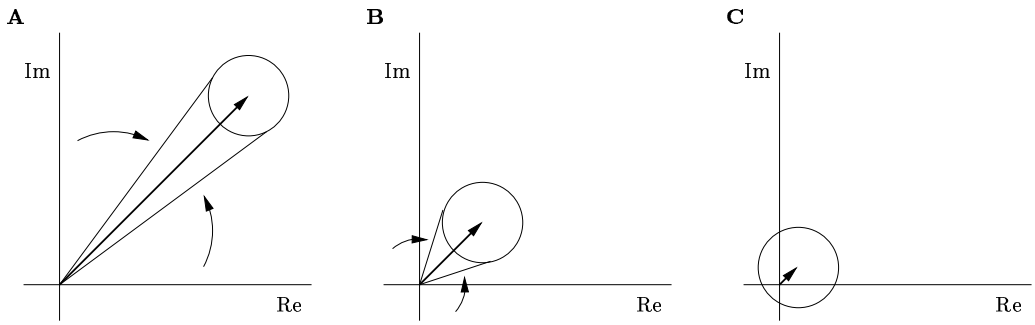

Figure 2.3: Example of varying phase variance with different values of amplitude. Given are an error ellipse in the complex plane with equal real and imaginary errors and an arrow, which represents the amplitude. When comparing A and B it becomes clear that the amplitude influences the phase variance and that the phase variation in A is significantly less than in B. In C the phase observation is nearly worthless (after Hanssen (2001)).

phase observations, as amplitudes are less influenced by these contributors. The first selection of PSCs from SAR images can be based on only amplitude statistics, as it can be assumed that points with a stable phase behavior over the image time series have also a stable phase behavior. This is explained in Figure 2.3. When a point has a high amplitude, a higher error in the phase observation is allowed for the same stability. Thus, if the amplitude shows a high stability this can also be expected for the phase.

A limitation of the PS technique is the fact that a lot of images are needed to select a reliable set of PSCs. According to Ferretti et al. (2001) at least 30 images are needed. Fortunately, the use of the whole image data set is possible in time series analysis, even the images with large temporal or spatial baselines. Another requirement to perform deformation analysis using permanent scatterers is the availability of a sufficient number of PSCs in the area of interest as the phase information of the selected PSCs are needed in further processing to estimate unknown parameters as, e.g., atmosphere and the deformation profile.

2.4 Test Area around Las Vegas

2.4.1 Deformation in Las Vegas

To test developed algorithms and select permanent scatterer candidates a data set containing ERS SAR data of Las Vegas city and its surroundings is used. Las Vegas, Nevada USA (36°12'N 115°13'W) is situated in a valley surrounded by desserts and mountains. The city itself lies about 620 meters above see level and is surrounded by the Spring mountains in the west, with highest top Charleston peak of 3632 meters high, and the Pahranagat Range in the north, with Sheep peak of 2972 meters the highest mountain. In Figure 2.4 a map of Las Vegas and its surroundings is shown, as well as an intensity image of one of the available SAR images. The city of Las Vegas is situated in the middle on the bottom of the intensity image.

About 45 km southeast of Las Vegas is Lake Mead. This lake, which lies just outside the area covered by the SAR images, was formed in the 1930s when the Hoover Dam was built, an enormous dam that controls the Colorado River to prevent floods in California. Lake Mead provides most of the water supply and electricity, not alone for Las Vegas, but also for the surrounding area and even a big part of the cities in California. Besides water from Lake Mead, groundwater is used to provide Las Vegas and all its gambling tourist of water. Since the late 1940s there was an accelerated groundwater pumping, which lowered the groundwater level over Las Vegas Valley up to 90 meters in some areas by 1990. This ground water level decline caused compression of the clay beds under the city, which led to subsidence rates of several centimeters per year during most of the 20th century. To stop the decline and subsidence

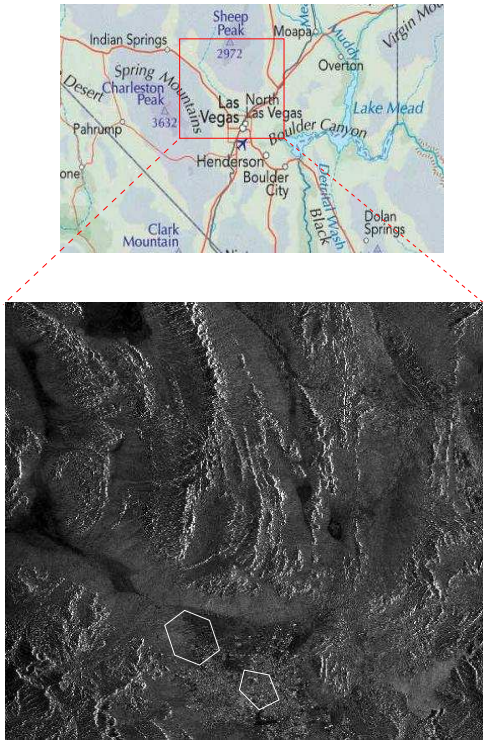

Figure 2.4: Top: Map of Las Vegas and its surrounding mountain ranges (web1). Under: intensity image of one of the fifty SAR images. The city, in the south part of the image can be distinguished very clearly, as well as some mountain ranges. The red square presents the approximate position of the SAR image, of 100 by 100 kilometers, on the map. The white polygons give an indication of the location of the main subsidence bowls in the city.

artificial recharge programs began in winter 1980, which resulted in more stable groundwater levels. Even some slight recovery of the groundwater level can be seen in some areas from the mid 1990s. Besides, the increased water import from Lake Mead reduced the groundwater pumping and the subsidence, especially during summers (Hoffmann, 2003).

The deformation pattern of the Las Vegas area in the nineties has been monitored using InSAR techniques in different studies, see, e.g., Amelung et al. (1999) and Hoffmann (2003). These studies show large subsidence bowls in the center and in the northwest of Las Vegas city (see white polygons in Figure 2.4). From 1992 to 1997 a multi-year displacement was measured of maximum 190 mm in the northwest and 110 mm in the central subsidence zone. This is low compared to levelling results in the early eighties, which show subsidence of about 50 mm per year. Between 1997 and 1999 subsidence rates have stabilized in some parts of the valley. However, there still remains a subsidence in the northwest of 25 mm per year. During winter the subsidence is almost entirely compensated by elastic expansion of the aquifer systems due to recovering of the groundwater level. In the winters of the late nineties an uplift of 30 mm was measured in the central subsidence zone, which compensates the subsidence of the summer. In both subsidence bowls a seasonal variation is measured, which has at least the same order of magnitude as the multi-year displacements and follows the annual cycle of pumping in summer and recharge in winter. By 1999, the seasonal fluctuations in the central zone far exceeded the multi-year trend.

The area around Las Vegas have favorable conditions to apply conventional interferometry. The desert environment and sparsely vegetated dry surfaces preserve the coherence of reflected signals over relatively large time periods. Nevertheless, in the urban area of Las Vegas city, e.g., construction activities can cause a loss of phase coherence locally. Then the use of the PS technique can be preferred.

2.4.2 Test Data Set

The data set used in this study consists of fifty SAR images, covering a time span of almost ten years from April 1992 to February 2002. There are sixteen images from ERS-1, launched by the European Space Agency (ESA) on 17 July 1991. ERS-1 was followed by ERS-2 in April 1995, providing a overlapping period in which images of both satellites were acquired until ERS-1 completed its operation in 1999. After May 1996 the Las Vegas data set contains only ERS-2 images. Both satellites have a repeat interval of 35 days, however, not for every satellite pass an image is available in the Las Vegas dataset. In Figure 2.5 a baseline plot is given of the available data. The time coverage is shown on the vertical axis and the perpendicular baseline $B_{\perp}$on the horizontal axis as a representation of the image geometry (see Figure 2.2).

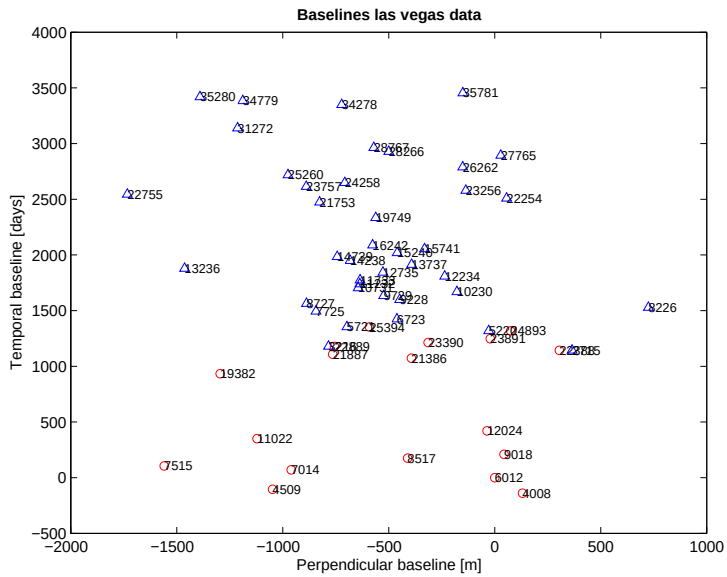

Figure 2.5: Baseline plot of fifty ERS SLC images of the Las Vegas data set with respect to ERS-1 image with orbit number 6012, 8 September 1992. On the vertical axis the temporal baseline between the images is given. The acquisition date of the images has a time span of about 10 years and varies between April 1992 and February 2002. On the horizontal axis the length of the perpendicular baseline is given. These parameters are used to select images for interferogram creation. The red circles represent ERS-1 images and the blue triangles are ERS-2 images.

Each image covers an area of about $100 \times 100km$, which corresponds to about 4900 pixels in across-track or range direction and 26500 pixels in along-track or azimuth direction, with a resolution of about 20 meters in range and 4 meters in azimuth direction. Each pixel contains a complex value from which amplitude and phase observations can be obtained.

Regarding the available data set, there are three of important issues that have to be taken in consideration before starting the processing and calibration of the SAR images. First, there are differences between ascending and descending tracks. ERS SAR images are always acquired to the right of the satellite track (see Figure 2.1). The ESA calibration procedure that will be described in the following chapter uses correction factors that vary in range direction and it is therefore important to know which area is represented by which pixel in the SLC image. It appears that the area closest to the satellite, near range, is always represented in the pixels in the first column of the image. So, if the intensity of the SAR images for descending tracks is plotted, the data seem to be 'flipped' geographically with near range on the left side of the image. As a consequence, the derived range dependent correction factors can be applied to the SLC data in the same way for ascending and descending images.

Product characteristics	PRI Product	SLC-Q	SLC-I
Pixel size (range-across track):	12.5 m	about 20 m	about 20 m
Pixel size (azimuth-along track):	12.5 m	about 4 m	about 4 m
Scene size (range):	8000 pixels	2500 samples	4900 samples
Scene size (azimuth):	at least 8200 lines	about 15000 lines	about 26000 lines
Pixel depth:	16 bits (uns. int)	16I, 16Q comp (signed int)	16I, 16Q complex (signed int)
Total product volume:	about 131 Mbytes	about 150 Mbytes	about 500 Mbytes
Projection:	ground range	slant range	slant range
Number of looks:	3	1	1

Table 2.1: Product characteristics for PRI, SLC-Q and SLC-I products (web2).

Secondly, there are differences in the way the raw SAR data is processed by the different Product Facility Centers (PAFs). Therefore, different parameters have to be applied in the ESA calibration procedure depending on where the data is processed (see Chapter 3). All images of the Las Vegas data set are processed by ESA's European Space Research Institute (ESRIN) in Italy. The ESA calibration method that is implemented during this research can also be used for calibrating SAR images from different PAFs, like the German D-PAF, Italian I-PAF and United Kingdom UK-PAF, when using the right tables of calibration parameters.

Finally, ESA provides different products: Precision Images (PRIs) and Single Look Complex (SLC) images. The PRI is a multi-looked ground range image. The product is applicable for most users interested in remote sensing applications. SLC images are SAR data processed into single-look images in the original slant range projection and have a complex data type. SLC images are particularly suitable for applications and techniques that require phase preservation as SAR interferometry. There are two forms of SLC products: the SLC-Q and SLC-I. The first is a product of quarter scenes or quadrants. They correspond to just over one half range by one half azimuth of the full image size, with some overlap of adjacent quadrants. SLC-I is a product covering a full frame. In Table 2.1 some characteristics of PRI, SLC-Q and SLC-I are given.

All images used in this research are SLC images. However, the ESA calibration procedure tested in this research is originally designed for PRIs. In appendix J of the ESA "ERS SAR Calibration" document (Laur et al., 2002) a brief description of a method to calibrate ERS SAR SLC images is given. However, a number of correction terms and their physical background stay unclear and there is a need for further interpretation. In the following chapter the ESA calibration method for SLC imagery will be described in more detail.

Chapter 3

Calibration of ERS SAR Imagery

3.1 Introduction

The permanent scatterers technique described in the previous chapter makes it is possible to detect and monitor displacements with millimeter accuracy per year. This technique can only be applied in areas that contain scatterers with a consistently high intensity in time as, e.g., in urban areas. To make a proper selection of permanent scatterers candidates several preprocessing steps on the radar data are necessary. In this study, the SAR images need to be *calibrated* in order to diminish differences between the SAR images, caused by, e.g., different satellite geometry or sensor characteristics (in this study ERS-1 and ERS-2), in stacked processing. Besides, existing *coregistration* procedures need to be refined in order to detect PSC on sub-pixel level. Although the latter falls outside the scope of this study, some remarks on the coregistration will be given in section 3.5.

In general, calibration of ERS SAR products is required for many different reasons, as, e.g., the determination of variation or drift in the radiometric performance of the SAR, the comparison of SAR products from ERS-1 and ERS-2 or different processing systems, or the use of SAR imagery for land applications. Dependent on the application the SAR images can be calibrated in an absolute or relative way (Meadows et al., 1998). *Absolute calibration* relates the digital pixel values in SAR data products to the physical estimation of the backscattering coefficient σ^0, which supports the geophysical interpretation of SAR data. *Relative calibration* enables the comparison and, important for this study, the use of both ERS-1 and ERS-2 imagery in homogeneous data stacks. Besides this subdivision, the calibration procedure of ERS SAR products is often divided in an external calibration and internal calibration step (Meadows, 1994). The *external calibration* concerns the analysis of the response of bright man-made point targets with a known backscattering coefficient. This results in estimated reference parameters, which can be used in the calibration procedure of other SAR images. The *internal calibration* involves the examination of the parameters generated on-board the ERS satellite that are needed in the calibration procedure.

Before the data can be calibrated the complex SAR data are oversampled and detected, i.e., amplitude values are derived from the complex SAR data. Successively, the oversampling, detection and calibration of the ERS SAR data are described in Section 3.2. Section 3.3 discusses the calibration of ERS SAR data according to a method developed by ESA (Laur et al., 2002). In this absolute calibration method the radar backscattering coefficient σ^0, a measure of the amount of energy reflected back to the radar, is calculated by applying several corrections to the data. The principal aim of the calibration in this study is the use of both ERS-1 and ERS-2 images in stacked processing and therefore the images will be calibrated absolutely first by calculating the backscattering coefficient and will be scaled to each other afterwards. Elements of both external and internal calibration can be found in the ESA ERS SAR calibration method. In Section 3.4 an empirical calibration method, based on the amplitude data, is presented.

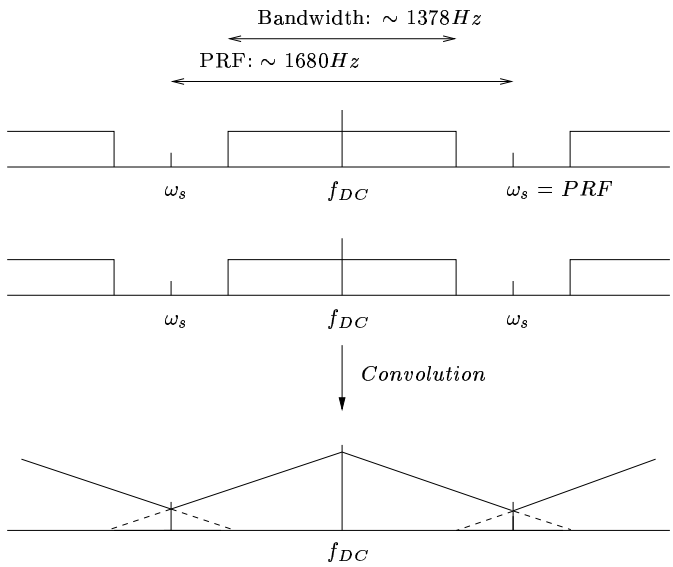

Figure 3.1: Example aliasing: The detection operator required for the calibration procedure provides amplitude values from complex SAR data by multiplying the complex pixel values with its complex conjugate (see Section 3.3.1). Aliasing effects are clearly visible in the spectral domain, as multiplication in the space domain yields convolution in the spectral domain. Here, a one-dimensional example is presented, with ω_s chosen equal to the PRF of about 1680 Hz (i.e., no oversampling is applied). In order to prevent aliasing a sampling rate of at least twice the PRF is required: $\omega_s \geq 2PRF$.

The oversampling and calibration procedure are both implemented using Matlab, while other processing steps are carried out using DORIS (Delft Object-oriented Radar Interferometric Software) and the additional utility cpxfiddle, which makes it possible to fiddle about with binary complex files and make crops of the data (Kampes, 1999).

3.2 Oversampling of SAR Data

3.2.1 Aliasing

Before the calibration can be performed the data need to be adequately sampled to preserve all statistical properties of the data and prevent aliasing. Aliasing can occur while creating interferograms when the data of the master image are multiplied by the complex conjugate of the slave image, but also at the detection of complex SAR data, as described in Section 3.3.1, when the data are multiplied by the complex conjugate of the data themselves.

To avoid aliasing the sampling rate should be chosen significantly larger than the Nyquist rate (see e.g. Haykin and van Veen (1999)), i.e., the sampling rate ω_s should be chosen at least twice the pulse repetition frequency (PRF), which is the rate at which consecutive chirps are generated by the SAR processor. The original ERS SAR complex data used in this research have a bandwidth of about 1378 Hz in azimuth direction and are sampled at a rate of almost 1680 Hz per resolution cell. In Figure 3.1 an example is presented with a sampling rate chosen below the Nyquist frequency. In this example, ω_s is chosen equal to the PRF, which causes overlap in the signal spectrum and aliasing occurs.

Besides the need of choosing a proper sampling rate, it is important to ensure that the complex power spectra is completely within the sampling window and is not folding over. As can be seen from Figure 3.3a the signal spectrum of SAR data is only centered at zero-Doppler frequency in range direction and not

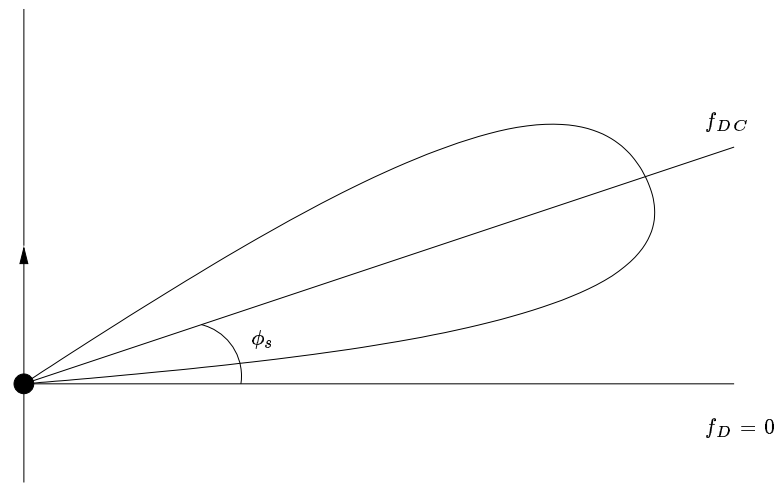

Figure 3.2: The Doppler centroid frequency and the zero-Doppler frequency: a two-dimensional view from the top with the antenna pattern and Doppler centroid direction. The deviation from the zero-Doppler frequency is mainly caused by a slight squint ϕ_s angle of the satellite.

in azimuth direction. The deviation in azimuth direction is mainly caused by a slight squint angle ϕ_s of the satellite which steers the antenna beam away from the direction perpendicular to the flight direction and causes a shift of the Doppler centroid frequency, as shown in Figure 3.2 (Hanssen, 2001). This shift has to be taken into account in the oversampling procedure.

3.2.2 Doppler Centroid Shift

As a single point scatterer is significantly smaller than the antenna beamwidth, the scatterer will be imaged within the antenna beam for a number of consecutive pulses in azimuth direction. During these pulses, the relative velocity of the point scatterer with respect to the radar changes, which causes an effect similar to the Doppler effect.

In Figure 3.2 two frequencies are given: the *zero-Doppler frequency* f_0, which denotes the direction in which the Doppler frequency is zero (perpendicular to the flight direction) and the *Doppler centroid frequency* f_{DC}, which denotes the frequency of the passage of a point scatterer through the antenna beam in the antenna boresight direction. If the antenna beam is aimed exactly perpendicular to the sum of the flight direction vector and the velocity due to Earth's rotation, f_0 and f_{DC} will be both zero. However, there will always be a squint angle that causes a deviation between these frequencies (Hanssen, 2001). An overview of the Doppler centroid frequency variations for the period spanning the Las Vegas dataset is given in Table 3.1. This table provides better insight into the size and general causes of the Doppler centroid frequency variations during different time periods of the ERS satellite missions.

The deviation of the Doppler centroid frequency f_{DC} with respect to the zero-Doppler frequency f_0 causes a shift in the azimuth spectrum (see Figure 3.3a). To avoid problems within the oversampling procedure due to this shift, the spectrum should be shifted back to f_0 before oversampling is performed. The oversampling procedure is divided into three steps, graphically presented in Figure 3.3. First, the signal is temporally shifted to the zero-Doppler frequency (Figure 3.3b). After that, the data are oversampled and finally shifted back to the original Doppler centroid frequency (Figure 3.3c and d).

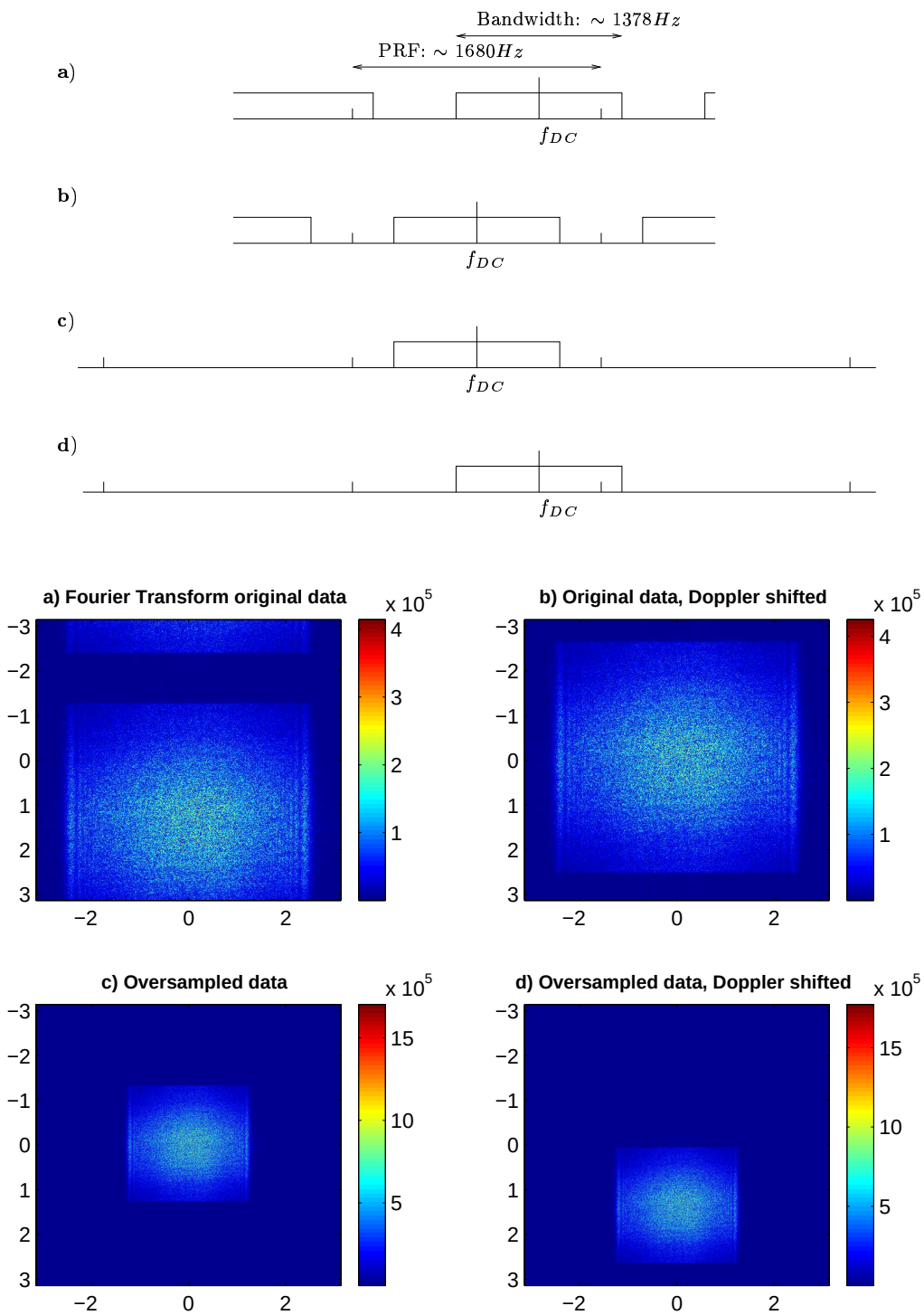

Figure 3.3: Overview of oversampling complex SAR data, taking into account the Doppler centroid frequency shift: one dimensional (above) and two dimensional example (under). a) Fourier transform of original data: the power spectra is 'folded over' from one end of the sampling window to the other. b) Spectrum shift of original data over the Doppler centroid frequency. c) Oversampling of the data by adding zero-rows and columns. d) Oversampled data shifted back to original.

Period	Variation of f_{DC}	Description
1992 - 1996	300 to 450 Hz	ERS-1 has been piloted with 3 gyroscopes since the beginning of the ERS mission, providing a stable attitude around the orbit.
1995 - 1999	75 to 250 Hz	ERS-2 has also been piloted with 3 gyroscopes since the beginning of the mission in 1995 (3 Gyro Mode).
Feb 2000 - Jan 2001	−300 to 300 Hz	Software to pilot ERS-2 with one single gyroscope has been developed and installed on board of ERS 2 due to several failures and problems on ERS 2 gyroscopes (1 Gyro Mode).
Jan 2001 - mid 2001	about 4000 Hz	In December 2000 the Extra Backup Mode (EBM) was uploaded and operationally since mid-January 2001. Doppler frequency variation during this period can be far over 4000 Hz. The available dataset of Las Vegas contains only one image with an f_{DC} of about 4000 Hz. InSAR applications are not recommended with EBM data.
mid 2001 - ...	1000 to 4000 Hz	In mid-2001 the Zero Gyro Mode was introduced, which results in over 90 percent of the f_{DC} remaining within ±4500 Hz.

Table 3.1: Changes of the Doppler centroid frequency variation for the available Las Vegas dataset in time. The variations in f_{DC} are taken from the fifty available images of Las Vegas. Generally, the values can show some deviation from the variations presented in this table for other data sets. For ERS-2 four time periods can be distinguished, dependent on the different 'modes' described in the last column (Meadows and Rosisch, 2003).

For the first step, the Doppler centroid frequencies of all images need to be computed. The Doppler centroid frequency of azimuth can be computed using a second degree polynomial as a function of pixel number p, the range sampling rate (RSR) of about 18.96 MHz and a constant, linear, and quadratic term, α_0, α_1 and α_2, read from the SLC leader file, part of the CEOS product header (Kampes (1999)):

$$f_{DC} = \alpha_0 + \alpha_1 \frac{p}{\text{RSR}} + \alpha_2 \left[\frac{p}{\text{RSR}}\right]^2 . \tag{3.1}$$

However, for oversampling it is sufficient to use only the constant term of Eq. (3.1), as long as the data are shifted back over the same frequency afterwards. The constant Doppler centroid frequency per image used to oversample the Las Vegas data are taken from the log-file that is produced when running the DORIS software. The parameters are read from this log-file into Matlab as most of the parameters are copied from the SLC leader file to the DORIS log-file during processing. Besides, it is easier, due to the format, to obtain parameters from this log-file than reading them directly from the leader file. The latter would require the use of other software as, e.g., the SAR toolbox of the ESA BEST-software (web3).

Once the Doppler centroid frequencies are known, the azimuth spectrum of a SLC image processed on a certain spectrum shifted f_{DC} is shifted to f_0. This shift can be presented in the frequency domain, but can also be obtained by pre-multiplication of the complex data z in the space domain:

$$z_s = z e^{-i2\pi \frac{f_{DC}}{PRF} l}, \tag{3.2}$$

with l the line number.

Secondly, the shifted complex data z_s is oversampled by a factor of two. This is performed in the frequency domain. After applying a two-dimensional fast Fourier transform algorithm, zeros are added to the spectrum in order to limit the signal bandwidth and prevent aliasing (see Figure 3.3c).

Finally, the spectrum is shifted back to the original Doppler centroid frequency. After applying an inverse fast Fourier transform, the oversampled shifted data $z_{s,os}$ are multiplied again with an exponential term, dependent on the PRF and the new line numbers l':

$$z_{os} = z_{s,os} e^{i\pi \frac{f_{DC}}{PRF} l'} . \tag{3.3}$$

The difference between Eq. (3.2) and (3.3) is a factor two in the exponential term, which is due to the oversampling factor. If this factor two would be applied to shift the oversampled data back, the Doppler shift would be twice as much. Note that this shift only affects the phases and not the amplitude observables. The described steps result in an oversampled image, taking into account the Doppler centroid frequency shift in azimuth direction. The intensity values needed for the calibration procedure can be detected from the oversampled data as will be described in the following section.

3.3 ESA Calibration Method

In order to study the backscattering behavior of point scatterers over time in different ERS SAR images, the SAR images need to be calibrated to diminish differences between the images caused by the use of different sensors. In this research fifty images from both ERS-1 and ERS-2 are available for the selection of permanent scatterer candidates based on amplitude statistics. In the calibration method, developed by ESA and presented in a technical report by Laur et al. (2002), the backscattering coefficient σ^0 is calculated, which gives an indication of how well radar energy is reflected. This backscattering coefficient is a result of applying corrections on detected complex radar data, dependent on differences in geometry, sensor type, processing and archiving facilities (PAFs), and product processing and acquisition date. In case of relative calibration the corrections are applied to correct for the use of different sensors (ERS-1 and ERS-2) and focusing with different processing systems. As all available images of Las Vegas are processed by ESA, the main reason for calibration in this research is to make it possible to analyze the amplitude data on pixel base from images acquired with different sensors.

The ESA report describes the derivation of the backscattering coefficient in ESA ERS SAR PRI products. However, the calibration of SLC complex data products requires a slight different approach compared to the approach for PRI products and is only shortly discussed in Appendix J of the ESA report (Laur et al., 2002). Therefore, a more extensive description of the calibration method for ERS SLC imagery and their physical background is given in Section 3.3.2. The main differences between the expressions of PRI and SLC products to calculate the backscattering coefficient from detected complex data are that no corrections for elevation antenna pattern gain and range spreading loss have been applied to the SLC products in the processing. Therefore, these corrections are included in the calibration procedure for SLC products. Another difference between the calibration procedure described in the ESA report and the calibration is that the ESA method calculates the backscattering coefficient for a distributed target consisting of more pixels, while this research is focused on the behavior of point scatterers in time. However, it is expected that this difference will have no large influence on the calibration results.

Before the backscattering coefficient σ^0 per pixel can be calculated, the complex data has to be detected. This is discussed in the Section 3.3.1. After that, the ESA calibration procedure for ERS SAR SLC products is described in more detail by giving an overview of all calibration corrections factors. In Appendix C a manual and scheme of the implemented Matlab-scripts to calibrate ERS SAR imagery according to the ESA method can be found.

3.3.1 Detection of Complex SAR Data

SAR images are composed of regular grids with complex values, which can be decomposed in an amplitude and a phase component. The real and imaginary components of the complex values are used to calculate the amplitude of the data, which is used in the calibration procedure. The calculation of the amplitude A for the calibration is called detection. The detection operation is performed by:

$$A = \sqrt{I^2 + Q^2}, \tag{3.4}$$

where I and Q are the real and imaginary complex samples. Note that in literature the amplitude is often denoted as the magnitude of the data. However, in this study the term amplitude is used. For calibration purposes the pixel intensity values, the square of the amplitude A^2, are used. Another expression for the detection operation is given by the multiplication of the complex data by its complex conjugate, which gives directly the intensity of the data needed for calibration.

3.3.2 Derivation of the Backscattering Coefficient

The backscatter coefficient for each resolution cell can be calculated after the complex data are oversampled by a factor two to avoid aliasing effects and after the data are detected. This coefficient gives information on the amount of transmitted energy that is reflected back to the radar. Besides this physical property of the backscattering coefficient, it can also be used for calibration purposes. In the ESA calibration method several corrections are applied to the data, which reduce the differences between images with different characteristics, as, e.g., sensor type, PAFs, and processing date, and make it possible to make a better comparison of the amplitudes of scatterers from different images over time. According to the SAR calibration method the backscatter coefficient can be determined as:

$$\sigma^0 = \frac{A^2_{c_{ij}}}{K}, \tag{3.5}$$

where K represents the calibration constant and $A^2_{c_{ij}}$ the calibrated intensity value per pixel. This calibrated intensity can be derived using the following expression:

$$A^2_{c_{ij}} = A^2_{ij} \frac{\sin(\alpha_i)}{\sin(\alpha_{\text{ref}})} \frac{R_i^3}{R_{\text{ref}}^3} \frac{1}{G(\theta_i)^2} \frac{\text{Image Replica Power}}{\text{Reference Replica Power}} \text{Power Loss}_{ij}, \tag{3.6}$$

with i and j are the slant range and azimuth pixel coordinates and α_i, θ_i and R_i are the incidence angle, look angle and slant range at pixel coordinate i. The parameters α_i, θ_i and R_i can be derived from geometrical considerations (see Figure 3.4). All factors of Eq. (3.6) are described in the following section.

The whole ESA SAR calibration procedure should be performed in linear scale, although in some tables the values of the calibration parameters are expressed in decibels and need to be transformed to linear scale. The final results are usually expressed in decibels:

$$\sigma^0_{dB} = 10 \log_{10} \sigma^0. \tag{3.7}$$

Spatial representativeness	Correction factor
Factors varying per range position	- local incidence angle correction - range spreading loss - elevation antenna pattern gain correction
Constant factor per image	- calibration constant K - replica pulse power correction
Factor varying per range and azimuth position	- powerloss (analogue to digital conversion)

Table 3.2: Overview of the ESA calibration correction factors and their spatial representativeness.

3.3.3 ESA Calibration Factors

The right hand-side of Eq. (3.6) consists of several correction factors, which are applied to the intensity values of an image. It shows the detected intensity value A_{ij}^2 per resolution cell, corrections dependent on the target incidence angle α_i and slant range R_i, corrections for the elevation antenna pattern gain (dependent on the look angle θ), the power of the replica pulse and a correction term to compensate for non-linearity of ERS-1 and ERS-2 on-board analogue to digital convertors. These correction factors can be divided into three groups based on their spatial representativeness (see Table 3.2). All calibration correction factors will be discussed in the remainder of this section.

Local incidence angle and range spreading loss correction

Two of the three corrections that only depend on the pixel range location in the image are the correction for varying local incidence angle and the correction for varying slant range. The local incidence correction at pixel coordinate i is given by:

$$\frac{\sin(\alpha_i)}{\sin(\alpha_{\text{ref}})}, \tag{3.8}$$

where α_i is the local incidence angle on pixel location i and α_{ref} the reference incidence angle of 23 degrees, the ERS SAR mid-range incidence angle. It is assumed that the incidence angle α_i on the imaging surface is represented on the ERS reference ellipsoid GEM6 (Goddard Earth Model 6, with oblateness coefficient 1/298.257), i.e., a flat terrain is considered. The exact derivation of the actual incidence angle per pixel requires the use of a Digital Elevation Model (DEM). Although the exclusion of any local surface slope can be of importance for mountainous regions like the Las Vegas area, no DEM information is included in this research. The incidence angle depends only on the ellipsoid and varies from about 19.5 degrees at near range to about 26.5 degrees at far range. Therefore, the factor in Eq. (3.8) varies between 0.85 and 1.14. As identical point targets in different images are most of the time situated at approximately the same range location (the range variation is max. 2 km between the images of the Las Vegas data stack), the correction factor for incidence angle will be approximately the same for these point targets in each image, and therefore not important for the calibration in this study.

The correction for range spreading loss compensation, which as said before has already been applied to PRI products in the processing but not for SLC products, is given by:

$$\frac{R_i^3}{R_{\text{ref}}^3}, \tag{3.9}$$

where R_i is the slant range to a pixel at ground range coordinate i and R_{ref} is the reference slant range of 847.0 km. The correction for range spreading loss is increasing from near range to far range, as the

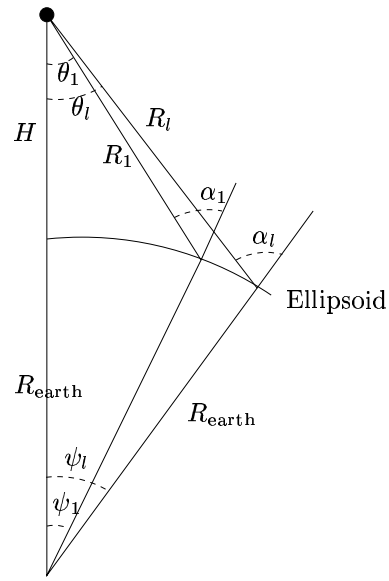

Figure 3.4: Geometric configuration of ERS SAR satellite, with H the ERS altitude, R_e the Earth radius, R_1 and R_l the slant range from the ERS to the first and last image pixel, θ the satellite look angle, ψ the angle between the vertical of the satellite and the vertical of image pixels and α the incidence angle.

loss of power of the radar signal is larger for scatterers at far range, i.e., scatterers that are further away from the sensor. This effect is also explained by the radar equation, which relates the range of a radar to the characteristics of the transmitter, antenna, target, and environment (see, e.g., Skolnik (1962)). The radar equation contains a factor for range variation in the denominator, which indicates at lower radar strength for scatterers that are close to the sensor. Therefore, the correction for range spreading loss is applied to compensate for variation in radar strength from near range to far range. The correction factor varies between 0.94 and 1.08. Again, this correction is not important for the calibration purpose in this study, as the range variation between the images is at most 2 km (about 100 pixels), and the correction factors for point targets in different images will have approximately the same values.

To obtain the correction factors for varying incidence angle and range spreading loss, the local incidence angle α_i and the slant range R_i need to be derived. These values can be calculated from geometrical considerations (see Figure 3.4) and three input parameters from the CEOS product header: the zero Doppler range time of the first range pixel t_1, the near range incidence angle α_1, and the processed scene center geodetic latitude ϕ. In this study, the parameters t_1 and ϕ can be read directly into Matlab by extracting them from the DORIS log-file to which these parameters are copied. Their original location in the CEOS product header can be found in the "data set summary record" of the SLC Leader File. However, the incidence angle at the first range pixel α_1 is not copied by DORIS to the log-file. Therefore, small changes are made in DORIS (in step1routines.cc) to get this value copied to the log-file from the "SLC facility related data record" of the CEOS product header.

From these parameters and some geometrical computations α_i, θ_i, and R_i at pixel coordinate i can be determined. Therefore, some other parameters need to be calculated first as the Earth radius R_{earth} and the ERS altitude H:

$$R_{\text{earth}} = a \, \frac{\sqrt{\cos^2\phi + (\frac{b}{a})^4 \sin^2\phi}}{\sqrt{\cos^2\phi + (\frac{b}{a})^2 \sin^2\phi}}, \tag{3.10}$$

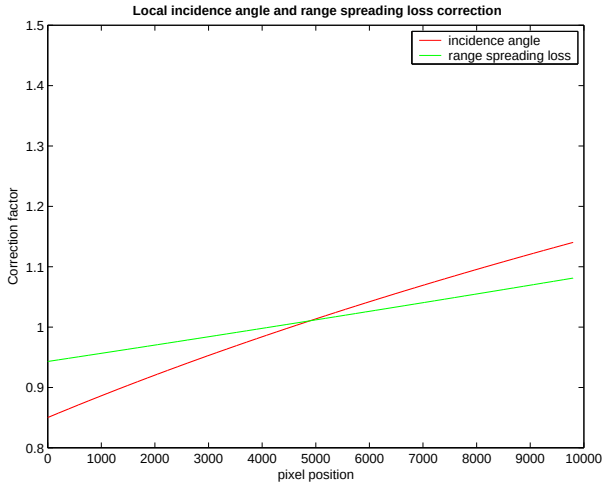

Figure 3.5: Example of the variation in range direction of the corrections for local incidence angle and range spreading loss. Typical variations from near range to far range are for the local incidence angle correction from 0.85 to 1.14 and range spreading loss from 0.94 to 1.08.

with a the equatorial Earth radius of 6378.144 km and b the polar Earth radius of 6356.759 km corresponding to the ERS reference ellipsoid GEM6. Next, the ERS altitude H can be derived from the geometry presented in Figure 3.4.

$$\begin{aligned}(R_{\text{earth}} + H)^2 &= R_{\text{earth}}^2 + R_1^2 + 2R_{\text{earth}}R_1 \cos\alpha_1 \\ H &= \sqrt{R_{\text{earth}}^2 + R_1^2 + 2R_{\text{earth}}R_1 \cos\alpha_1} - R_{\text{earth}},\end{aligned} \tag{3.11}$$

with the slant range to the first pixel computed by $R_1 = c\frac{t_1}{2}$ and c the speed of light. Assume that the Earth radius R_{earth}, calculated in the center of the image, is constant in subsequent computations.

Finally, the parameters that are needed in the calibration procedure can be calculated. The slant range from the ERS satellite to a pixel at range coordinate i, with $\Delta r = \frac{c}{2f_s}$ the pixel spacing in range direction, is derived by:

$$R_i = R_1 + (i-1)\frac{c}{2f_s}. \tag{3.12}$$

The look angle at pixel coordinate i, needed for the elevation antenna pattern gain correction, is given by:

$$\theta_i = \frac{\arccos(R_{\text{earth}}^2 - (H + R_{\text{earth}})^2 - R_i^2)}{-2R_i(H + R_{\text{earth}})}, \tag{3.13}$$

and the incidence angle at pixel coordinate i can be obtained from:

$$\alpha_i = \pi - \arccos\frac{(H + R_{\text{earth}})^2 - (R_{\text{earth}})^2 - R_i^2}{-2R_i(R_{\text{earth}})}. \tag{3.14}$$

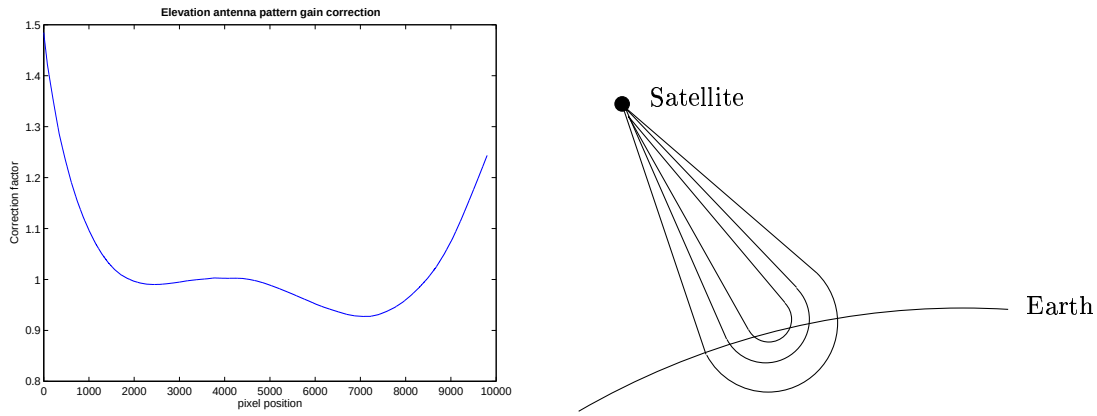

Figure 3.6: Example of the variation in range direction of the elevation antenna pattern gain correction (left). The correction factor varies with the look angle from 1.5 at the edges of the image to 0.93 at the sub-center of the image. The correction follows the strength contour lines of the transmitted radar signal along the antenna beam pattern in range direction (right).

The correction factors for both local incidence angle and range spreading loss variations in range direction are presented in Figure 3.5. Note that in the center of each azimuth line the corrections will be almost one, i.e., almost no corrections are applied to the intensity values according Eq. (3.6). The correction factors at near range and far range are larger. The main consequence of the local incidence angle and range spreading loss corrections are that the intensity values are more balanced over the image.

Elevation antenna pattern gain correction

The correction for elevation antenna pattern gain depends also on the pixel range location in the image: it depends on the varying look angle θ. The need for applying this correction is caused by different strength of the transmitted radar signal along the antenna beam pattern in range direction, like strength contour lines (see Figure 3.6). The antenna pattern gain correction is derived from look up tables that include gain values (dB) varying with the relative look angle $\Delta\theta$:

$$\Delta\theta = \theta_i - \theta_{\text{ref}}, \tag{3.15}$$

with θ_i from Eq. (3.13) and θ_{ref} the boresight angle of 20.355 degrees.

The values given in the look up tables in the ESA document are estimated using external calibration. The values are derived by using the mean range profile of several images of uniform areas, as images from the Amazon rainforest (Meadows and Rosich, 2003). There are different look up tables available depending on the different dates of processing and the processors used at ESA or other Processing and Archiving Facilities (PAFs). Some improvements were made to the implementation of the elevation pattern in the ESA Verification Mode Processor (VMP v6.8) at extreme near and far ranges in November 2001. In this study only one table is used, as all Las Vegas data are processed by ESA after November 2001.

The correction for elevation antenna pattern gain is applied by the factor:

$$\frac{1}{G(\theta_i)^2}. \tag{3.16}$$

In Figure 3.6 the elevation antenna pattern correction for the Las Vegas data set is shown on a linear scale. The correction factor varies from 1.5 at near and far range to almost one at the center of the image

azimuth line. This pattern is due to the nature of the transmitted signal by the sensor, as the strength of the signal is not the same for every resolution cell in range direction.

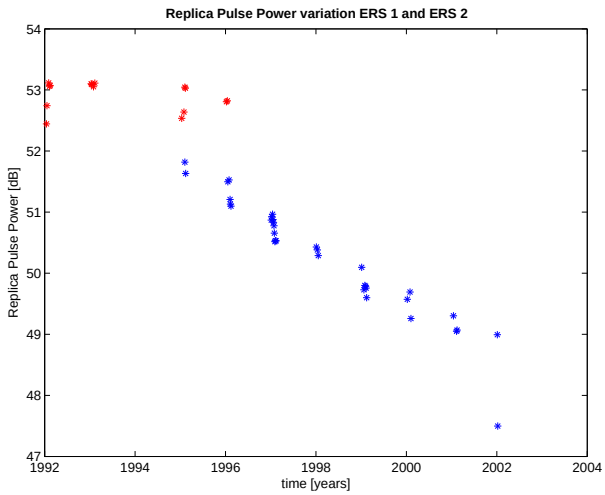

Figure 3.7: Values for the replica pulse power for ERS-1 (red) and ERS-2 (blue) images in dB for the Las Vegas data set. These variations correspond to values known from literature. The ERS-2 values show a continuous decrease corresponding with the variation of the calibration power and transmitted pulses. For ERS-1 the variation of the replica pulse power is about 1.0 dB, while it is known that the calibration pulse power variation for ERS-1 is much smaller. Therefore, corrections for the replica pulse power are needed for ERS-1 imagery.

Replica pulse power correction

The replica pulse power correction is applied to avoid the incorrect use of parameters in SAR processing. There are two types of calibration parameters measured in the SAR. First, at the start and end of each imaging sequence four calibration pulse measurements are made. Second, during the imaging sequence, copies of the transmitted pulses, the replica pulses, are generated and appended to the raw data. These latter quantities are used to monitor the system gain drift due to temperature changes and ageing. They are especially important for ERS-1 imagery as ERS-1 does not have an automatic gain control system. The calibration pulses, that measure the majority of the gain drift from image sequence to image sequence are more representative than the replica pulses that monitor the gain drift during the imaging sequence (Meadows, 1994). However, the replica pulses are being used in the processing, as the more representative calibration pulse is not available most of the time.

Both ERS-1 and ERS-2 data are processed by the PAFs in more or less the same way. Replica pulses are used in SAR processing as a representative of the transmitted pulses during the image acquisition period. Processed ERS-1 and ERS-2 images are scaled by the use of the local replica pulse. Any change in transmitted pulse power must be reflected in a similar change in the replica pulse power, in such way that imagery can be radiometrically corrected. While using the replica pulse within a SAR processor, it is assumed that the replica pulse is directly proportional to the transmitted pulse power. In that case, any transmitted pulse power variations would be compensated in the resultant SAR image. Unfortunately, the replica pulse has different power characteristics for ERS-1 and ERS-2. The energy of the ERS-1 replica pulse is poorly correlated with the actual transmitted power and will be different to the energy of the replica pulse used to determine the overall calibration constant K. This calibration constant, determined using a scene of Flevoland in 1991 and transponders in this area, is different for ERS-1 and ERS-2 and is needed to estimate the backscattering coefficient in Eq. (3.5). As a consequence, the replica pulse variations introduced by a SAR processor for ERS-1 need to be removed from the data to use the calibration constant K correctly. This is done by comparison of the replica pulse power used to generate the image in question with the replica pulse power used to generate the reference image in Flevoland in

1991 from which the calibration constant K was derived.

The SAR processors at the PAFs use one replica pulse power per image. Therefore, the power of the replica pulse is removed from ERS-1 data by applying the following correction factor per image:

$$\frac{\text{Image Replica Power}}{\text{Reference Replica Power}}, \tag{3.17}$$

with a reference replica power of about 53.12 dB obtained from the ERS-1 reference image of Flevoland in 1991. The replica power per image can be found in the "facility related data record" of the CEOS product header file and is extracted from the DORIS log-file after adapting the "step1routines.cc" file of DORIS. As said, the replica pulse power correction is only required for ERS-1 imagery. The ERS-2 data changes in transmitter pulse power are reflected in the replica pulse, i.e., replica and calibration pulse powers are correlated. Hence, no replica pulse correction is required when obtaining the backscattering coefficient from ERS-2 imagery.

In Figure 3.7 the variation of the replica pulses in time are shown for the Las Vegas data. The red stars represent the replica pulses from ERS-1 imagery and the blue stars represent the ERS-2 imagery. From literature it is known that the replica power shows a drop in power as a function of time: the rate of decrease for ERS-2 is approximately 0.66 dB per year between its launch and the end of 2000, and approximately 0.82 dB to September 2002 (Meadows and Rosisch, 2003). Changes in the ERS-1 SAR replica pulse power can be as large as 2 dB, while the transmitter pulse is for the most part stable. The exact variation can strongly differ per time period (Meadows et al., 2001). As can be seen in Figure 3.7 these variations do also apply for the Las Vegas dataset.

Powerloss correction

The powerloss correction involves a correction for non-linearities in the analogue to digital convertor (ADC) on board ERS satellites. Within this ADC the in-phase (I) and quadrature (Q) Gaussian distributed channels of the raw SAR data are quantized to 5 bits each. This way, the data can take integer values in the range -16 to 15. Each channel has a Gaussian distribution, having a maximum at a value of 0 or -1 and should fall to zero at -16 and 15 (Meadows, 1994). If the tail of the distribution does not fall to zero at these upper and lower quantisation levels this can have two different reasons: 'bit redundancy' or saturation. The first situation occurs when, e.g., areas with a low radar reflection having a low backscattering coefficient are present in the image. If the input for the ADC is low only some of the available quantisation levels are used. If, on the other hand, regions with high backscatter values can be found in the image, the input signal to the ADC can get too high, causing saturation: a large number of data values will occupy the lowest and highest quantisation levels, resulting in a situation in which the output from the ADC will be less than the input power, i.e., there is a loss of power.

Powerloss due to ADC saturation mainly occurs over large areas with a high backscatter level. In literature, the influence of the ADC saturation is often applied in areas with uniform high backscattering, as in areas with the same surface type like only sea or ice (see, e.g., Meadows et al. (1998)). The influence of ADC saturation in areas that not have a total uniform high backscattering levels are not mentioned, like urban areas with a high density of point scatterers as in the Las Vegas data set. Although the powerloss correction is not mentioned in literature for areas containing many point scatterers, this correction will be applied to the Las Vegas data set.

Figure 3.8 shows that areas containing point scatterers with a high backscatter level show correction factors for ERS-1 up to 1.2 for mountainous or urban areas, which is large compared to the previous discussed correction factors. The powerloss correction for ERS-2 imagery is significantly less due to the reduced gain settings of several dB below that of ERS-1. As a result, the ADC saturation problem for ERS-2 almost disappears.

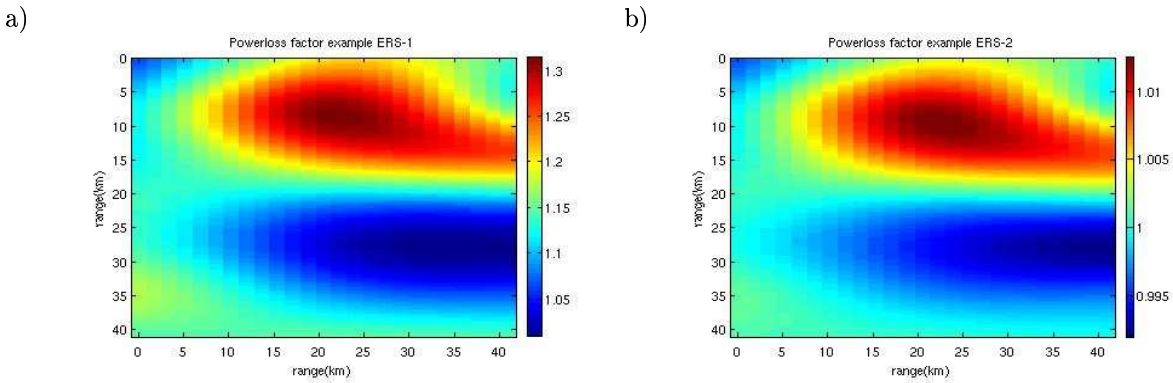

Figure 3.8: Overview of powerloss correction factors for an ERS-1 image (a) and ERS-2 image (b) after interpolation of an area of 40×40 km of Las Vegas. The correction factors can be up to 1.2 for mountainous and urban area for ERS-1. The corrections for ERS-2 are less due to the reduced gain settings. Both images show the same pattern of correction factors.

The procedure to calculate the powerloss for ERS imagery is very briefly described in the ESA technical report by Laur et al. (2002). However, the procedure has been explained in more detail by Ralph Cordey during a visit to ESA-ESTEC in Noordwijk. After his explanation and reading the ESA report extensively the powerloss correction is implemented in Matlab. The procedure to calculate the powerloss correction factors consists of several steps. First, after oversampling the full images with factor two and applying the detection operator, the uncalibrated data should be root mean squared block averaged in blocks of $b \times b$ pixels:

$$A_{uv}^2 = \frac{1}{b^2} \sum_{i=1}^{b} \sum_{j=1}^{b} A_{ij}^2, \tag{3.18}$$

with u and v averaged slang range and pixel coordinates and $b = 100$, recommended in the ESA report. This corresponds to about 400 meter in azimuth and 790 meter in slant range direction.

Subsequently, the powerloss amplitudes $A_{pl_{uv}}^2$ are calculated by correcting the block-averaged data by the replica pulse power correction. In contrast to described before, this correction is now applied to both ERS-1 and ERS-2 data. This has different physical reasons. For ERS-1 imagery one have to get back to the raw data values on a scale equivalent to those for which the powerloss correction curves in the look up tables provided by ESA have been drawn up (see Figure 3.9). This scale corresponds to the values obtained from the transponder reference scene. Hence, one have to correct for the same reasons as described earlier. The powerloss correction for ERS-2 is, due to the reduced gain settings, very small. Nevertheless, if one wants to correct for the ADC saturation and use the ADC saturation curves provided by ESA, the fact that the transmitter power on ERS-2 is declining over time has to be taken into account. The used scale has to be shifted by comparing the used local replica pulse power in the processing to normalize the image with the replica pulse power at the time of the reference scene for which the saturation curves were derived. The powerloss amplitude is then derived by:

$$A_{pl_{uv}}^2 = A_{uv}^2 \frac{\text{Replica Pulse Power}}{\text{Reference Replica Power}}, \tag{3.19}$$

with a reference replica power of 205229 for ERS-1 and 156000 for ERS-2 (linear scale).

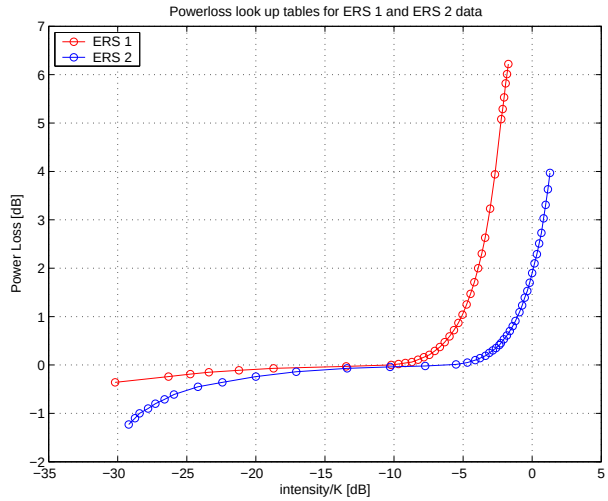

Figure 3.9: Powerloss curves from the look up tables provided by ESA (Laur et al., 2002). The red curve shows the powerloss values for ERS-1 imagery and the blue curve the values for ERS-2 imagery. The powerloss for ERS-1 is larger than for ERS-2 due to reduced gain settings of ERS-2 after July 1995.

The next step is smoothing the powerloss amplitudes with a window of size 5.5 km by 4.8 km (azimuth and range resolution). This corresponds to about 1400 x 600 pixels.

$$A^2_{pls_{uv}} = \frac{b^2}{600 * 1400} \sum_{k=u-300/b+1}^{u+300/b} \sum_{l=v-700/b+1}^{v+700/b} A^2_{pl_{uv}}, \tag{3.20}$$

with $u = 300/b$ to $(n - 300)/b$ and $v = 700/b$ to $(m - 700)/b$, with an original image size of m by n pixels. Although the use of a moving window over the image may lead to better results, in this study the powerloss amplitudes are interpolated to reduce calculation time. Finally, this results in one amplitude value per pixel.

The resultant smoothed powerloss amplitudes $A^2_{pls_{uv}}$ are converted using the calibration constant K of the image in question:

$$\frac{A^2_{pls_{uv}}}{K}. \tag{3.21}$$

After conversion to decibel scale the resulting powerloss values per area can be determined using the look up tables provided by ESA. Figure 3.9 shows the powerloss curves obtained from the look up tables.

After all correction factors are known, the backscattering coefficient for every pixel can be calculated by Eq. (3.5), which is a measure for the energy reflected back by the Earth's surface. This results in values between zero and about 1.2 in linear scale. As we are in this study not interested in the backscattering coefficient, but in the behavior of the intensity values of the data over time, the backscattering coefficients are scaled back again to intensity values using ERS-2 as reference, i.e., all images are scaled to ERS-2:

$$A_{\mathrm{cal}_{ij}} = \frac{A^2_{c_{ij}}}{K} K_{\mathrm{ref}} \tag{3.22}$$

For K_{ref} the value for the ERS-2 calibration constant K for ESA products processed after 20 January 1997 is chosen, with $K_{ref} = 93325.3$. The choice of K_{ref} is just an arbitrary choice to equalize the amplitude values from different sensors to enable stacked processing.

In Figure 3.10 all corrections, except the power loss, are given for an ERS-2 image. The significance of the implemented ESA calibration method will be discussed in Chapter 4, where the influence of all correction factors on the data will be described, as well as the influence of the calibration correction factors for the selection of permanent scatterer candidates. Moreover, the ESA method will be compared with an empirical calibration method. This empirical method is described in the following section.

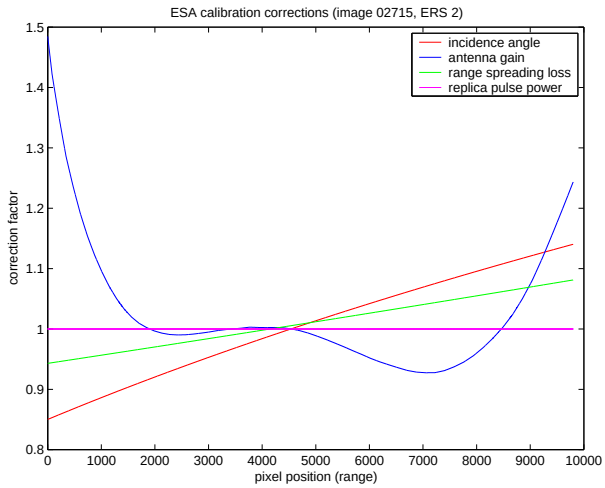

Figure 3.10: Variation in range direction of the incidence angle, range spreading loss, elevation antenna pattern gain and replica pulse power correction. The correction factors are for an ERS-2 image of Las Vegas (orbit number 02715, on 27 October 1995). As it is an ERS-2 image, the replica pulse power correction is one, i.e., no correction is applied.

3.4 Empirical Calibration Method

A relative simple calibration method is developed to enable a comparison with results obtained from the ESA calibration method. The implemented empirical method has the advantage that SAR images from other satellites than ERS, as, e.g., Envisat, can be included in the calibration procedure and used in the stacked processing of the permanent scatterer technique, whereas the ESA calibration method is restricted to the calibration of ERS imagery.

The empirical calibration method is based on a selection of the amplitude data. In short, per image a constant factor c_k is estimated from a restricted set of amplitude data, which contains only stable scatterers. This factor is used to calibrate all amplitude values within this image by multiplication with this constant factor. The estimation of factor c_k is restricted to a limited set of points, as for this estimation a data set of stable amplitude values with a Gaussian distribution is required. The distribution of amplitude values A is given by the Rice distribution (Papoulis, 1968). The shape of this distribution depends on the signal-to-noise ratio (SNR). For low SNR, the Rayleigh distribution can be used as model for the amplitude radar data. For high SNR, in general SNR > 4, the Rice probability density function approaches a Gaussian distribution (Ferretti et al., 2001). In Section 4.4 this is tested for the data with high SNR by applying a Kolmogorov-Smirnov test.

An almost similar calibration method is performed by Lyons and Sandwell (2003) that calculates the average calibration factor per image using the ratio of the amplitude of each image (mean of the amplitude values of all pixels) to the mean amplitude of the entire set. Each SAR image is divided by this calibration factor to equalize the brightness between the images. Next, the inverse of the amplitude dispersion is used to select stable point scatterers. The difference with the empirical calibration method implemented in this study is that the method used by Lyons and Sandwell (2003) uses the amplitude values of all pixels, whereas the method in this study is based on a selection of stable scatterers.

The empirical calibration method starts with creating time series of oversampled amplitudes per resolution cell of coregistred images. An initial selection ofpoints that have stable amplitude values is performed on these time series by using the dispersion index D_A (Ferretti et al., 2001):

$$D_A = \frac{\sigma_A}{\mu_A}, \tag{3.23}$$

where μ_A and σ_A are the mean and the standard deviation of the amplitudes over the image time series per pixel $p = 1, 2, \ldots, P$. Pixels with $D_A < 0.25$, i.e., pixels that have a high amplitude and low standard deviation, are pointed out to be stable scatterers. The threshold value is set on 0.25, as for this value the most points are selected of which the amplitude values have a Gaussian distribution. If the threshold value is set lower, less points are selected. If the threshold value is chosen higher, the amplitudes are no longer Gaussian distributed (see Section 4.4.5). The selection based on the dispersion index corresponds with the inverse of the previously mentioned condition SNR > 4. The mean μ_{A_p} and standard deviation σ_{A_p} per pixel p are derived using:

$$\underline{\mu}_{A_p} = \frac{1}{K} \sum_{k=1}^{K} \underline{A}_p^k, \tag{3.24}$$

$$\sigma_{A_p} = \left(\frac{1}{K-1} \sum_{k=1}^{K} (\underline{A}_p^k - \underline{\mu}_{A_p})^2 \right)^{\frac{1}{2}}, \tag{3.25}$$

with $k = 1, 2, \ldots, K$ and K the number of available images.

This results in a number selected PSC with their amplitude values $A_1^k, A_2^k, \ldots, A_{PS}^k$ per image k and with $ps = 1, 2, \ldots, PS$ the selected PSCs. From these amplitude values and the mean amplitude per PSC over time $\mu_{A_1}, \mu_{A_2}, \ldots, \mu_{A_{PS}}$ the calibration factor c_k can be calculated per image. To enable a fast computation of the constant calibration factors c_k for testing purposes, a simplified model is used in this study. The mean values $\mu_{A_{ps}}$ are assumed to be deterministic, whereas they are in fact stochastic. Besides, it is assumed that the amplitude observations are uncorrelated and the same for every observation, wtih $\sigma_{A_{ps}^k} = 1$.

$$c_k = \frac{1}{PS} \sum_{ps=1}^{PS} \frac{\underline{A}_{ps}^k}{\mu_{A_{ps}}}, \qquad \text{with} \quad ps = 1, 2....PS. \tag{3.26}$$

For all images, this results in the following model with $m = k \cdot ps$ observations, the amplitudes of the PSCs per image, and $n = k$ unknowns, the constant calibration factors per image.

$$E\{\begin{pmatrix} \underline{A}_1^1 \\ \underline{A}_2^1 \\ \vdots \\ \underline{A}_{PS}^1 \\ \cdots \\ \underline{A}_1^2 \\ \underline{A}_2^2 \\ \vdots \\ \underline{A}_{PS}^2 \\ \cdots \\ \vdots \\ \cdots \\ \underline{A}_1^K \\ \underline{A}_2^K \\ \vdots \\ \underline{A}_{PS}^K \end{pmatrix}\} = \begin{pmatrix} \mu_{A_1} & 0 & \ldots & 0 \\ \mu_{A_2} & 0 & \ldots & 0 \\ \vdots & \vdots & \ddots & \vdots \\ \mu_{A_K} & 0 & \ldots & 0 \\ \cdots & \cdots & \cdots & \cdots \\ 0 & \mu_{A_1} & \ldots & 0 \\ 0 & \mu_{A_2} & \ldots & 0 \\ \vdots & \vdots & \ddots & \vdots \\ 0 & \mu_{A_K} & \ldots & 0 \\ \cdots & \cdots & \cdots & \cdots \\ \vdots & \vdots & \ddots & \vdots \\ \cdots & \cdots & \cdots & \cdots \\ 0 & 0 & \ldots & \mu_{A_1} \\ 0 & 0 & \ldots & \mu_{A_2} \\ \vdots & \vdots & \ddots & \vdots \\ 0 & 0 & \ldots & \mu_{A_{PS}} \end{pmatrix} \begin{pmatrix} c_1 \\ c_2 \\ \vdots \\ c_K \end{pmatrix}, \qquad \text{with} \quad Q_y = \sigma_{A_{ps}^k} I_m \tag{3.27}$$

Finally, the calibrated amplitudes $A_{\text{emp}_p}^k$ are calculated by multiplying each amplitude value A_p^k within image k with the calibration factor c_k, which is constant per image:

$$A_{\text{emp}_p}^k = c_k \underline{A}_p^k. \tag{3.28}$$

The calibrated amplitude values from the ESA calibration method are compared with the calibrated amplitude values from this empirical method in Chapter 4 using crops of images from the Las Vegas data set.

To enable a critical analysis on the quality of the empirical calibration method, the model given in Eq. (3.27) should be improved in further research. A suggestion for the implementation of an improved model is presented in Appendix B. This method estimates the c_k factors using all amplitude observations. The images are scaled to an unknown reference image. This reference image and the c_k factors are estimated iteratively using a linearized model (see Appendix A and B).

3.5 Coregistration of SAR Imagery

Although full implementation and refinement of the coregistration procedure falls outside the scope of this study, some attention is given on the way the method is implemented in this study using the in Delft developed software for radar processing DORIS (Delft Object-oriented Radar Interferometric Software). Coregistration parameters between the images need to be determined very accurately to enable time series analysis of the amplitudes on pixel base. In the coregistration procedure the images are placed on top of each other in such a way that every resolution cell represent the same area with backscatterers in every image. The coregistration is performed on different times for the ESA calibration method and the empirical calibration method. If the ESA calibration method is used, coregistration has to be performed after the calibration, whereas for the empirical method coregistration is required before the images are calibrated, as the empirical method is based on a initial selection of PSCs from the oversampled raw data using time series analysis on pixel base (see for an overview of all processing steps Figure 5.1).

In this study the available coarse and fine coregistration step within DORIS is used. DORIS uses a polynomial to coregister all images to one master image. In areas with much topography, as, e.g., steep mountains, it might be possible that the use of a polynomial not fully represents the topography and underestimates the coregistration parameters. As a refinement of the coregistration falls outside the scope of this study, test areas with little topography are chosen to minimize possible coregistration errors. In this study the coregistration is performed using a second order polynomial. The principle of data-snooping, using the residuals and the w-test, is performed to test the coregistration parameters (see for more information Teunissen (2000b)). In the DORIS cpm-output files information on the least squares estimation of the coregistration parameters can be found, including the offsets in range and azimuth direction, estimated errors, and w-test statistics.

From an analysis of the residuals and their w-test statistics of ten different output files, an error in pixel position in range direction of 0.10 pixels (± 0.07) and an error of 0.07 pixels (± 0.05) in azimuth direction is found. Although these results are obtained from output files of relatively flat areas, it is expected that for areas with more topography variation the errors will also be below one pixel. Therefore, it can be assumed in this study that errors in the coregistration do not influence the time series analysis on pixel base. The possibility that a wrong pixel is included in the time series analysis is minimal. As a consequence, the evaluation of the implemented calibration methods and the selection of permanent scatterer candidates are not influenced by coregistration errors.

Chapter 4

Comparison of SAR Calibration Methods

4.1 Introduction

In the previous chapter two methods to calibrate ERS SAR SLC imagery were presented. Some test results of the implemented ESA calibration method on crops of four selected images from the Las Vegas data stack are given in Section 4.2. Especially, the correction for replica pulse power is discussed. An overview of the size of all ESA calibration correction factors is presented as well. Some test results of the empirical calibration method are presented in Section 4.3.

In Section 4.4 the ESA calibration method is compared with the empirical calibration method described in the previous chapter. Both calibration methods are applied on the Las Vegas data stack. Taking into account the relative long computation time, only resampled crops of 512 by 512 pixels (approximately 2×10 km) of 48 images of the city center of Las Vegas are used as a representation of the whole image. As will be explained in this section, it is expected that this restriction will not influence the results of the comparison, as the variation of the range dependent calibration correction factors between the image time series is relatively small. Two images of the available Las Vegas data set are excluded from the calibration processing: the image with oribtnr. 25394, acquired on 26 May 1996, is used as master image in the coregistration procedure, and with the image with orbitnr. 31272, acquired on 13 April 2001, there were some problems with the processing of the raw SLC data in DORIS. Both calibration methods are compared by analyzing, e.g., the number of selected PSCs and the statistics of amplitude residuals. Based on different criteria it can be evaluated which calibration method, or elements of the calibration method, can best be used for the calibration purpose of this study (diminish the differences between amplitude data of stacked data sets).

To evaluate if the selected permanent scatterer candidates, which have stable amplitude behavior, have also coherent phase behavior, the calibrated crops of complex ERS SAR data are used as input in a processing method for the analysis of permanent scatterers. Some interesting results of the comparison of the selected sets of PSCs and PSs are presented in Section 4.5. From the results of the comparison an approach for a calibration method, that enables time series analysis of amplitude data of all available images in order to select a set of permanent scatterer candidates, is given in Section 4.6.

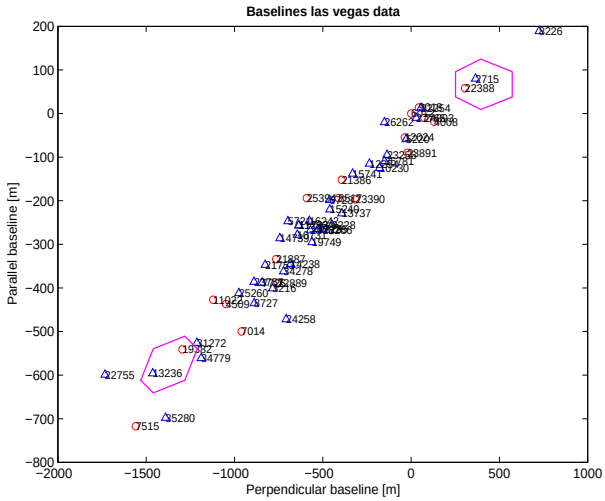

Figure 4.1: Baseline plot of the Las Vegas data set, with the perpendicular baseline $B_\perp$ on the horizontal axis and the parallel baseline $B_{\shortparallel}$ on the vertical axis. The two image pairs that are selected to perform tests on the ESA calibration method are given within the purple polygons.

Orbitnr	mission	date	image size [pixels]	$B_\perp$[m]	$B_{\shortparallel}$[m]
02715	ERS 2	27 Oct 1995	26577 x 4900	365	80
22388	ERS 1	26 Oct 1995	26612 x 4900	305	58
19382	ERS 1	30 Mar 1995	26578 x 4900	−1295	−541
13236	ERS 2	31 Oct 1997	26543 x 4900	−1463	−596

Table 4.1: Selection of four images out of the Las Vegas data set. These images are used to provide first test results of the implemented ESA calibration procedure. The maximum perpendicular and parallel baselines are 1768 and 676 m. Using the geometry in Figure 2.2 and the look angle θ of 23.0 degrees this results in a maximum range variation between the images of about 2 kilometres ($\approx$ 100 pixels).

4.2 Test Results of the ESA Calibration Method

To study the calibration correction factors of the ESA calibration method, four test images are selected from the Las Vegas dataset. A part of the calibration correction factors that are given in Eq. (3.6), depend on the geometry per pixel position. To test the influence of differences in geometry on the calibration parameters, image pairs with large perpendicular and parallel baseline are selected for ERS-1 and ERS-2 (see Figure 2.2 and Figure 4.1). Two image pairs are processed with more or less the same perpendicular and parallel baseline to enable the comparison of ERS-1 and ERS-2. These image pairs are given in Table 4.1.

The ESA calibration correction factors were given in Eq. (3.6), see page **??**:

$$A^2_{c_{ij}} = A^2_{ij} \frac{\sin(\alpha_i)}{\sin(\alpha_{\text{ref}})} \frac{R_i^3}{R_{\text{ref}}^3} \frac{1}{G(\theta_i)^2} \frac{\text{Image Replica Power}}{\text{Reference Replica Power}} \text{Power Loss}_{ij}.$$

Almost all of the correction factors are constant or vary with range direction. Only the powerloss correction varies in both range and azimuth direction. To perform a first test on the geometry dependency of the range dependent correction factors, a correction vector for every line in an image is calculated.

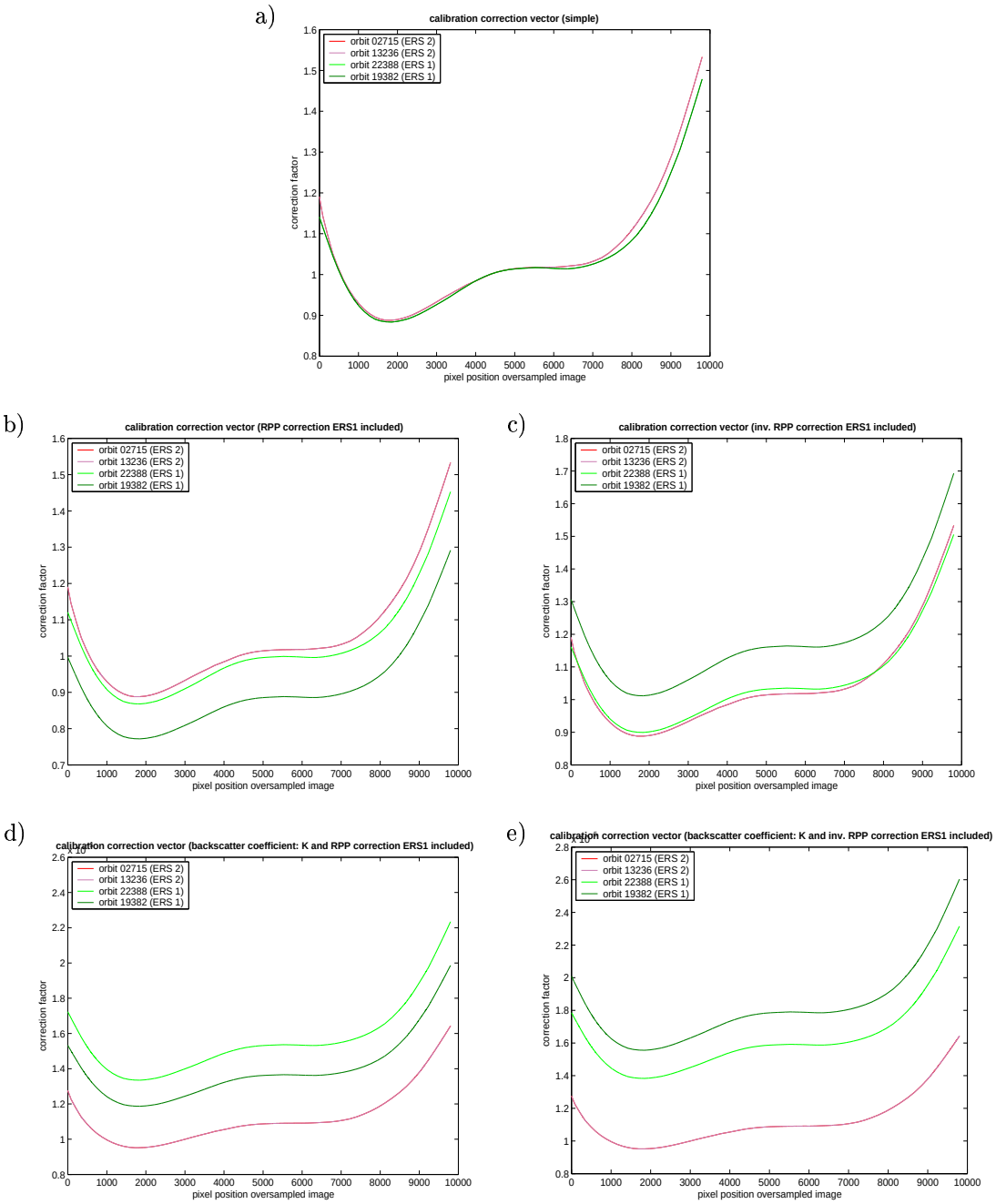

Figure 4.2: Calibration correction vectors that are multiplied with every line of the specific image. On the left part the calibration vectors calculated after the ESA calibration method are presented. The vectors on the right are calculated using an inverse replica pulse power correction, i.e., instead of the factor Replica Pulse Power/Reference Replica Power the inverse of this factor is used. This is done because of the negative effect the RPP correction factor has on the scaling of the histograms (see Figure 4.3). a) 'Simple calibration': incidence angle, range spreading loss, antenna pattern gain. b) and c) 'RPP calibration': replica pulse power correction included. d) and e) backscattering coefficient: calibrated intensity/K. The influence of the ESA calibration method on the ERS-2 images is very small. There is almost no difference after calibration between the ERS-2 images: the calibration vectors for ERS-2 lie on top of each other. The ESA calibration mainly corrects the ERS-1 images. In b) and c) the influence of the calibration is clearly visible for the ERS-1 images, mainly caused by the replica pulse power correction. Note the scale difference between b), c) and d), e). From d) and e) can be seen that the influence of calibration constant K is even larger (see also Table 4.2).

This correction vector is a multiplication of all correction factors except the powerloss correction, as, e.g., the factors shown in Figure 3.10. This vector is different for every image and varies within the image only in range direction. Thus, this vector is the same for every line in a specific image. An example of these vectors is given in Figure 4.2.

In the oversampling and calibration processing very large datasets, containing millions of pixels, are used. As the computing memory to perform the oversampling and calibration steps in Matlab is limited, the images are split up into patches of 1024×1024 pixels. Per patch histograms are made of the amplitude data to analyze the influence of the calibration factors on the data. In Figure 4.3 histograms are presented of the intensity data and the backscattering coefficient before and after applying some calibration correction factors. In the presented histograms three different calibration equations, containing different calibration correction factors, are used to calculate calibrated intensity values. These are:

1. Intensity data before calibration, after oversampling,
2. Intensity data after 'simple calibration':
   correction factors $\frac{\sin(\alpha)}{\sin(\alpha_{\text{ref}})}$, $\frac{R^3}{R^3_{\text{ref}}}$ and $\frac{1}{G(\theta)^2}$,
3. Intensity data after 'RPP calibration':
   'simple calibration' and correction factor for replica pulse power variations.

The same subdivision is made for the backscattering coefficient:

1. Backscattering coefficient: intensity after oversampling/K
2. Backscattering coefficient: intensity 'simple calibration'/K
3. Backscattering coefficient: intensity 'RPP calibration'/K

Results from the analysis of the histograms that are of importance for a correct implementation of the calibration procedure are presented in the remainder of this section.

4.2.1 Influence of the Replica Pulse Power Correction

During the implementation of the replica pulse power correction two problems arise. First, there is a note in the ESA SAR calibration report on the use of this correction factor (see Laur et al. (2002), page 26), mentioning that for data products processed at ESA the ratio for the replica pulse power correction:

$$\frac{\text{Image Replica Power}}{\text{Reference Replica Power}}, \tag{4.1}$$

should be replaced by the ratio between the first chirp average density measured during the image acquisition and a chirp average density of reference of 267.20 for ERS-1:

$$\frac{\text{Chirp average density image}}{\text{Chirp average density reference}}. \tag{4.2}$$

The chirp average density per image can be found in the ESA reserved record area of the "facility data record" of the CEOS product header. Although the byte location is given, it is, due to the unknown

format, impossible to read this variable directly from the CEOS header to the result or log-files using DORIS. However, the BEST software (see web3) contains a tool for reading all parameters from the CEOS header. Comparison of the size of the values obtained from (4.1) and (4.2) for some of the images show practically the same results (see Table 4.2) and, therefore, the first expression is used in this research.

Secondly, it appears from Figure 4.3 that after applying the replica pulse power correction (RPP) the histograms from ERS-1 and ERS-2 seem to be more separated compared to the situation before this correction factor was applied, cf. 4.3b) and c), and e) and f). This is in contrast with what is expected from the calibration in this study. The calibration procedure should diminish the differences between ERS-1 and ERS-2: the replica pulse power correction, which only influences the ERS-1 images (see Figure 4.2), should shift the histograms from ERS-1 and ERS-2 towards each other. As the histograms of the ERS-1 images in Figure 4.3 are situated on the right side of the histograms of the ERS-2 images, a correction factor higher than one is expected. From Table 4.2 can be seen that this is not the case. To evaluate this effect, also an inverse RPP correction is applied to test data set of four images, cf. with Eq. (4.1):

$$\frac{\text{Reference Replica Power}}{\text{Image Replica Power}}. \tag{4.3}$$

The results of this inverse correction on the scaling of the histograms are presented in Figure 4.4. It appears that after applying an inverse replica pulse power correction the histograms of ERS-1 and ERS-2 match better. Therefore, taking into consideration the purpose of the calibration in this study (diminish the differences between images within the data stack, especially the differences between ERS-1 and ERS-2), the inverse of the replica pulse power correction should be applied. However, according to ESA (Cordey, 2004), the correct way to implement the correction for replica pulse power variation is the use of Eq. 4.1. In the processing of raw radar data a replica pulse is used in such a way that it should be removed using this equation and not its inverse. In the comparison presented in Section 4.4, the ESA method, as described by Laur et al. (2002), is applied to the Las Vegas data set. This way, a critical evaluation of the ESA method, as presented in the ESA calibration document, can be made.

To describe the influence of the calibration using the inverse replica pulse power correction on the selection of PSCs, some test results are presented in Section 4.6.3. Nevertheless, this effect needs to be analyzed more extensively in further research, using other images, and compare the results from this inverse ESA calibration with results from the ESA and empirical calibration method.

4.2.2 Size of the ESA Calibration Factors

To evaluate the importance of the sequence of ESA calibration factors, an analysis of the variation in size of different calibration factors is made. An overview of this variation of the calibration factors for the four selected images is given in Table 4.2. As explained in Section 3.3.3, the factors in the first two lines of this table, the correction for incidence angle and range spreading loss, depend on variation in satellite geometry. The values of these range dependent correction factors show the same variation from near range to far range in all four images. Thus, although these images were selected based on the largest perpendicular and parallel baselines to test the influence of variation in satellite geometry on the calibration parameters, there seem to be no difference for these correction factors between the images. The maximum range variation between the images is 2 km, which corresponds to about 100 pixels. A range variation of 100 pixels corresponds to a variation in the correction factor for incidence angle of 0.006 and a variation in the correction factor for range spreading loss of 0.003. Comparing these values with the variation for replica pulse power of values up to 0.14 or the variation of the influence of calibration constant K of 0.44 (see Table 4.2), the influence of the incidence angle and range spreading loss correction can be neglected.

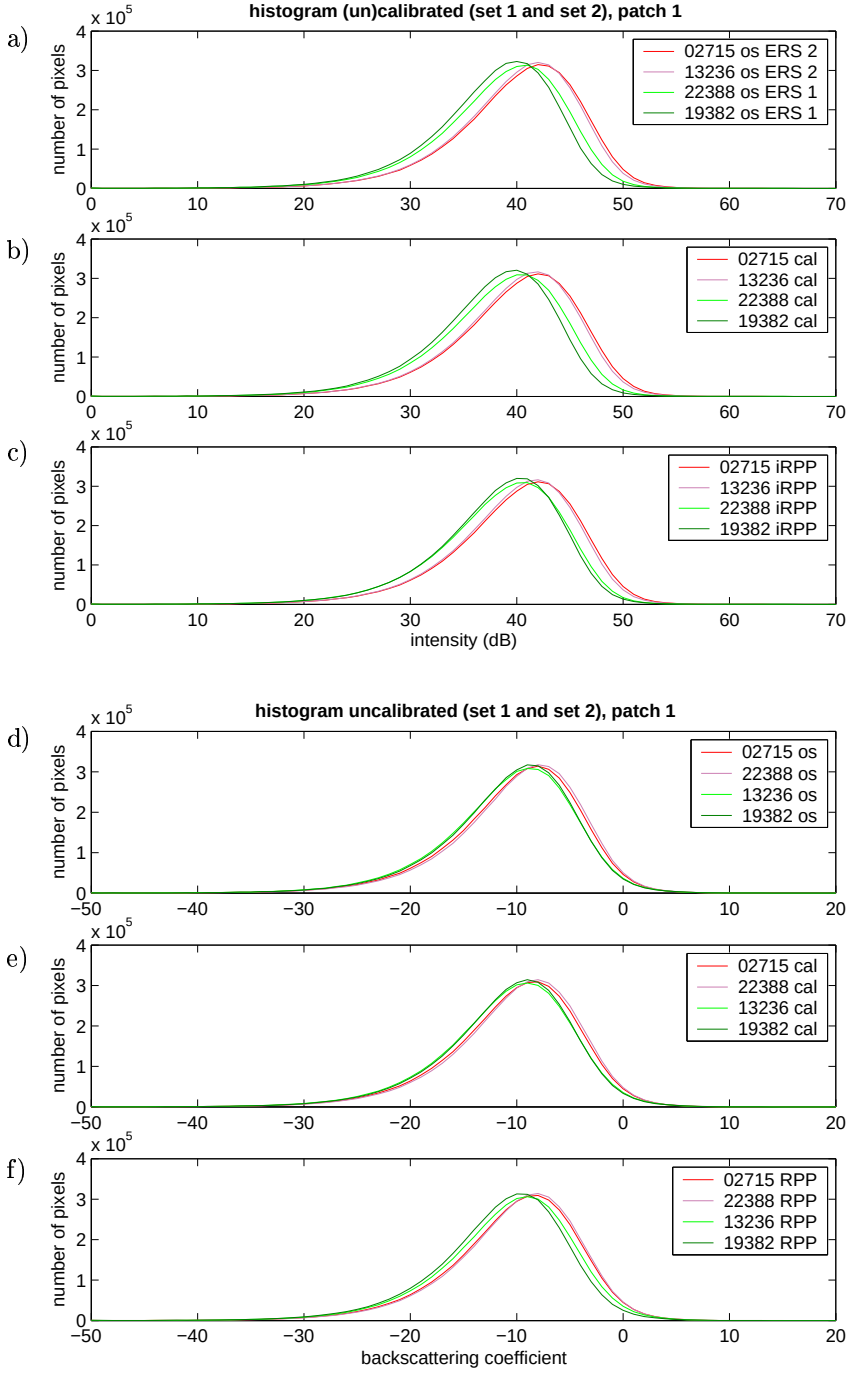

Figure 4.3: Histograms of intensity values and backscattering coefficients of patch 3,1 (line 4097-6144, pixel 1-2048 of the oversampled image) of the four test images before and after calibration steps. a) Intensity values in decibels after oversampling (os), b) after 'simple calibration' (cal), and c) after 'RPP calibration' (RPP). These intensity values are divided by calibration constant K, resulting in the backscattering coefficient σ^0. This results in d) the backscattering coefficient before calibration (os), e) after 'simple calibration' (cal), and f) after 'RPP calibration' (RPP). From a) and d) it becomes clear that calibration constant K is the most important factor: if only this factor is applied to the oversampled data, the histograms are already more or less on top of each other. Comparing e) and f), it can be seen that the replica pulse power correction has an inverse effect: the histograms are more separated after applying this correction.

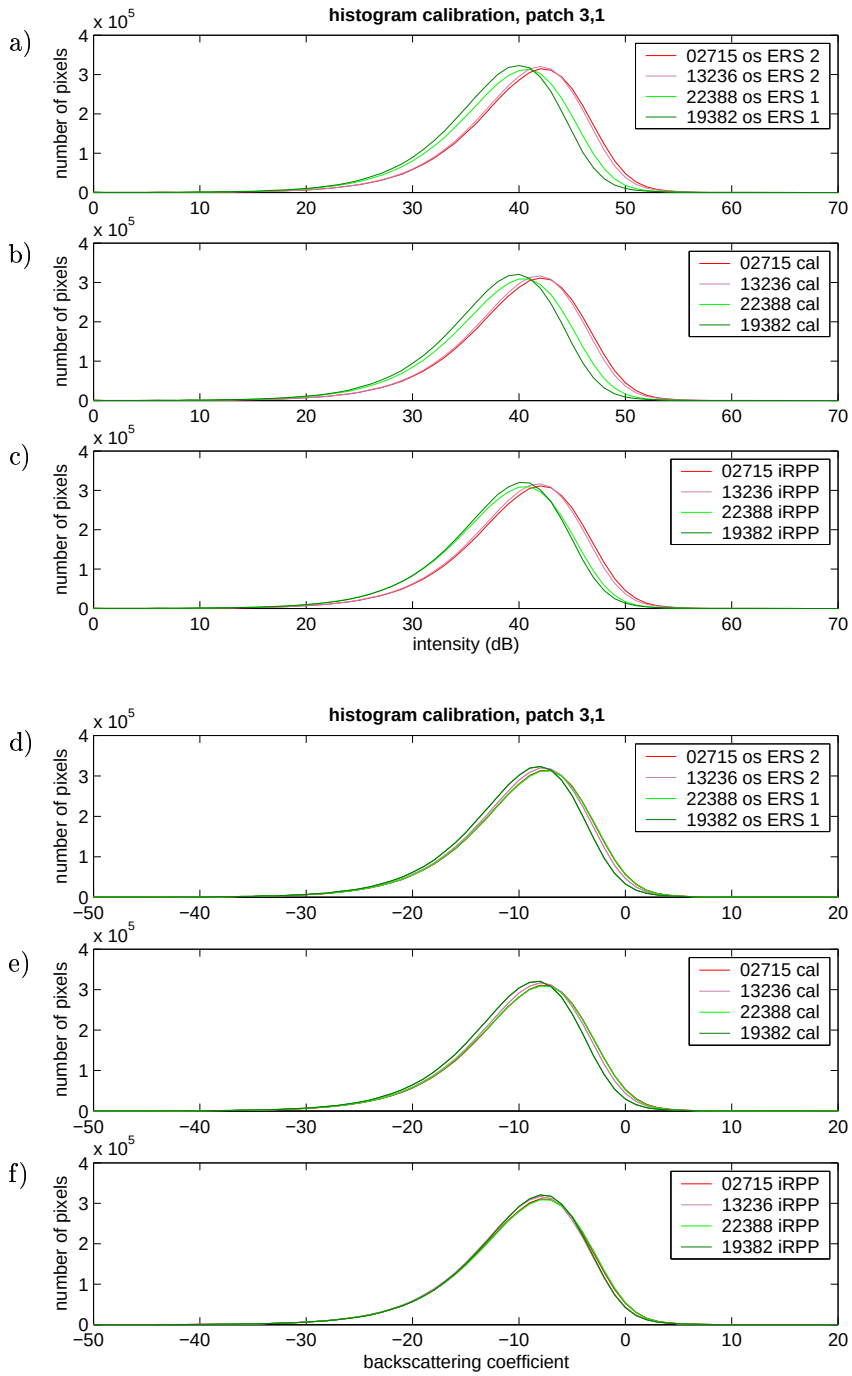

Figure 4.4: Compare this figure with Figure 4.3: instead of the replica pulse power correction the inverse of this correction, as given in (4.3), is applied to patch 3,1 (line 4097-6144, pixel 1-2048 of the oversampled image). a) Intensity values in decibels after oversampling (os), b) after 'simple calibration' (cal), and c) after 'inverse RPP calibration' (iRPP). The backscattering coefficient is given in d) before calibration (os), e) after 'simple calibration' (cal), and f) after 'inverse RPP calibration (iRPP)'. It appears that the histograms matches better after applying this inverse correction. This is best seen after the intensity values are divided by K in the histograms in e) and f).

Correction	02715 (ERS-2)	22388 (ERS-1)	13236 (ERS-2)	19382 (ERS-1)
$\frac{\sin(\alpha)}{\sin(\alpha_{\text{ref}})}$	0.85 - 1.14	0.85 - 1.14	0.85 - 1.14	0.85 - 1.14
$\frac{R^3}{R^3_{\text{ref}}}$	0.94 - 1.08	0.94 - 1.08	0.94 - 1.08	0.94 - 1.08
$\frac{1}{G(\theta)^2}$	0.93 - 1.49	0.92 - 1.42	0.93 - 1.49	0.92 - 1.42
RPP	1.00	$\frac{201.607}{205.229} = 0.9823$	1.00	$\frac{179.259}{205.229} = 0.8734$
chirp average density	1.00	$\frac{261.618}{267.20} = 0.9791$	1.00	$\frac{233.453}{267.20} = 0.8737$
inverse RPP	1.00	$\frac{205.229}{201.607} = 1.02$	1.00	$\frac{205.229}{179.259} = 1.14$
$\frac{K_2}{K_i}$	1.00	$\frac{65026.0}{93325.3} = 1.44$	1.00	$\frac{65026.0}{93325.3} = 1.44$

Table 4.2: Overview of the variation of the ESA calibration correction factors for four test images of the Las Vegas data set. The upper three corrections are range dependent, the other corrections are constant per image. As the first three corrections factors in this table are almost the same, and as the range variation between the images is maximum 2 km (about 100 pixels), these correction factors can be neglected for the calibration in this study. The variation of the range dependent correction factors between these images is for the incidence angle correction 0.006, for the range spreading loss 0.003 and for the antenna pattern gain 0.011. This is far less than the variation between the images for replica pulse power (0.14) and the scaling using calibration constant K (0.44), which are the two important factors for this study. The correction factor using the chirp average density, that should be applied to ERS-1 imagery instead of the replica pulse power correction according to the ESA document Laur et al. (2002), is approximately the same as the replica pulse power correction. As the latter is easier to derive, this factor is used in the calibration.

The same is the case for the antenna pattern gain correction, which is only slightly different for ERS-1 and ERS-2. The antenna pattern gain correction is obtained form different look up tables, depending on the date of processing and used sensor (ERS-1 or ERS-2). Also separate tables for UK-PAF imagery are available. For the Las Vegas imagery only the difference for used sensors are of importance, as all images are processed after 21st January 1997 and, as a consequence, only two different look up tables are used: one for ERS-1 and one for ERS-2. The main consequence of applying these three range dependent correction factors is that the intensity values are more balanced over the whole image. Their contribution to the calibration purpose in this study, diminish the differences between ERS-1 and ERS-2 images, can be neglected, as these correction factors do not differ much between the images.

In Figure 4.3 and 4.4 it is shown that the most important factors that reduce the difference between ERS-1 and ERS-2 are the replica pulse power correction and the use of calibration constant K. These correction factors are constant per image. For the Las Vegas data set only two different calibration constants K have to be obtained from the look-up tables for the same reason as described for the antenna pattern gain correction: a calibration constant for all ERS-1 images and a calibration constant for all ERS-2 images. The replica pulse power correction is only applied to ERS-1 and varies per image. The variation of these factors between ERS-1 and ERS-2 images is large compared to the other correction factors, both correction factors are important for the calibration in this study. The influence of K is three times larger than the influence of the replica pulse power correction. Therefore, results of a calibration method using only calibration constant K are presented in Section 4.6.2.

Finally, the powerloss correction factor varies in both range and azimuth direction. In general it shows a pattern that follows the characteristics of the Earth's surface within the SAR images as can be seen from Figure 3.8. The correction is larger for ERS-1 due to reduced gain settings of ERS-2. It appears from this figure that the powerloss correction factors are most of the time larger than one, resulting in higher amplitudes values in most parts of the image to compensate for the loss of power. An analysis of the variation of the powerloss correction over the image time series shows more or less the same pattern for all images. As the powerloss corrections factors do not differ significantly for the same areas in different images, these factors are not important factors for this study. The influence of the different ESA calibration factors on the selection of permanent scatterer candidates is described in more detail in Section 4.6.1.

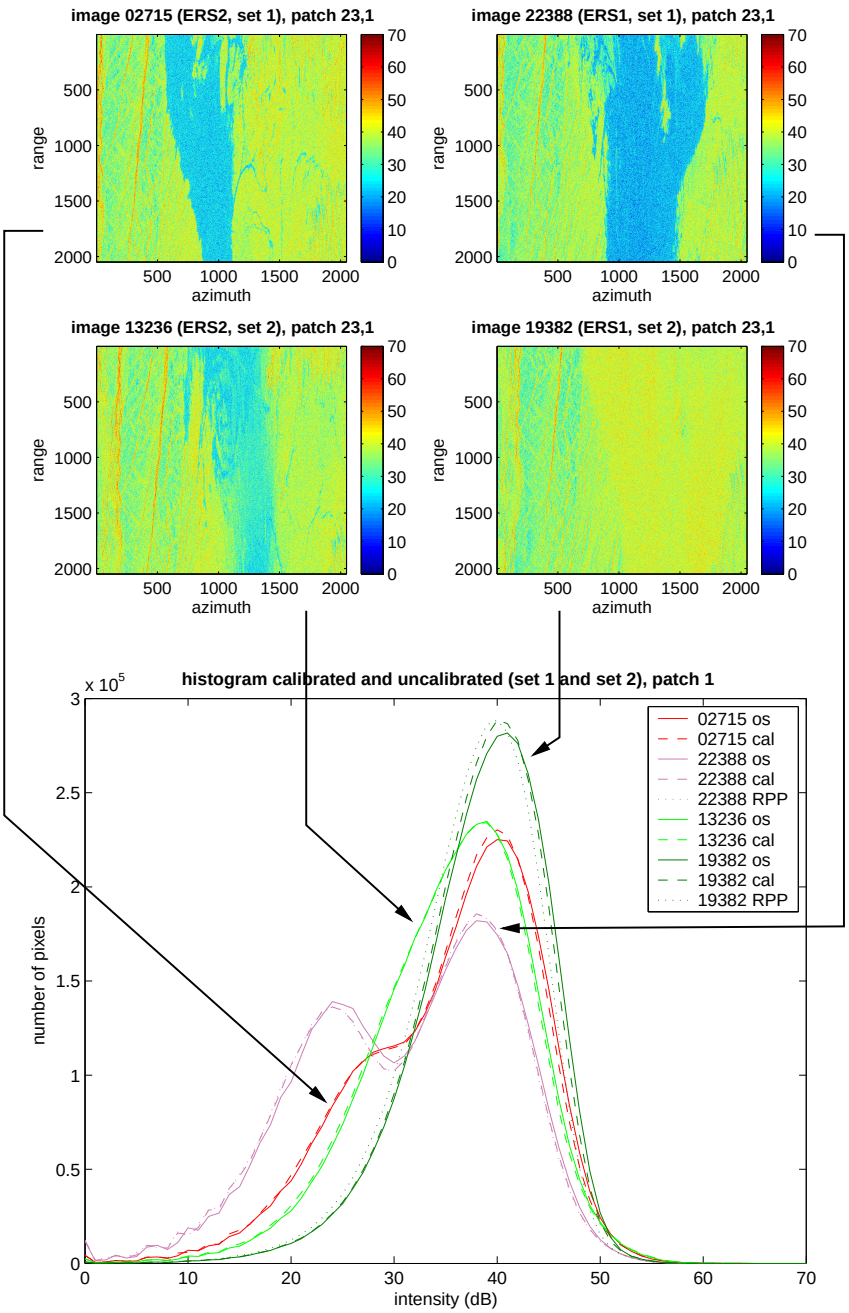

Figure 4.5: Example of temporal decorrelation: a lake is situated in the center of an image patch. When comparing the four selected images, some striking differences between the histograms (under) occur, caused by the changing level of backscatter of the lake in different seasons (in this case spring and autumn, see dates in Table 4.1). Therefore, this patch useless for calibration.

4.2.3 Influence of Temporal Decorrelation

When performing a histogram analysis one should be careful which area or image patch to choose. The assumption for calibration is that the influence of temporal decorrelation on point scatterers that are used in the permanent scatterer technique is limited. Therefore, if strong temporal decorrelation effects are present, this can disturb the distribution of the histogram. Therefore, it is impossible to perform comparison based on the histograms, as, e.g., done in Section 4.4. Also empirical calibration methods, based on scaling of amplitude histograms, are not possible for these areas with strong temporal decorrelation.

An example of an area showing strong influence of temporal decorrelation is given in Figure 4.5. Especially the amplitude histogram of ERS-1 image 22388 acquired in October 1995 show strong deviations. This is due to changing water level of the lake, situated in the middle of this crop, that causes different backscatter levels. The presence of many water resolution cells causes a peak in the histogram at 25 dB.

4.3 Test Results of the Empirical Calibration Method

In this section some test results of the implemented empirical calibration method are presented. As described in Section 3.4, this calibration method is based on the estimation of a constant calibration factor c_k per image, using time series of amplitude data. Unlike the ESA method, which can be applied for every single ERS SAR image, the empirical method requires the use of more images to estimate the calibration factors. As the empirical method is based on the amplitude data, the influence of temporal decorrelation should also be taken into consideration. Areas that show large temporal decorrelation effects can disturb the estimation of the c factors.

The number of PSCs that are selected is determined by a chosen threshold value for the dispersion index. In general, a value of 0.25 chosen, as this provides the highest detection rate. Besides, if the dispersion index is higher than 0.25, the amplitudes are not Gaussian distributed and the dispersion index is no longer a good selection criteria for selecting points with coherent phase behavior. The selected number of PSCs increase significantly when changing the threshold value of D_A, as shown in Figure 4.6. Here, the number of selected PSCs are shown for varying threshold values for the dispersion index, for both the raw oversampled data set, which is used for the initial selection of PSCs that are used to estimate the calibration constants c_k, and the empirical calibrated data set. The number of PSCs that are selected after the empirical calibration is performed is larger than before calibration, i.e., more points are pointed out to be stable: the detection rate of PSCs is larger.

The number of PSCs that are equal in both data sets are also shown in this figure. Note that not all pixels that were selected from the raw oversampled data are selected again from the empirical calibrated data set. This is a consequence of applying different calibration correction factors to different images, resulting in different values for the dispersion index per pixel (μ and σ change). To test whether the selected pixels can be used in the permanent scatterer processing, the phase coherence of these pixels has to be analyzed over time. This way PSCs can be identified that are incorrectly marked as stable points, i.e. the false detection rate can be determined. This is discussed in Section 4.5, where a first version that uses the permanent scatterer technique analysis is used to identify permanent scatterers that show large phase coherence over time.

From Figure 4.6 it becomes clear that more PSCs are selected after the data is calibrated, but also when the threshold value of the dispersion index is increased. This suggests that the same results for the selection of PSCs can be achieved by applying just another (higher) threshold value for the dispersion index for the oversampled raw data, as for the calibrated data using a lower threshold value. However, from Table 4.3 can be seen that this is not the case. In the first and second column the dispersion index for the empirical calibrated and oversampled raw data is given that needs to be chosen to select the

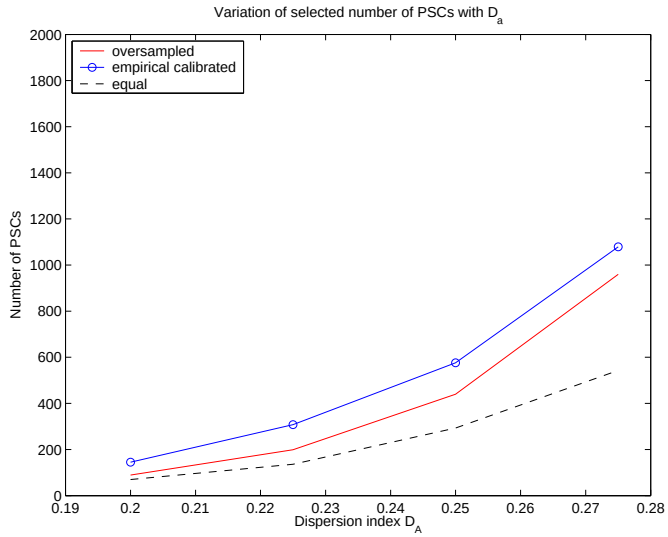

Figure 4.6: Variation of the number of selected PSCs with changing threshold values for the dispersion index. The red line denotes the number of PSCs selected from the raw oversampled data. This initial set of PSCs are used for the estimation of the empirical calibration constants c_k per image. The blue line gives the number of selected PSCs after the data is calibrated using the empirical method. The dotted black line gives the number of selected PSCs that are equal for both data sets. The number of PSCs that are selected increase after calibration, i.e., the detection rate is higher after calibration.

number of PSCs given in the third column. By increasing the threshold value for the oversampled raw data the same number of PSCs are selected, as were selected from the empirical calibrated data with a lower threshold value. However, these are not the same points. In the last column the number of PSCs are given that are equal in both data sets. Only 82% of the number of selected PSCs given in the third column is equal in both data sets. Therefore, it is not possible to replace the calibration of SAR images by just choosing an higher value for the dispersion index and apply this to the oversampled raw data set: other points will be selected after the calibration.

More test results on the empirical calibration method can be performed if the approach presented in Appendix B will be implemented. Then, in further research, an analysis of the residuals and the standard deviation of the estimated calibration constants c_k can be performed to obtain a critical validation of the empirical calibration method.

D_A (emp.cal.)	D_A (ovs raw)	Number of PSCs	Number of equal PSCs (%)
0.200	0.217	145	119 (82.1%)
0.225	0.238	308	251 (81.5%)
0.250	0.257	576	477 (82.8%)
0.275	0.279	1079	888 (82.3%)

Table 4.3: Overview of the threshold values that are needed to select the same number of PSCs from the oversampled raw data and the empirical calibrated data. The first column gives the threshold values for the dispersion index used to select the number of PSCs, given in the third column, from the empirical calibrated data set. The corresponding dispersion index that is needed to select the same number of PSCs from the oversampled raw data is given in the second column. In the last column the numbers of selected PSCs that are equal in both data sets are given, with the percentage between the brackets. Although it is possible to select the same number of PSCs from both data sets by changing the threshold values, it is not possible to replace the calibration procedure by choosing just another higher threshold value for the oversampled raw data set, for almost 20% of the selected pixels are different for both data sets.

4.4 Comparison of the ESA and Empirical Calibration Method

To compare the ESA and empirical calibration procedure resampled crops of a part of the city center of Las Vegas are analyzed. The size of the original crop is 512×512 pixels (pixel 23000-23511 in azimuth and 2000 - 2511 in range direction from the original image of about 26000×4900 pixels). The size of the area is about 21 squared kilometers: over 2 kilometers in azimuth direction and over 10 kilometers in range direction. The resulting datasets after calibration will have twice the pixel size, due to the oversampling by a factor two. Three different data sets are compared:

- Oversampled data by factor two, i.e., oversampled 'raw' SLC data
- Oversampled and calibrated data, according to the ESA method
- Oversampled and calibrated data, according to the empirical method

The implemented calibration methods are analyzed using different methods. In the following sections, an analysis of the number of selected PSC, the possible improvement of the dispersion index per pixel, the variation of the calibration factors of the empirical calibration method and some statistics on amplitude residuals are discussed.

Based on the following three criteria, it is decided which calibration method, or which elements of the calibration methods, are most important for the calibration purpose in this study (derive a data set of images, of which the differences in amplitude between the images, caused by, e.g., the use of different sensors or varying satellite geometry, are minimal, to enable a time series analysis of the amplitudes on pixel base to select PSCs).

1. *Detection rate of PSCs*

   The number of selected PSCs after calibration should be as high as possible. A high detection rate after calibration ensures that enough PSCs are available to use as input for the permanent scatterer analysis to estimate deformation profiles, even outside urban areas where less strong stable points scatterers are present. The detection rate is specified the number of PSCs that are selected using a specific calibration method as a precentage from the total number of different PSCs (selected from all data sets: oversampled raw, ESA and empirically calibrated). A stable amplitude over time is needed, as the selection of PSCs is based on the dispersion index: the ratio between the standard deviation and mean of the amplitudes over the image time series.

2. *False detection rate of PSCs*

   The selection of PSCs is based on a analysis of time series of amplitude data. This way, point scatterers are selected, using the dispersion index $D_A = \frac{\sigma_A}{\mu_A}$, that have a stable amplitude behavior. However, these scatterers should also have coherent phase behavior, as the permanent scatterer analysis is based on points that are coherent over time. Therefore, only points that show coherent phase behavior over time should be selected and marked as PSCs, i.e., the false detection rate should be as low as possible. The false detection rate is defined as the percentage of selected PSCs based on amplitude data, that do not show a coherent phase behavior. A first analysis of this false detection rate is presented in Section 4.5 using a first implemented version to analyze permanent scatterers.

3. *Computation time*

   Although the criterion described above are the most important to decide which of the calibration methods is the best method to be used for the calibration in this study, the differences in computation time can also be of importance. If the difference between the computation time is large, and the results of the PSCs selection do not differ much, the calibration method that has the lowest

computation time can be preferred. Besides, elements that are not important for the purpose of the calibration in this study should be omitted, as this will reduce the computation time of the calibration. More attention on the reduction of computation time is given in Section 4.6.

4.4.1 Amplitude Variation of PSCs per Image

The aim of the calibration in this study is to provide a stable time series of amplitude data to enable selection of PSCs. Especially the difference between ERS-1 and ERS-2 imagery should be reduced after calibration. Therefore, the amplitude variation of the PSCs per image is analyzed. In Figure 4.7 the mean of the amplitudes values of the PSCs per image are shown.

For the first 40 images, the amplitude pattern after ESA calibration (blue line) is more or less stable: the differences between ERS-1 and ERS-2 imagery is reduced after applying the different ESA calibration factors. As the replica pulse power correction is only applied for ERS-1 imagery and all images are scaled to ERS-2 by using calibration constant K, the amplitude values of ERS-1 are mainly influenced by the ESA calibration method. The empirical calibration method (green line) shows also a more stable pattern for the amplitude values of the PSCs for this part of the image time series compared to the pattern of the raw oversampled data (red line), although this pattern is not as stable as for the ESA calibration method. The empirical method applies corrections to both ERS-1 and ERS-2 imagery. This results in an amplitude pattern with higher values than the original raw oversampled data when 48 images are used. If only 44 images are used the amplitudes are lower. This is caused by the fact that both ERS-1 and ERS-2 images are scaled. From Figure 4.7 and Table 4.4 it appears that for both the ESA and the empirical calibration method the amplitude values are more stable compared to the oversampled raw data. The empirical calibration method shows the most stable results. Therefore, this calibration method seems to the most applicable for the calibration in this study. However, more test have to be performed on other crops or data sets to confirm these results.

	48 images:		**44 images:**	
Data set	**mean [dB]**	**std [dB]**	**mean [dB]**	**std [dB]**
Oversampled 'raw'	54.20	1.00	54.19	0.62
ESA calibration	54.52	0.99	54.27	0.36
Empirical calibration	55.30	0.49	54.13	0.19

Table 4.4: The mean and standard deviation of the amplitude variation of the PSCs over the image time series. The empirical calibration method shows the most stable results. This method, that scales both ERS-1 and ERS-2 imagery, has the lowest standard deviations.

4.4.2 Number of Selected Permanent Scatterer Candidates

For each of the three datasets a matrix containing dispersion index values per pixel position is calculated using Eq. (3.23), page 29:

$$D_A = \frac{\sigma_A}{\mu_A}.$$

From this matrix all pixels with $D_A < 0.25$ are selected and marked as permanent scatterer candidates. As can be seen from Figure 4.8 and Table 4.5 the number of selected PSCs increase significantly after calibration. For the empirical calibration method 29.1%, and for the ESA calibration 30.3% more pixels are selected with respect to the selection performed on the oversampled raw data (and 19.7% and 25.2% when 44 images are used). In the second columns of the tables in this section the number of PSC are

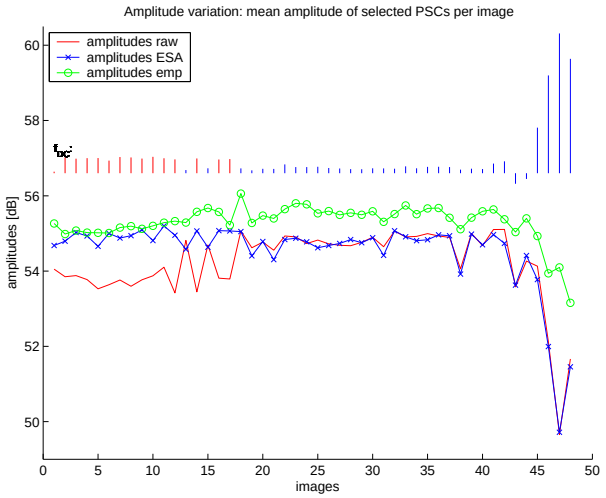

Figure 4.7: Variation of mean amplitudes of all selected PSC per image. The last images show a large drop in the amplitude value upt to 5 dB. This is probably caused by the large Doppler centroid frequencies that influence the observations in the image. The lines in top of the image give an impression of the variation of the Doppler centroid frequencies: the red lines are ERS-1 and blue lines are ERS-2 imagery. In this figure the influence of the calibration methods on the decrease of differences between ERS-1 and ERS-2 imagery is shown.

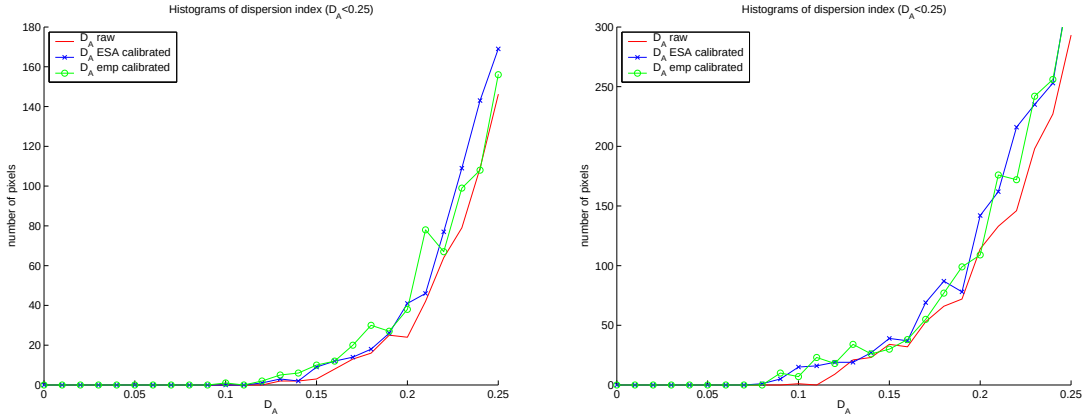

Figure 4.8: Histogram of dispersion index for $D_A < 0.25$ for the oversampled raw data, ESA calibrated and empirically calibrated data from 48 images (left) and 44 images (right). In the right figure the images that have a large Doppler centroid frequency of over 400 Hz are excluded, as these images disturb the calibration (see Section 4.4.4). Note the scale differences between the images: the histograms of all data sets are more shifted to the left. As a consequence, more PSCs will be selected, i.e., the detection rate is higher. This is logical, as the images with high Doppler centroid frequency are excluded, and fewer images are used in the time series analysis to select stable points. Note that the histograms after calibration lie on the left side of the histogram of the raw oversampled data. This indicates that more PSCs are selected after calibration, when the same threshold value for the dispersion index is used. The exact number of selected PSCs are given in Table 4.5.

Number of selected PSCs in:	48 images	44 images	equal in both data sets
Oversampled 'raw' data	446 (21 per km^2)	1269 (60 per km^2)	438 (98.2%)
ESA calibration data	581 (28 per km^2)	1589 (76 per km^2)	578 (99.5%)
Empirical calibration data	576 (27 per km^2)	1519 (72 per km^2)	563 (97.7%)

Table 4.5: Number of selected PSCs with dispersion index: $D_A < 0.25$. The selected numbers of PSCs (per km^2) in the first column are obtained from 48 images. The second column represents the results for 44 images, with have a low Doppler centroid frequency (see Section 4.4.4). Between brackets an indication of the number of PSC per squared kilometer is given. The last column gives the number of selected PSCs that are the same for both data sets. The percentage of this number of the total selected PSCs from 48 images is given between the brackets: almost all pixels that are selected from 48 images are also selected when 44 images are used. Almost three times more PSCs are selected when only 44 images are used, which is logical as only the best images are included in the time series analysis. Note that up to 30% more PSCs are selected after calibration.

Equal number of selected PSCs in:	48 images	44 images
Oversampled 'raw' and ESA calibration	363 (42.0%)	1084 (58.0%)
Oversampled 'raw' and empirical calibration	293 (33.9%)	1160 (62.1%)
ESA calibration and empirical calibration	334 (38.7%)	1321 (70.7%)
Oversampled 'raw', ESA calibration and empirical calibration	251 (29.1%)	1056 (56.1%)

Table 4.6: The number of selected PSCs with a small dispersion index: $D_A < 0.25$ that are the same in the different specified data sets. Between the brackets the percentage of this number of the total number of PSCs that are selected using all different data sets (844 PSCs using 48 images and 1868 PSCs using the 44 images with low Doppler centroid frequency) to analyze the similarity between the data sets. The similarity between the data sets is larger when only 44 images are used. Especially the correspondence between the ESA and empirically calibrated data set improves, when images with high Doppler centroid frequency that disturb the empirical calibration are excluded (see Section 4.4.4). Still, the correspondence between the PSCs from different data sets is low.

given if only the 44 images are processed that have a 'normal' Doppler centroid frequency up below 400 Hz. This selection of images is made to see whether there is improvement or change in the behavior of the standard deviation of the amplitude values using the empirical calibration, if the images that have a large Doppler centroid frequency of over 400 Hz are excluded. This is explained in more detail in Section 4.4.4. These 44 images are the images from the Las Vegas dataset that are acquired from 21 April 1992 to 20 October 2000. Moreover, image 25394 (26 May 1996) is not in the processing as this image is chosen to be the master image in the coregistration step. If only 44 images are used, the number of selected PSCs increase significantly: almost three times more PSCs are selected (see Table 4.5). This is logical, as only images that have relatively stable amplitude values for the PSCs over the image time series are included in the selection (see also Figure 4.7).

Table 4.6 shows the number of corresponding selected PSCs in the different data sets. The correspondence is expressed using a percentage of the total number of PSCs that are selected from the oversampled raw, ESA calibrated, and empirically calibrated data. In total, 864 PSCs are selected using 48 images, and 1868 PSCs using 44 images. The correspondence between the ESA and empirically calibrated data is larger if the images with large Doppler centroid frequency are excluded: 38.7% and 70.7% of the total number of selected PSCs. However, there are serious differences between the results of the ESA and empirical calibration method. For example, only 334 PSCs are selected by both of the ESA calibration method end the empirical calibration method (38.7% of the total number), i.e., only 58% of the PSCs selected after the ESA calibration method are also selected after an empirical calibration is performed on the data set of 48 images. The results for 44 images are better: about 83 percent of the selected PSCs after ESA calibration is also selected after the empirical calibration is performed. In Table 4.7 the number of selected PSCs are given with the percentage of the total number of different PSCs that are selected from the oversampled raw, ESA and empirically calibrated data sets. Also the union of number of PSCs that are selected from the ESA calibration and empirical calibration is shown here, which is 95% of the total amount of selected PSCs. The highest detection rate is achieved after the data is calibrated using

Total number of selected PSCs in:	48 images	44 images
Oversampled 'raw', ESA calibration and empirical calibration	864 (100%)	1868 (100%)
ESA calibration, empirical calibration	823 (95.3%)	1787 (96.0%)
Oversampled 'raw'	446 (51.6%)	1269 (67.9%)
ESA calibration	581 (67.3%)	1589 (85.1%)
Empirical calibration	576 (66.7%)	1519 (81.3%)

Table 4.7: Total number of selected PSCs from the different data sets. The number of PSCs in the first two lines of the table are derived using the union operator, e.g., the total number of different PSCs that are selected from 48 images is 864 PSCs. Between the brackets the percentage of the PSCs, obtained from the (combination of) data sets specified in the first column, of the total number of different PSCs is given. From this table can be seen that the ESA calibration method provides the highest detection rate of PSCs (67.3% and 85.1%).

the ESA method (67.3% for 48 images). Again, from this table can be concluded that the detection rate is higher when less image are used. Still the ESA calibration method gives the best results, considering the detection rate.

In Figure 4.9 the spreading over the images is shown. The increasing number of selected PSCs when only 44 images are used can be seen from this figure, cf. Figure 4.9a) and b). In Figure 4.9c) an enlargement of a part of the SAR images is shown. This figures shows that most of the PSCs that are selected are part of larger clusters of PSCs. Most of the time, these clusters of PSCs originate from only one dominant scatterer, and the neighboring pixels are side-lobes of this scatterer. As only this dominant scatterer should be used in the subsequent PS processing, further research is required to analyze how many of this PSCs are clustered. Then, a better comparison between the different data sets can be performed. This effect can be tested in future research by estimating, e.g., a sinc-pattern based on the amplitude values through the PSCs cluster (or more sinc-patterns in case more dominant scatterers are present).

Based on the results of the analysis of the number of selected PSCs the following conclusions can be drawn.

- The detection rate of PSCs is higher after the data is calibrated. For the ESA calibration method and 30.3% and 25.2% (48 and 44 images) more PSCs are selected, and for the empirical method 29.1% and 19.7%. From Table 4.7 can be seen that the ESA method has the highest detection rate: 67.3% and 85.1%, vs. 66.7% and 81.3% for the empirical method. Based on only the detection rate, it can be concluded that the ESA calibration method is the best method to use for the calibration in this study.
- More PSCs are selected if only images with low Doppler centroid frequencies are used: 864 vs. 1868 PSCs (see also results in previous point), i.e., the detection rate is higher and the total number of selected PSCs increase significantly (116.2%). This is a logical result, as the unstable images are not used in the analysis. To obtain the best detection rate, images that have a high Doppler centroid frequency should be excluded.
- Large differences between the points that are selected by the ESA and the empirical calibration method are present. Only 38.7% of the total number of selected PSCs for 48 images is selected by both the ESA and empirical method. The correspondence is better when only 44 images are used: 70.7% are selected by both methods. Thus, there are large differences between the data sets.

Regarding the detection rate, the ESA method shows slightly better results than the empirical calibration method. However, as both methods are able to select enough PSCs to use as input for the permanent scatterer analysis, also the false detection rate has to be analyzed, i.e., it is important to know if the selected PSCs have also coherent phase behavior. This is done in Section 4.5 by analyzing the phase coherence of the PSCs over time.

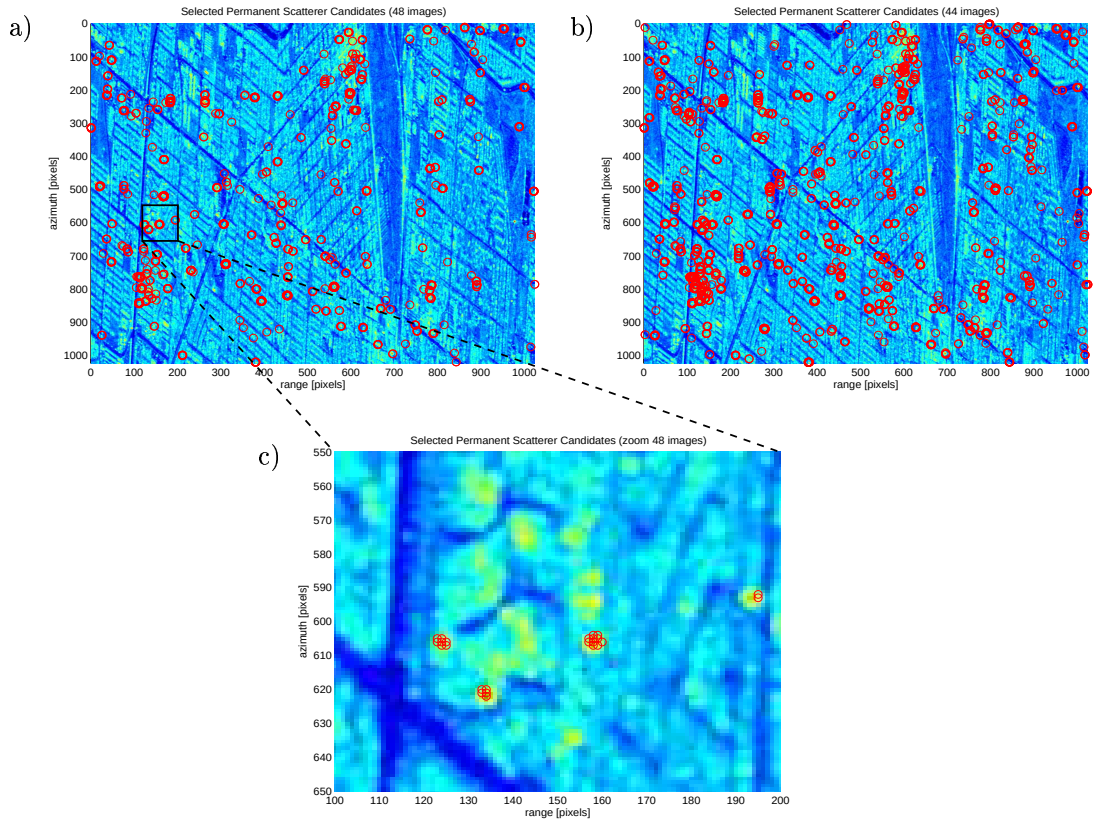

Figure 4.9: Spreading of the selected permanent scatterer candidates from all data sets. a) 48 images and b) 44 images (more points selected). c) Zoom: PSCs clustered. The similarity between the data sets for 44 images is better than for 48 images (see also Table 4.7).

4.4.3 Improvement of Dispersion Index

It is expected that after applying the calibration the dispersion index per resolution cell will be lower, as the calibration should stabilize the amplitudes values over the image time series, and, as a consequence, the standard deviation should be lower. In Figure 4.10 histograms of the mean amplitude, standard deviation and dispersion index D_A are shown. The improvement of D_A after calibration should be visible in the histogram of D_A by a slight shift to the left. The right side of this figure presents the same parameters if only the first 44 images are included in the processing. From Figure 4.10 the following conclusions can be drawn:

- *Regarding the mean of the amplitudes:*
  The mean amplitudes values are a bit larger after the ESA and empirical calibration method. Both calibration methods show more or less the same results.

- *Regarding the standard deviation of the amplitudes:*
  Almost the same results appear for the standard deviation of the amplitudes from the oversampled raw data and the ESA calibrated data. The standard deviation of the empirical calibrated data deviates from the other histograms of the standard deviation, if all 48 images are included. If only 44 images with 'normal' f_{DC} are used, there is no difference any more, and almost the same results can be seen for both calibration methods.

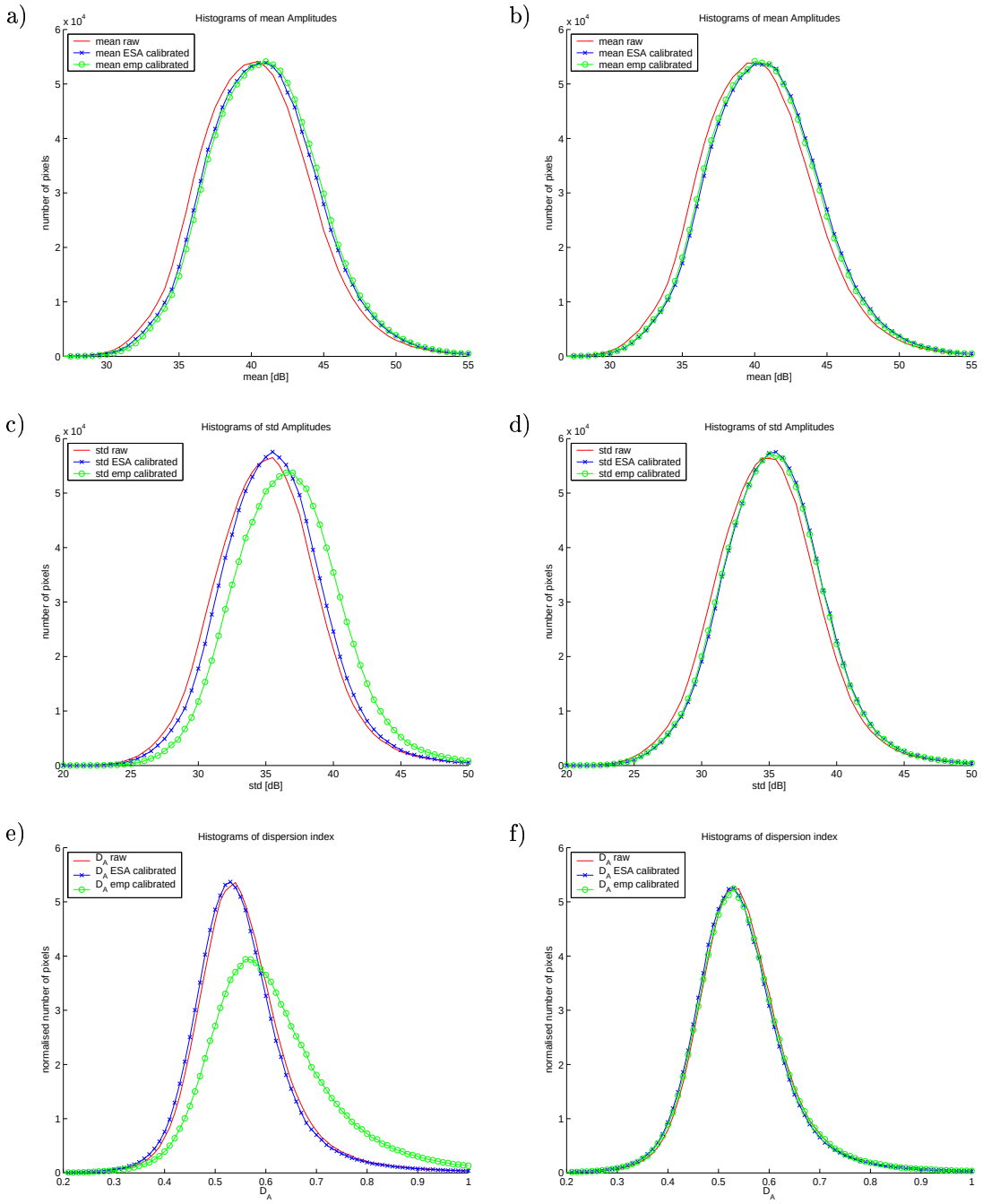

Figure 4.10: Histogram of mean [dB], standard deviation [dB] and dispersion index of all amplitudes of the three test datasets. On the left side histograms for 48 images are given. The histograms on the right side only represent the first 44 images with low Doppler centroid frequency. Important differences can be seen for the standard deviation and dispersion index.

- *Regarding the dispersion index:*
  Although in Figure 4.10 the expected shift of the histogram to the left is hardly visible, a slight improvement, i.e., a shift to the left, can be seen when comparing enlargements of the histograms for $D_A < 0.25$ as given in Figure 4.8. Again, the dispersion index of the empirical calibrated data show a different pattern if all 48 images are included in the calculation. This is logical, as the dispersion index is related to the standard deviation.

From test results presented in Section 4.3, of an analysis on the shift of the threshold values of the dispersion index, it became clear that is possible to select the same number of PSCs from both the empirically calibrated and oversampled raw data by increasing the threshold value for the oversampled raw data set. However, it is not possible to replace the calibration method by the only a shift of D_A, as other points are selected from both data sets.

4.4.4 Analysis of Calibration Factors of the Empirical Calibration Method

To interpret the behavior of the standard deviation and dispersion index, in case the empirical calibration method is performed on 48 images of the Las Vegas data set, the calibration factors used in the empirical method are further analyzed. The calibration factors were calculated using (3.26):

$$c_k = \frac{1}{PS} \sum_{ps=1}^{PS} \frac{A_{ps}^k}{\mu_{A_{ps}}}, \quad \text{with} \;\; ps = 1, 2....PS. \tag{4.4}$$

The distribution of the empirical calibration sub-factors $\frac{A_{ps}^k}{\mu_{A_{ps}}}$ are analyzed per image in Figure 4.11, as the empirical calibration method is based on using the mean of these factors of all PSCs per image, resulting in one calibration factor c_k per image. It seems that the distribution of these sub-factors for images with an acquisition date after the beginning of 2001 (blue dotted line) differ from that of the earlier images (red line). The blue circles represent the factors c_k for the four more recent images. These factors are larger than the calibration factors of the earlier images (red stars) that all have values around one. This behavior is probably caused by the influence of the high Doppler centroid frequencies of over 1200 Hz in the more recent images, whereas the Doppler centroid frequencies are normally up to ±400 Hz. In Figure 4.7 the behavior of the mean per image of all amplitude values of the selected PSCs are given. For the last four images a drop up to 5 dB can be seen for the oversampled raw and ESA calibrated data sets, which indicates on erroneous instable amplitude values within these images. The mean amplitude values for the empirical calibrated data set is higher, caused by the higher c_k values for the last images.

The aim of the calibration in this study was to diminish differences between ERS-1 and ERS-2 imagery, but without messing up the statistics of the amplitudes, as these statistics are used to select PSCs. As a consequence, the empirical calibration should only be performed on images with normal f_{DC}. If other images with higher f_{DC} are included in the empirical calibration method, these images disturb the calibration of the calibration factors c_k. To test this, the calibration is performed again using only the first 44 images, of which the results are already described above.

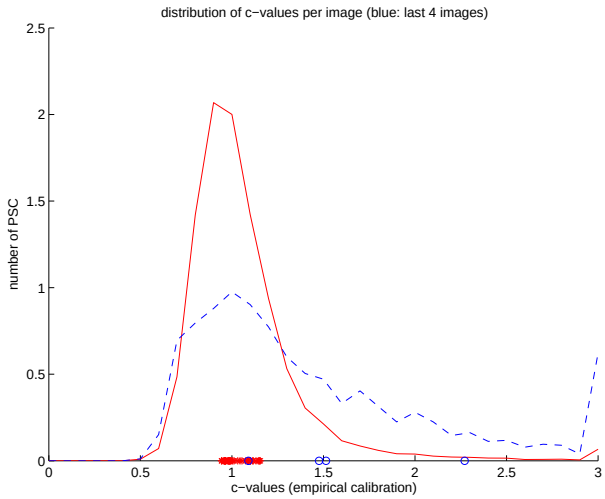

Figure 4.11: Distribution of the empirical sub-calibration factors per image. The red line represents a normalized histogram of the sub-calibration factors $\frac{A_{ps}^k}{\mu_{A_{ps}}}$ of the first 44 images. The blue dotted line represents the last 4 images with large f_{DC}. The red stars and blue circles give the matching calibration factors c_k.

4.4.5 Amplitude Residual Analysis

The amplitude residuals of the selected PSC are analyzed to give a validation of the calibration procedure and to find out whether the calibration disturb the statistics after calibration. The residuals are defined as the difference per PSC between the amplitude and their mean over the image time series. It is expected that the residuals are smaller after calibration, i.e., the scatterers are supposed to be more stable. The vectors of residual amplitudes follow from:

$$A_{ps}^{k,\mathrm{res}} = A_{ps}^k - \mu_{A_{ps}} \tag{4.5}$$

with PSCs $ps = 1, 2, \ldots PS$ and images $k = 1, 2, \ldots K$. This results in three different data sets of residuals for the oversampled raw data, ESA calibrated data and empirically calibrated data. According to simulations and theory, the residuals of the amplitudes of the selected PSC (with $D_A < 0.25$) have a normal Gaussian distribution.

When using only the available data it is hard to test whether the residuals are normally distributed, due to the limited number of samples: there are only 48 residuals per PSC available. Therefore a simulation with more samples is performed to test the distribution of the residuals compared to the distribution of the same number of independent samples from the normal distribution using the Kolmogorov-Smirnov test.

Kolmogorov-Smirnov test

A Kolmogorov-Smirnov test is performed to compare the derived residual amplitude values with a normal distribution, i.e., it represents how good the data fit a normal cumulative distribution. This test can be used to parameterize if the calibration affects the statistics of the selected point scatterers. The Kolmogorov-Smirnov test statistic is the maximum difference between the cumulative distribution of the residuals and the theoretical normal distribution.

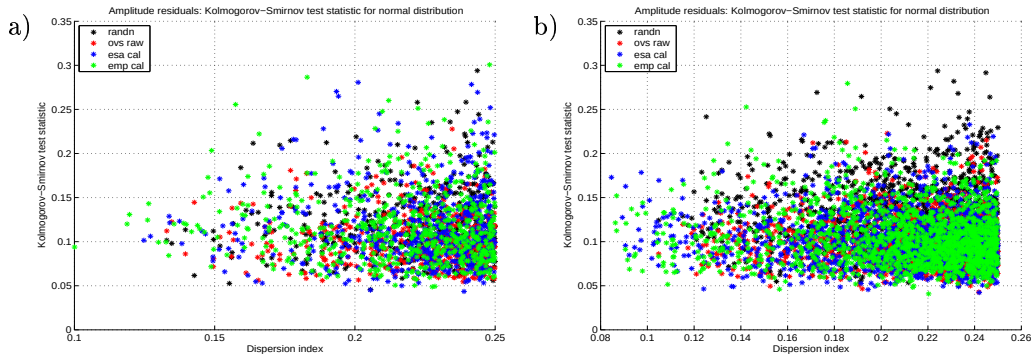

Figure 4.12: Kolmogorov-Smirnov test for the oversampled raw data, ESA calibrated and empirical calibrated data. Also random normally distributed samples are included (black). In a) the results for 48 images are given, and in b) the results for 44 images with low Doppler centroid frequency. Almost all of the residuals are normally distributed. The number of rejected PSCs by the Kolmogorov-Smirnov test are given in Table 4.8.

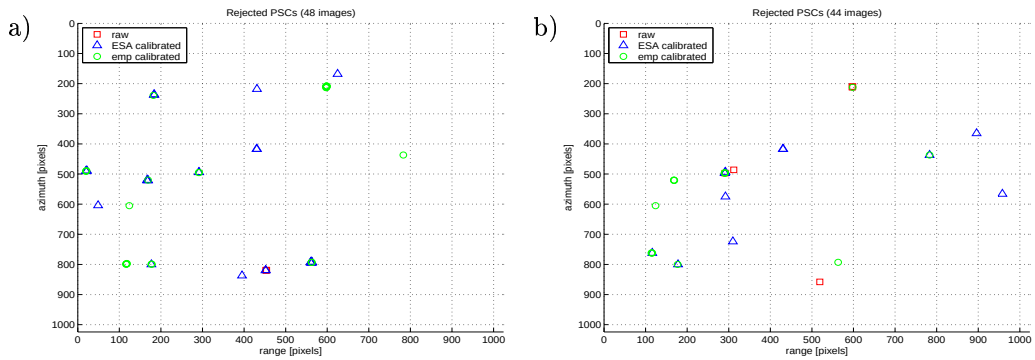

Figure 4.13: Spreading of the rejected PSCs by the Kolmogorov-Smirnov test a) 48 images, b) 44 images. The rejected points are spread over the whole image. The similarity between the rejected PSCs from different data sets is low: only 1 PSC is rejected from all data set for the case 44 images are used. For the data set of 48 images no PSCs are rejected by all data sets.

Based on point scatter theory some simulations, which compare the cumulative distribution with independent samples form the normal distribution, have been carried out that indicate that the residuals are normally distributed for point scatterers with $D_A < 0.25$. But the Kolmogorov-Smirnov test is not perfect: it is limited by the number of samples used and there always remains a test statistic of about 0.1 when a limited number of samples is used. The Kolmogorov-Smirnov test is also performed on the available residuals data sets (the 'raw' oversampled, ESA calibrated and empirical calibrated amplitude residuals) and the same number of independent samples from the normal distribution. The results of this can be seen in Figure 4.12. Most of the residual data sets seem to be normally distributed: the statistics of the amplitude residuals do not change significantly after calibration. From this, it can be concluded that the calibration does not disturb the statistics of the selected point scatterers.

The number of points that are rejected by the Kolmogorov-Smirnov test are given in Table 4.8. Note that after the calibration more PSCs are rejected by the Kolmogorov-Smirnov test than before the data were calibrated, i.e., more PSCs are assumed to be not normally distributed. From Table 4.5 it becomes clear that more points are pointed out to be PSCs after calibration, but they probably have worse statistics, and as a consequence more PSCs are rejected. On the other hand, it might be possible that more 'false detected PSC', i.e., PSCs that have not a coherent phase behavior over time, are rejected after calibration. Furthermore, relative fewer points are rejected if only 44 images are used (see percentage in Table 4.8), whereas a lot more PSCs are selected. This is not surprising, as only the best 44 images are used with the best statistics for PSCs selection.

Number of rejected PSC in:	48 images	44 images
Oversampled 'raw' data	3 (0.67%)	6 (0.47%)
ESA calibrated data	33 (5.68%)	12 (0.78%)
Empirical calibrated data	26 (4.51%)	15 (0.99%)

Table 4.8: Number of selected PSCs that are rejected by the Kolmogorov-Smirnov test, using a significance level of 5%. The percentage of the total number of selected PSCs per data set is given between the brackets.

The spreading of the rejected PSCs is given in Figure 4.13. Different PSCs are rejected from the oversampled and calibrated data set. From further analysis it appears that almost all rejected PSCs are part of larger clusters. Therefore, it is expected that if only the best scatterer per cluster is selected, the number of rejected PSCs will approach zero.

From the comparison results presented in this section it can be concluded that both calibration methods improve the selection of PSCs. The detection rate for both methods is higher after the images are calibrated. However, better conclusions on which calibration provides the best results can be obtained if it is known how many of the selected PSCs have a coherent phase behavior. This false detection rate, the second criteria specified in the beginning of this section, is discussed in Section 4.5. The third criteria, the reduction of computation time of the calibration, is discussed in Section 4.6.

4.5 Results of Permanent Scatterer Analysis

To analyze how many of the selected permanent scatterer candidates, which have a stable amplitude behavior, have also a coherent phase behavior, a processing method for the analysis of permanent scatterers developed by Freek van Leijen is used. He used crops of 30 complex SAR data as input for his processing method. Although this is only a first version for the analysis of permanent scatterers, some interesting results can be obtained from the comparison of the PSCs and PS dataset. The comparison of the number of PSCs that were selected from the amplitude time series are compared with the number of scatterers that show large phase coherence over time, resulting in a false detection rate, which is defined as the percentage of selected PSCs based on amplitude data, that do not show a coherent phase behavior.

For the 30 SAR images interferograms are created of the same crops of the city center of Las Vegas as used before and are used as input for the PS processing. The three different amplitude data sets are used again for the selection of PSCs: the oversampled raw, ESA calibrated, and empirically calibrated data set. The PSCs are selected using the dispersion index $D_A < 0.25$, and the phase values and height to phase factors are stored to use in the permanent scatterer analysis. The output of the PS processing consists, besides an estimation of deformation profiles per PS and DEM errors, of a data set of the coherence per PSC. Evaluation of the coherence per PSC over time in relation to a certain threshold value gives the final group of permanent scatterers. In this comparison the threshold value for the coherence is set on 0.75.

In Table 4.9 the number of permanent scatterer candidates and the final group of permanent scatters are given for 30 images. Again, more PSCs are selected after the images are calibrated. These PSCs, 41 for the raw oversampled data, 57 for the ESA calibrated data and, 19 for the empirical calibrated data, are randomly distributed over the image. Most of the rejected PSCs are part of larger clusters of selected PSCs, thus, there will be other permanent scatterers available on this place in the image to estimate the deformation profile. The percentage of rejected PSCs, i.e., the PSCs that are wrongly identified by the PSCs selection as they do not have a coherent phase behavior, is very low for the empirical calibration method: 0.92%. The percentage for the ESA calibration method is higher: 2.73%, which is even higher than for the oversampled raw data: 2.46%. Although, the percentages for all data sets are low, the empirical calibration method shows the best results in this case.

Number of:	PSCs	PS 30 images
Oversampled 'raw' data	1668	1627 (97.54%)
ESA calibrated data	2086	2029 (97.27%)
Empirically calibrated data	2048	2029 (99.08%)

Table 4.9: Number of selected PSCs that are selected from 30 cropped images. In the second column the number and percentage of pixels that can be marked as permanent scatterer, based on phase coherence, are given, resulting in a false detection rate. It appears that the empirical calibration method shows the best results for the calibration in this study. The false detection rate for this method is the lowest: only 0.92% of the pixels were wrongly marked as PSCs.

Note that the number of permanent scatterers that have a coherent phase behavior, using a threshold value of 0.75, is the same for the ESA calibrated data and the empirically calibrated data. From both data sets 2029 points with stable phase behavior are selected. However, only 1792 points of the 2029 selected permanent scatterers are the same in both data sets.

To enable better analysis of the reliability of the PSCs before and after the different calibration methods are performed, an analysis of the phase behavior of permanent scatterers using more images or crops of other areas, as, e.g., mountainous areas or fields, is needed. Besides, as a first version of a processing method to analyze permanent scatterers is used in this study, further research is needed to provide more insight in the false detection rate using improved versions of this method.

4.6 Approach for a Calibration Method for the Selection of PSCs

In the previous section results were presented of the comparison between the oversampled raw data, the ESA calibration method and the implemented empirical calibration method. Interesting for this study is to evaluate which elements of these calibration methods are of importance to enable a time series analysis of amplitude data of all available images in order to select a set of permanent scatterer candidates. The calibration method should eliminate the differences between amplitude values within the image time series, caused by different sensor characteristics of ERS-1 and ERS-2, or other differences caused by, e.g., different satellite geometry, in such a way that a set of PSCs can be selected based on the statistics of amplitudes within these time series.

First, in Section 4.6.1, the importance of the different ESA calibration factors will be discussed. In Figure 4.4 it was shown that the calibration constant K has the highest influence on reducing the differences between ERS-1 and ERS-2. Therefore, the 48 crops of Las Vegas are calibrated using only this constant correction factor, of which the results are presented in Section 4.6.2. As from the histograms of the test images with large baselines (see Section 4.2) it was found that the histograms of the amplitude data mach better after the inverse of the replica pulse power is applied to the data, some additional tests are performed using this inverse correction factor in the ESA calibration method. These results are presented in Section 4.6.3. Finally, in Section 4.6.4 some recommendations on the calibration for PSCs selection are given. Using these recommendations, a proposal for the implementation of a calibration method of ERS SAR imagery can be given.

4.6.1 Influence of the ESA Calibration Factors on the PSCs Selection

The calibrated amplitude value per pixel is derived using the expression given in Eq. (3.6) on page 19, according to the ESA calibration document (Laur et al., 2002):

$$A^2_{c_{ij}} = A^2_{ij} \frac{\sin(\alpha_i)}{\sin(\alpha_{\text{ref}})} \frac{R_i^3}{R_{\text{ref}}^3} \frac{1}{G(\theta_i)^2} \frac{\text{Image Replica Power}}{\text{Reference Replica Power}} \text{PowerLoss}_{ij}.$$

with on the right hand side the correction factors for varying local incidence angle, range spreading loss, elevation antenna pattern gain, replica pulse power and powerloss.

In the ESA document the calibrated intensity is used to calculate the backscattering coefficient σ^0, which is a measure for the energy reflected back by the Earth's surface, see Eq. (3.5) on page 19:

$$\sigma^0 = \frac{A^2_{c_{ij}}}{K},$$

This backscattering coefficient is very useful for remote sensing applications that, e.g., distinguish between different soil types. However, in this study, the calibration is performed to reduce differences in amplitude data between the images, caused by ,e.g., the use of different sensors (ERS-1 and ERS-2). Therefore, a critical evaluation of all ESA calibration factors is needed.

In Section 4.2.2 and Table 4.2, see page 40, the variation in size of the different calibration factors has already been shown for a test set of four test images with large perpendicular and parallel baselines. For the calibration purpose of this study, only the factors that show large variation between the images are of importance. For example, for the Las Vegas data set, the first three correction factors in Eq. (3.6), which vary with range position, show no large variation between the images and are therefore not important for the selection of PSCs (see Section 4.2.2).

This is explained by the way the PSCs selection is performed. The selection is based on the dispersion index D_A:

$$D_A = \frac{\sigma_A}{\mu_A}, \tag{4.6}$$

with σ_A the standard deviation and μ_A the mean of the amplitudes over the image time series. A resolution cell will have approximately the same correction for local incidence angle, range spreading loss, and elevation antenna pattern gain in every image, as the shift between the images in range direction is maximum 2 km ($\approx$ 100 pixels) for the Las Vegas data set. This results in a maximum difference in correction factor of 0.006 between the images (see Section 4.2.2). Therefore, both the standard deviation and the mean of the amplitudes over time will have approximately the same level of change, and, as a consequence, the dispersion index will not be influenced: the same set of PSCs will be selected as when the range dependent correction factors were not applied. Only if a resolution cell is situated at near range in one image and almost at far range in another image, the differences between these corrections in different images will be larger and their contribution to the calibration cannot be neglected. However, this situation will never occur, as in general the maximum overlap between images within a data stack is only several km.

In Section 4.2.2 it is explained that also the correction for powerloss, that varies in range and azimuth direction, show no large differences between the same areas in different images, and is therefore not important for the calibration in this study. From test results presented in Section 4.2 it becomes clear that the only factors that show large differences per resolution cell over the image time series are the replica pulse power correction and the calibration constant K. These factors are most important to diminish the deviation between ERS-1 and ERS-2 images. As both factors are constant per image they

scale the amplitudes in different images to each other. For calibration constant K this is done by applying Eq. (3.22), see page 27, that scales all images to ERS-2 using the calibration constant K of ERS-2 as reference ($K_{\text{ref}} := K_2$).

$$A_{\text{cal}_{ij}} = \frac{A^2_{c_{ij}}}{K} K_{\text{ref}}.$$

Summarized, if there are no large relative displacements between the images, and, as a consequence, the range and azimuth dependent corrections can be neglected, it is possible to replace the total ESA calibration method by just one scaling factor per image. A small reduction in processing time is achieved by leaving out some of the ESA correction factors. However, as the oversampling step is the far most time consuming step, there seem to be more benefit in improving this step. In the following sections some tests are performed using different implementations of the ESA calibration method. First, a restricted ESA method, using only scaling based on calibration constant K, is evaluated. In Section 4.6.3 the ESA method using the inverse of the correction for replica pulse power is tested, and results on the selection of PSCs are given.

4.6.2 Calibration using ESA Calibration Constant K

From the histograms shown in Figure 4.4 (see page 39) can be seen that the calibration constant K has the most influence on reducing the differences between ERS-1 and ERS-2. To analyze the influence on the selection of PSCs if only this correction would be applied, all 48 crops of Las Vegas are calibrated using only Eq. (3.22) given on page 27, i.e., no corrections are applied to ERS-2 imagery and all ERS-1 images are scaled to ERS-2, using the ratio based on the calibration constants K. As mentioned in Section 3.3.3, K differs for the Las Vegas data set only for ERS-1 and ERS-2, but for other data sets, with, e.g., other acquisition dates, other values for K are possible (see the look up table in Laur et al. (2002)).

After the crops are calibrated a selection of PSCs is performed using the condition $D_A < 0.25$, which results in 601 selected PSCs (30 per km^2). This is more than the PSCs that were selected using the empirical and ESA calibration method (see results presented in Table 4.5, page 47: 576 and 581 PSCs). In other words, the detection rate, one of the criterions specified in Section 4.4, is higher if only calibration constant K is used.

In Figure 4.14 the variation of the mean of the amplitudes per image of all selected PSC are given. The pattern for the restricted calibration method, using only K, is more stable ($\sigma = 0.95$ dB) compared to the results of the ESA calibration method given in Table 4.4 on page 45 ($\sigma = 0.99$ dB). Note however, that the PSCs from the empirically calibrated data set show the most stable results ($\sigma = 0.49$ dB) and is preferred, based on the criterion of amplitude stability, to use for the calibration in this study.

Thus, both the stability and the detection rate of PSCs improve if only calibration constant K is applied to the oversampled data, and the ESA calibration method can be restricted to the use of only this factor for the calibration purpose in this study.

4.6.3 Calibration using the Inverse Replica Pulse Power Correction

From the histogram analysis of four test images in Section 4.2 it appears that the inverse of the replica pulse power correction shifts the amplitude histograms more on top of each other than if the replica pulse power correction is applied, which shifts the histograms away from each other. Therefore, the ESA calibration method is applied again to the 48 crops of Las Vegas, but now using the inverse of the replica pulse power correction, to evaluate the influence on the stability of the amplitude values and the selection of PSCs.

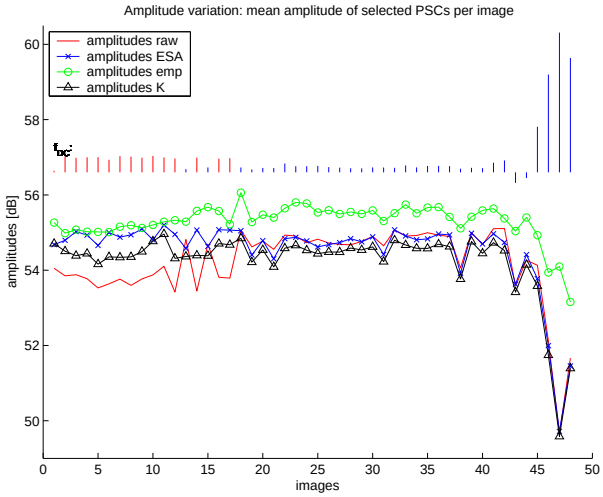

Figure 4.14: Variation of mean amplitudes of all selected PSC per image to visualize the influence of the calibration methods on the differences between ERS-1 and ERS-2 imagery. The lines on top represent the variation in Doppler centroid frequency. The empirical calibration method shows the most stable pattern ($\sigma = 0.49$ dB). The amplitudes of the calibration using only K is higher ($\sigma = 0.95$ dB). Comparing these values with Table 4.4, it becomes clear that the restricted ESA calibration method, using only K, shows better results than if all ESA correction factors are included ($\sigma = 0.95$ dB, vs. $\sigma = 0.99$ dB).

a)

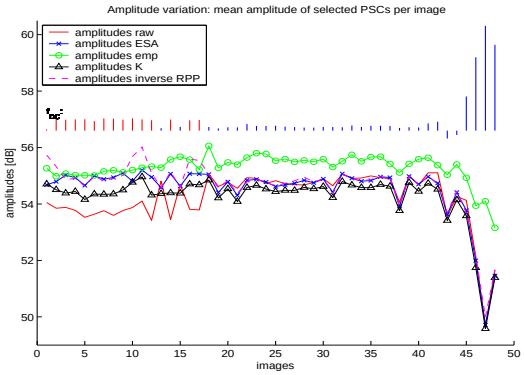

b)

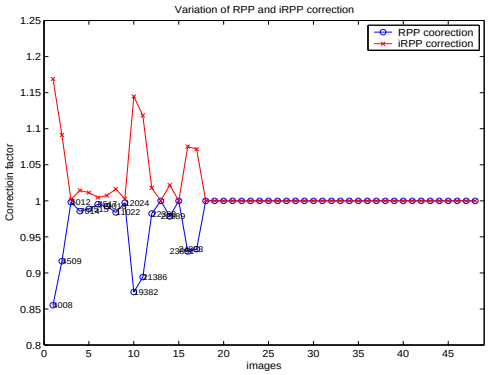

Figure 4.15: a) Variation of mean amplitudes of all selected PSCs per image, the results of the inverse replica pulse power correction are given by the dotted line. The stability of the amplitude time series is lower compared to the results when the 'normal' ESA calibration method is used, cf. from Table 4.4, page 45: $\sigma = 1.01$ dB, vs. $\sigma = 0.99$ dB. From these results appears that the replica pulse power correction should not be replaced by its inverse. b) Variation of the replica pulse power correction (blue) and inverse replica pulse power correction (red) for ERS imagery. The replica pulse power correction is only applied to ERS-1 imagery, as ERS-1 does not have an automatic gain control system. The correction factors of the inverse replica pulse power correction are all positive. The peaks in b) are clearly visible in a), which indicates that the inverse replica pulse power has a negativ effect on the stability of the amplitudes.

The values of the replica pulse power correction and its inverse are shown is Figure 4.15b. The variation of replica pulse power correction is from 0.85 to 1.00 (blue line), and for its inverse from 1.00 to 1.17 (red line). The values for all ERS-2 images are one, as this correction is only applied to ERS-1 imagery, because ERS-1 does not have an automatic gain control system. The influence of these inverse correction factors are clearly visible in Figure 4.15a. The images with large replica pulse power correction introduce peaks in the amplitude time series, resulting in a less stable amplitude (σ = 1.01 dB) compared to the 'normal' ESA calibration method (σ = 0.99 dB).

Also the detection rate of PSCs decreases when the inverse replica pulse power is applied. From the data set calibrated using the ESA calibration method with the inverse replica pulse power correction 516 PSCs were selected. With the 'normal' ESA calibration method 581 PSCs were selected. Therefore, it is recommended to use the replica pulse power correction in the ESA calibration procedure and not its inverse. However, the correction factor for the replica pulse power is still low compared to the correction factor using calibration constant K (up to 1.44), and from the previous section it became clear that the use of only calibration constant K provides the best results for the calibration in this study.

4.6.4 Recommendations on Calibration for PSCs Selection

In this chapter two calibration methods, the ESA calibration method and the empirical method, were analyzed and compared in order to evaluate which method, or elements of a method, is most suitable to use for the calibration of ERS SAR imagery to select PSCs. The calibration purpose in this study is to diminish the differences between the amplitude data of stacked images to enable a time series analysis on amplitude data that are not influenced by different sensor characteristics or satellite geometry.

In general, it depends on the specific ERS SAR data set which of the implemented calibration procedures is the best solution for the calibration in this study. If the overlap between the SAR images in range direction is small, it is sufficient to use a constant factor per image: either the constant factor K from the ESA calibration method, or a constant factor derived from empirical estimation. Note, that if only a few images are available, the use of the constant calibration factor K of the ESA calibration can be preferred, as this method can be applied to every single SAR image. The factor K can be obtained from look-up tables, based on external calibration results. The presented empirical method is based on the estimation of a constant calibration factor from time series of amplitude data, and will be less accurate if only a few images are included. Besides, if images are included that have a high Doppler centroid frequency, the estimation of the constant calibration factors of other images is disturbed. This will influence the dispersion index, which can introduce errors in the PSCs selection.

Based on the criterion presented in Section 4.4, the stability of amplitudes after calibration, detection rate of PSCs, false detection rate of PSCs, and the computation time, the empirical method is the best method to use for the calibration purpose in this study. This method shows the best amplitude stability (0.49 dB vs. 0.99 dB), and false detection rate (0.92% vs. 2.73%) for the selected PSCs. Although the detection rate is slightly better for the ESA calibration method (67.3% vs. 66.7%), the empirical method is preferred, as the false detection rate is much better for this method. Regarding the computation time, it is obvious that the ESA calibration method will be faster than the empirical method when only a constant correction factor will be applied to the image. For the ESA calibration method this constant factor can be taken from look-up tables and multiplied with the amplitude data, whereas for the empirical calibration method a calibration factor is calculated from the amplitude data, which will take more time. However, the oversampling of the complex SAR data, that has to be applied before calibration can be performed, takes much more computation time than the calibration.

Summarized, assuming the availability of enough images with low Doppler centroid frequency, the empirical calibration method is the best method to use. In other cases, the restricted ESA calibration method, using only calibration constant K, would be the best solution.

Chapter 5

Conclusions and Recommendations

5.1 Introduction

This study emphasizes on the amplitude calibration of ERS SAR imagery in order perform a reliable selection of permanent scatterer candidates (PSCs) for deformation monitoring. Calibration is required to diminish differences between the amplitude values of SAR imagery caused by different sensor characteristics or image geometry. After the images are calibrated, the points with the most stable amplitudes are selected and marked as PSCs, using a time series analysis and statistics of the amplitudes on pixel base. In Chapter 3 and 4 two calibration methods to calibrate ERS SAR imagery are presented and compared. The results from this comparison are used to answer the main question of this study on how the calibration of ERS SAR Imagery should be implemented in order to perform a selection of reliable permanent scatterer candidates. In this study a test data set is used of SLC SAR images of Las Vegas. Crops of approximately 2×10 km of 48 SAR images are used to test the implemented calibration methods and compare these methods.

The conclusions of this study, presented in Section 5.2, are split up into two parts. First, some conclusions on the implementation of the used ERS SAR ESA calibration method and empirical calibration method will be given, and, second, conclusions will be drawn from the comparison of these implemented calibration methods. Based on three different criteria, this leads to an approach on how the calibration can be best implemented in order to calibrate ERS SAR images for the purpose of this study. Recommendations on further research are listed in Section 5.3.

5.2 Conclusions

Implementation of the used ERS SAR calibration methods

The calibration methods that are implemented in this study are the ESA calibration method and an empirical calibration method. The amplitude calibration is an important preprocessing step that has to be performed before a selection of PSCs can be made. The place of the amplitude calibration within the sequence of all preprocessing steps is shown in Figure 5.1. The calibration and coregistration are performed on different times for the ESA calibration method and the empirical calibration method.

Point wise conclusions will be given on the implementation of the ESA calibration method and the empirical calibration method.

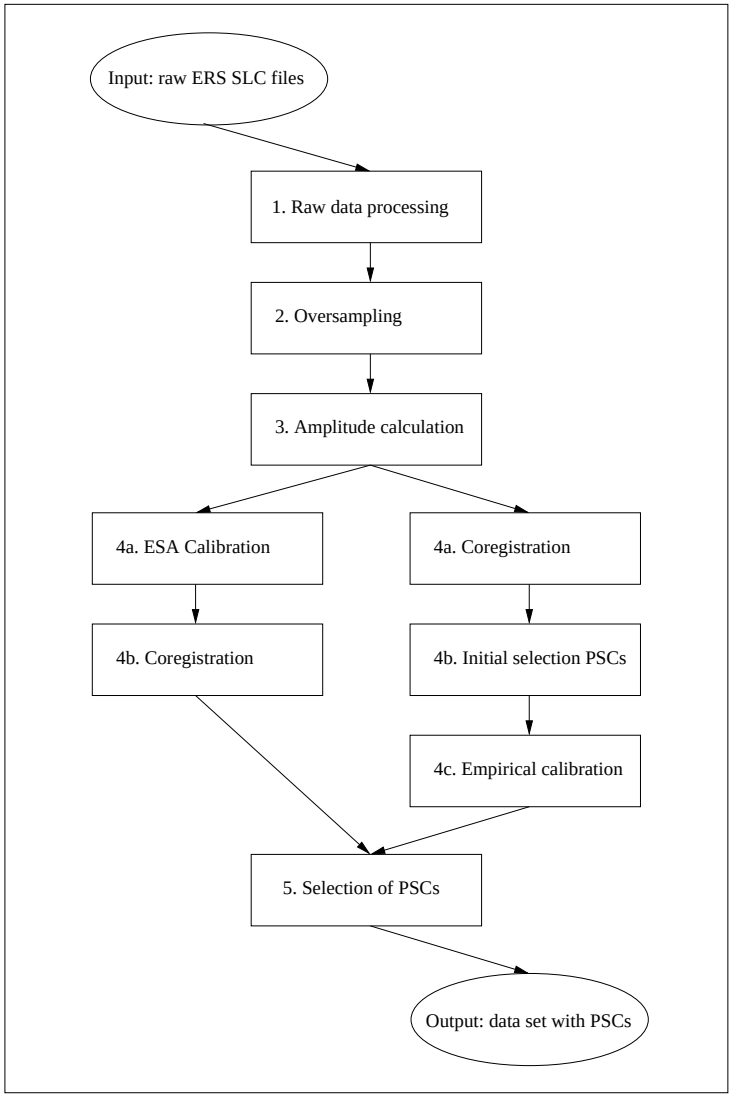

Figure 5.1: Preprocessing steps that have to be performed before a selection of PSCs can be made. 1) Processing of the raw ERS SLC SAR data to complex SAR images. 2) The SAR data need to be oversampled by factor two to avoid aliasing effects. 3) Amplitude values are calculated from the complex data to be used as input for the calibration. 4) Amplitude calibration and coregistration. The sequence of these steps is different for the ESA calibration method and the empirical calibration method. The ESA method contains range and azimuth dependent correction factors that are based on the original geometry. Therefore, the images are coregistered after the ESA calibration is performed. In the empirical method a calibration factor per image is calculated from the variation of amplitude data over time on pixel base, and thus, the data need to be coregistered before the calibration is performed. 5) PSCs are selected using a time series analysis of amplitudes on pixel base. Only the scatterers with the most stable amplitude are selected and marked as PSCs, using a threshold value of 0.25 on the dispersion index, which is the ratio between the standard deviation and the mean of the amplitudes per pixel over time.

ESA calibration method

The ESA calibration method contains different correction factors that have to be applied to the amplitude data. The correction factors for local incidence angle, range spreading loss and antenna pattern gain vary with range direction. The corrections for powerloss vary in range and azimuth direction, and the correction for replica pulse power and calibration constant K are constant per image. Most of the ESA correction factors can be obtained from look-up tables derived from external calibration campaigns.

- The ESA calibration method can be applied to every single SAR image. As this method is mainly based on physical properties of the sensors and satellite geometry and not on the amplitude data itself, this method has the advantage that it can be applied independent of data of other SAR images.
- The correction factors of the ESA calibration method that vary with range direction are not important for the calibration in this study. The calibration should diminish the differences between amplitude values over the image time series. As the overlap between the images is maximum 2 km ($\approx$ 100 pixels), the variation in correction factor between different images can be neglected. The overlap results in a variation of 0.006 for the incidence angel correction and 0.003 for the correction factor for range spreading loss between images. This is very low compared to the variation for the correction factors for replica pulse power up to 0.14 (vary from 1 to 1.14 between the images) or the influence of calibration constant K (1 to 1.44). Therefore, the ESA calibration method can be restricted to the use of only the constant correction factors per image: the correction for replica pulse power and calibration constant K.
- From histogram analysis of four images it appears that the inverse of the replica pulse power correction shift the amplitude histograms more on top of each other than if the replica pulse power is applied, which shift the histograms away from each other. However, if the replica pulse power correction is replaced by its inverse, the stability of the amplitude data becomes worse. The standard deviation of all selected PSCs over the image time series increase from 0.99 dB to 1.01 dB. Also the number of PSCs that will be selected decrease from 581 to 516 when the inverse correction is applied. Therefore, it is recommended to use the replica pulse power correction in the ESA calibration procedure and not its inverse.
- The calibration constant K has the most influence on reducing the differences in amplitude between ERS-1 and ERS-2 imagery. If only this correction factor is applied to the data and all other ESA correction factors are omitted, the stability of the amplitude over the image time series of the PSCs improves with respect to the situation when all corrections were applied: the standard deviation decreases from 0.99 dB to 0.94 dB. Also more PSCs are selected: 601 instead of 581. Besides, leaving out some of the ESA correction factors will reduce the computation time.

From this can be concluded that the best way to implement the ESA calibration method for the calibration purpose in this study is the use of only calibration constant K. Using only this factor, the method provides almost the same results as if all correction factors are applied, but is much faster.

Empirical calibration method

The empirical method estimates one constant calibration factor c_k per image from the amplitude data of an initial selection of points that a show stable amplitude behavior and are Gaussian distributed. These points can be selected using the dispersion index, which is the ratio between the standard deviation and the mean of the amplitudes over the image time series, and select all points that have a dispersion index below 0.25. The c_k values are calculated by taking the mean of the ratio between the amplitude values of all stable points and their mean over the image time series. This factor c_k per image is used to scale all amplitude values within this image. After the calibration a new set of PSCs is selected using again the threshold value of 0.25 on the dispersion index derived from the calibrated data.

- Only images that have a low Doppler centroid frequency f_{DC} should be included in the computation of the calibration factors c_k, as images with high Doppler centroid frequencies will disturb the computation of the calibration factors c_k. A drop of almost 5 dB is visible for the amplitude values of the PSCs from the images that have high f_{DC} (see Figure 4.7, page 46). As in the computation of the c_k factors per image the amplitude values over the image time series are used, these lower amplitude values in the images with high f_{DC} influence the values of the c_k factors of all images. All calibration factors normally have values around 1, whereas the calibration factor for images with high Doppler centroid frequency are up to 2.3. That the use of images with high f_{DC} should not be used in the computation, is also shown in the histograms of the standard deviation and the dispersion index that deviates from the pattern of the ESA and raw data (Figure 4.10, page 50). When only the images with a f_{DC} lower than 400 Hz are used, the standard deviation and dispersion index show a normal pattern.
- Unlike the ESA calibration method, the empirical calibration cannot be performed on one single image. The calibration factors c_k are calculated from time series of amplitude data. A minimum number of images is needed to ensure the reliability of the c_k calculation and the final selection of PSCs.

Remarks on the conclusions:
To test the implemented calibration methods, crops of a data set of 48 SLC SAR images of Las Vegas are used. The conclusions presented in this section are based on these crops, but the conclusions also hold for crops of other parts of the SAR images. As the correction factors c_k for the empirical method and the most important correction factors for the ESA calibration method, the calibration constant K, are constant per image, it does not matter what crop is chosen. Crops of other parts of the SAR images will give the same results.

Comparison of the implemented calibration methods

A comparison is performed on a data set of all 48 available crops that are calibrated using the ESA and empirical calibration method. Also a data set of 44 crops, of only the images that have a Doppler centroid frequency below 400 Hz, is compared. Results of this comparison were presented in Chapter 4. Here, three criterion were specified which can be used to decide which calibration method, or elements of this calibration methods, are most suitable for the calibration in this study. The criteria are further specified in Section 4.4. Based on these criteria it appears that the empirical calibration method gives the best results for the calibration purpose in this study. The criteria are:

1. *Detection rate of PSCs.*
   The detection rate is specified as the number of PSCs that are selected using a specific calibration method as a percentage from the total number of different PSCs selected from all data sets (oversampled raw, ESA and empirically calibrated). The number of selected PSCs after calibration should be as high as possible. Also the stability of amplitudes needs to be as high as possible after calibration, as the selection of PSCs is based on pixels with low dispersion index (ratio between the standard deviation and mean of the amplitudes over the image time series).
2. *False detection rate of PSCs.*
   The false detection rate is defined as the percentage of selected PSCs based on amplitude data using the dispersion index, that do not show a coherent phase behavior. Points with coherent phase behavior are needed in the permanent scatterer analysis to estimate, e.g., deformation profiles per permanent scatterer. The calibration method with the lowest false detection rate is preferred. If the false detection rate is low, more PSCs with a coherent phase behavior are selected that can be used in the permanent scatterer analysis, i.e., the selected PSCs are more reliable.
3. *Computation time.*
   The computation time of the calibration processing should be as low as possible.

Per criterion conclusions are drawn on which calibration method can be preferred.

Ad 1) Detection rate of PSCs.

- The detection rate is highest for the ESA calibration method: 67.3% of all different PSCs that are selected from all data sets are selected by the ESA calibration method. For the empirical calibration method this is 66.7%. The results for 44 images are 85.1% vs. 81.3%. Although the ESA calibration method shows the best results, the results form the empirical results are almost as good as from the ESA method. Both calibration methods improve the detection rate of PSCs. The ESA method detects 30.3% and 25.2% (48 and 44 images) more PSCs than before the images were calibrated, and the empirical calibration method detects 29.1% and 19.7% more PSCs, which indicates that calibration of ERS SAR imagery is crucial for the selection of PSCs.

  The empirical calibration method provides the most stable amplitude values over the image time series. The standard deviation of the mean of all PSCs over time is 0.49 dB when 48 images are used (cf. 0.99 dB for the ESA calibration method and 1.00 dB for the uncalibrated oversampled data). The results for the data set of 44 images are even better: 0.19 dB against 0.36 dB for the ESA method, and 0.62 dB for the uncalibrated oversampled data. However, the physical meaning of the ESA calibration should not be neglected. The corrections of the ESA method have a physical interpretation and are not just a scaling of the data.

Ad 2) False detection rate of PSCs.

- The empirical calibration method shows the lowest false detection rate. Tests are performed by selecting points with stable amplitudes (points with a dispersion index below a threshold value of 0.25) and points that have coherent phase behavior (points with a coherence above the threshold of 0.75). Only 0.92% of the pixels that were marked as PSCs after the empirical calibration method did not show a coherent phase behavior. The false detection rate for the ESA calibration method is higher: 2.73%. The selection based on the empirically calibrated data results in more reliable PSCs (points that show also stable phase behavior).

Ad 3) Computation time.

- As the ESA calibration method and the empirical calibration method are calculated on computers with different computational memory, it is impossible to compare the computation time of both methods. However, it is obvious that the ESA method, using only the constant calibration factors from look-up tables, is faster than the empirical method that calculates the calibration factor per image from the amplitude data. The far most time consuming step is the oversampling of the complex radar data, a preprocessing step that needs to be performed before calibration can be applied.

Assumed that there are enough images available that have low Doppler centroid frequencies, the empirical calibration method is the best method to use for the calibration for the selection of PSCs. However, if this is not the case, the restricted ESA method should be used that contains only the constant calibration factor K.

5.3 Recommendations

In this section some recommendations on further research are given:

1. *Use other crops and data sets to test the implemented calibration methods.*

   The test results presented in this research are based on the analysis of a crop of 48 images. In order to test the influence of the different calibration methods on the selection of PSCs, or to decide which (parts) of the implemented calibration methods in this study are most suitable for calibration, more tests have to be performed. Different SAR data sets can be used for this, or crops from other areas of the Las Vegas data set, as, e.g., agricultural fields, desert or mountainous areas.

2. *Improvement of the empirical calibration method*

   In Appendix B a approach to improve the empirical calibration method is given. This approach is based on all amplitude data of all images. This method should be implemented, tested and compared to the results presented in this study, to see whether this method is more suitable for the calibration than the methods implemented in this study. Introduction of a w-test on the data and performing statistical analysis can give more insight on the quality of this calibration method.

3. *Analyze the implementation of the inverse replica pulse power correction*

   One of the correction factors of the ESA calibration method is the replica pulse power correction. According to ESA this correction should be applied by multiplying the amplitude data with the ratio between the image replica power and the reference replica power. However, tests on four images of the Las Vegas data set indicate that the differences between images reduce when the inverse of this ratio is used. However, test on crops of 48 images show that the stability of amplitudes gets worse after the inverse replica pulse power correction is applied. As the aim of the calibration in this study is to reduce difference between the images, this (inverse) correction should be further analyzed.

4. *Perform an analysis on the phase behavior of the selected PSCs using an improved permanent scatterer analysis procedure.*

   The phase of the PSCs that are selected based on amplitude statistics are used in the subsequent permanent scatterer processing to estimate deformation profiles. The set of PSCs that show large phase coherence over time can be compared to the initial sets of selected PSCs after different calibration methods were performed, to evaluate which calibration method give the best results (false detection rate). Results from a first version of PS processing are presented in this study, but further analysis in needed on other data sets, using improved versions of this PS processing.

5. *Analyze the clusters of selected PSCs.*

   Most scatterers that are marked as PSC are part of a larger cluster, containing more PSCs. It is possible that only one or a few dominant scatterers are present and that the neighboring pixels that are also marked as PSCs are side-lobes of these scatterers. For the PS processing only the dominant scatterers within in this cluster are required. By estimating, e.g., one or more sinc-patterns based on the amplitude values through the clusters of PSCs the dominant scatterers can be detected.

6. *Reduce the computation time of the oversampling step.*

   The far most time consuming preprocessing step to perform a selection of PSCs is the oversampling of the SAR data. Improvement of this step would mean an important reduction of the total computation time of the calibration method, and makes it easier to test other data sets.

Bibliography

Amelung, F., Galloway, D. L., Bell, J. W., Zebker, H. A., and Laczniak, R. J. (1999). Sensing the ups and downs of Las Vegas: InSAR reveals structural control of land subsidence and aquifer-system deformation. *Geology*, 27(6):483–486.

Colesanti, C., Ferretti, A., Novali, F., Prati, C., and Rocca, F. (2003). SAR monitoring of progressive and seasonal ground deformation using the Permanent Scatterers Technique. *IEEE Transactions on Geoscience and Remote Sensing*, 41(7):1685–1701.

Cordey, R. (2004). Personal communication.

Ferretti, A., Prati, C., and Rocca, F. (2000). Analysis of permanent scatterers in SAR interferometry. In *International Geoscience and Remote Sensing Symposium, Honolulu, Hawaii, 24–28 July 2000*, pages 761–763.

Ferretti, A., Prati, C., and Rocca, F. (2001). Permanent scatterers in SAR interferometry. *IEEE Transactions on Geoscience and Remote Sensing*, 39(1):8–20.

Hanssen, R. F. (2001). *Radar Interferometry: Data Interpretation and Error Analysis.* Kluwer Academic Publishers, Dordrecht.

Hanssen, R. F. (2003). Subsidence monitoring using contiguous and PS-InSAR: Quality assessment based on precision and reliability. In 11th *FIG International Symposium on Deformation Measurements, Santorini, Greece, 23–28 May, 2003*, pages cdrom, p.8.

Hanssen, R. F. and Klees, R. (1998). Applications of SAR interferometry in terrestrial and atmospheric mapping. In Ligthart, L. P., editor, *Workshop proceedings European Microwave Conference, Amsterdam, 9 October*, pages 43–50. European Microwave Conference, Miller Freeman.

Haykin, S. and van Veen, B. (1999). *Signals and Systems.* John Willey and Sons Inc., New York, USA.

Hoffmann, J. (2003). *The application of satellite radar interferometry to the study of land subsidence over developped aquifer systems.* PhD thesis, Stanford University.

Kampes, B. (1999). *Delft Object-Oriented Radar Interferometric Software: Users manual and Technical Documentation.* Delft University of Technology, Delft, 1.2 edition.

Laur, H., Bally, P., Meadows, P., Sanchez, J., Schaettler, B., Lopinto, E., and Esteban, D. (2002). Derivation of the backscattering coefficient σ^0 in ESA ERS SAR PRI products. Technical Report ES-TN-RS-PM-HL09, ESA. Issue 2, Rev. 5d.

Lyons, S. and Sandwell, D. (2003). Fault creep along the southern San Andreas from InSAR, permanent scatterers, and stacking. *Journal of Geophysical Research*, 108(B1):2047, doi:10.1029/ 2002JB001831.

Meadows, P. J. (1994). The calibration of the ERS-1 synthetic aperture radar using UK-PAF imagery. In *Radar calibration, Proceedings of the 14th EARSeL Workshop, Goteborg, Sweden, 6–8 June 1994*, pages 423–430.

Meadows, P. J., Laur, H., Rosisch, B., and Schättler, B. (2001). The ERS-1 SAR performance: A final update. In *CEOS SAR Workshop, Tokyo, Japan, 2–5 April 2001*, page 8.

Meadows, P. J., Laur, H., and Schättler, B. (1998). The calibration of ERS SAR imagery for land applications. In *Procedings of the 2nd International Workshop on Retrieval of Bio- & Geo-physical Parameters from SAR Data for Land Applications, ESTEC, Noordwijk, The Netherlands, 21–23 October 1998*, pages 35–42.

Meadows, P. J. and Rosich, B. (2003). The ERS-2 SAR performance: Another further update. In *CEOS Working Group on Calibration and Validation SAR Workshop, BNSC/DTI Conference Centre, London, United Kingdom, 24- 26 September 2002.*

Meadows, P. J. and Rosisch, B. (2003). The ERS-2 SAR performance: The 2003 update. In *CEOS SAR Workshop, Montréal, Canada, 25–27 June 2003.*

Papoulis, A. (1968). *Systems and Tronsforms with Applications in Optics.* McGraw-Hill series in Systems Science. McGraw-Hill, New York.

Skolnik, M. I. (1962). *Introduction to Radar Systems.* McGraw-Hill Kogakusha, Ltd., Tokyo.

Teunissen, P. J. G. (2000a). *Adjustment theory; an introduction.* Delft University Press, Delft, 1 edition.

Teunissen, P. J. G. (2000b). *Testing theory; an introduction.* Delft University Press, Delft, 1 edition.

Websites

web1 http://www.multimap.com

web2 http://envisat.esa.int/services/pg/pgerssarslc.xml?full.xsl

web3 http://earth.esa.int/services/best/

Appendix A

Least-squares Estimation using a non-linear Model

In this appendix the procedure for performing a least-squares adjustment is presented for a nonlinear model of observation equations. More information can be found in (Teunissen, 2000a). The vector of observations $E\{\underline{y}\}$ is nonlinearly related to the vector of unknown parameters x:

$$E\{\underline{y}\} = A(x) \ ; \quad D\{\underline{y}\} = Q_y \tag{A.1}$$

To obtain a solution for the unknown parameters, the model is linearized using by making use of Taylor's theorem:

$$E\{\underline{y}\} = A(x^0) + \partial_x A(x^0)\Delta x \ ; \quad D\{\underline{y}\} = Q_y \tag{A.2}$$

The second order remainder is neglected, as this term becomes very small by choosing x^0 close enough to x. With $\Delta\underline{y} = \underline{y} - A(x^0)$ and $\Delta x = x - x^0$ the linearized model reeds:

$$E\{\Delta\underline{y}\} = \partial_x A(x^0)\Delta x \ ; \quad D\{\Delta\underline{y}\} = Q_y \tag{A.3}$$

From this linearized model the least-squares estimator $\underline{\hat{x}}$ can be estimated. The solution of model (A.3) is:

$$\begin{aligned}
\underline{\hat{x}} &= x^0 + \left[\partial_x A(x^0)^* Q_y^{-1} \partial_x A(x^0)\right]^{-1} \left[\partial_x A(x^0)^* Q_y^{-1} \Delta\underline{y}\right] \\
\underline{\hat{y}} &= A(\underline{\hat{x}}) \\
\underline{\hat{e}} &= \underline{y} - \underline{\hat{y}}
\end{aligned} \tag{A.4}$$

with in $\underline{\hat{x}}$ the estimated unknown parameters, $\underline{\hat{y}}$ the corrected observations, and $\underline{\hat{e}}$the least-squares residuals.

The propagation law of variances gives:

$$
\begin{aligned}
Q_{\hat{x}} &= \left(\partial_x A(x^0)^* Q_y^{-1} \partial_x A(x^0)\right)^{-1} \\
Q_{\hat{y}} &= \partial_x A(x^0) Q_{\hat{x}} \partial_x A(x^0)^* \\
Q_{\hat{e}} &= Q_y - Q_{\hat{y}}
\end{aligned} \tag{A.5}
$$

Principle of least-squares iteration

The solutions given in (A.4) hold if x^0 is a good approximation, and the second-order remainder can be neglected. If the approximation is not that good, $\underline{\hat{x}}$ is not the least-squares estimator and an unpredictable error is made. Therefore, the approximation of x^0 is improved by solving (A.4) in a iterative way, starting with $x^i = x^0$:

$$
\begin{aligned}
\Delta \underline{y} &= y - A(x^i) \\
Q_x &= \left(\partial_x A(x^i)^* Q_y^{-1} \partial_x A(x^i)\right)^{-1} \\
x^{i+1} &= x^i + Q_x \partial_x A(x^i)^* Q_y^{-1} \Delta \underline{y}
\end{aligned} \tag{A.6}
$$

The least-squares estimates of the unknowns, when x^{i+1} converges to the final leas-squares estimate, is given by:

$$
\begin{aligned}
\hat{x} &:= x^{i+1} \\
Q_{\hat{x}} &= Q_x
\end{aligned} \tag{A.7}
$$

Appendix B

Approach for an Improved Empirical Calibration Method

In this appendix an approach for an improved empirical calibration method is given. To enable a critical analysis on the quality of the empirical calibration method, the model given in Eq. (3.27) on page 30 should be improved. Using this approach it is not needed to separate the empirical calibration method into two parts: the initial selection of PSCs, and the estimation of the calibration constant c_k per image, as all observations will be included in the estimation of the c_k factors.

In this approach all amplitude values will be scaled to an unknown reference image, denoted as A_p^{ref}, using a scaling factor c_k per image k:

$$E\{\underline{A}_p^k\} = c_k \; A_p^{\mathrm{ref}}, \tag{B.1}$$

with $\underline{A}_p^k$ the observations $m = p \cdot k$, and c_k and A_p^{ref} the unknowns $n = k + p$. The number of images is denoted by $k = 1, 2, \ldots, K$, and the pixels per image by $p = 1, 2, \ldots, P$.

As this is model is nonlinear, it needs to be linearized before the unknowns can be estimated using Taylor's theorem (see Teunissen (2000a)). The linearized observation reeds

$$\Delta\underline{A}_p^k = \Delta A_p^{\mathrm{ref}^0} c_k + c_k^0 \Delta A_p^{\mathrm{ref}}. \tag{B.2}$$

Use for the first approximations $c_k^0 = 1$, and for the approximations of A_p^{ref} the amplitude values of the first image: $A_p^{\mathrm{ref}^0} = \underline{A}_p^1$. With

$$\begin{aligned} \Delta\underline{A}_p^k &= \underline{A}_p^k - c_k^0 A_p^{\mathrm{ref}^0} \\ \Delta c_k &= c_k - c_k^0 \\ \Delta A_p^{\mathrm{ref}} &= A_p^{\mathrm{ref}} - A_p^{\mathrm{ref}^0}, \end{aligned}$$

follows for the linearized model:

$$
E\left\{\begin{pmatrix} \Delta\underline{A}_1^1 \\ \Delta\underline{A}_2^1 \\ \vdots \\ \Delta\underline{A}_P^1 \\ \cdots\cdots \\ \Delta\underline{A}_1^2 \\ \Delta\underline{A}_2^2 \\ \vdots \\ \Delta\underline{A}_P^2 \\ \cdots \\ \vdots \\ \cdots \\ \Delta\underline{A}_1^K \\ \Delta\underline{A}_2^K \\ \vdots \\ \Delta\underline{A}_P^K \end{pmatrix}\right\} = \begin{pmatrix}
A_1^{\mathrm{ref}^0} & 0 & \dots & 0 & c_1^0 & 0 & \dots & 0 \\
A_1^{\mathrm{ref}^0} & 0 & \dots & 0 & 0 & c_1^0 & \dots & 0 \\
\vdots & \vdots & \ddots & \vdots & \vdots & \vdots & \ddots & \vdots \\
A_1^{\mathrm{ref}^0} & 0 & \dots & 0 & 0 & 0 & \dots & c_1^0 \\
\cdots & \cdots & \cdots & \cdots & \cdots & \cdots & \cdots & \cdots \\
0 & A_1^{\mathrm{ref}^0} & \dots & 0 & c_2^0 & 0 & \dots & 0 \\
0 & A_1^{\mathrm{ref}^0} & \dots & 0 & 0 & c_2^0 & \dots & 0 \\
\vdots & \vdots & \ddots & \vdots & \vdots & \vdots & \ddots & \vdots \\
0 & A_1^{\mathrm{ref}^0} & \dots & 0 & 0 & 0 & \dots & c_2^0 \\
\cdots & \cdots & \cdots & \cdots & \cdots & \cdots & \cdots & \cdots \\
\vdots & \vdots & \ddots & \vdots & \vdots & \vdots & \ddots & \vdots \\
\cdots & \cdots & \cdots & \cdots & \cdots & \cdots & \cdots & \cdots \\
0 & 0 & \dots & A_1^{\mathrm{ref}^0} & c_K^0 & 0 & \dots & 0 \\
0 & 0 & \dots & A_1^{\mathrm{ref}^0} & 0 & c_K^0 & \dots & 0 \\
\vdots & \vdots & \ddots & \vdots & \vdots & \vdots & \ddots & \vdots \\
0 & 0 & \dots & A_1^{\mathrm{ref}^0} & 0 & 0 & \dots & c_K^0
\end{pmatrix}
\begin{pmatrix} \Delta c_1 \\ \Delta c_2 \\ \vdots \\ \Delta c_K \\ \dots \\ \Delta A_1^{\mathrm{ref}} \\ \Delta A_2^{\mathrm{ref}} \\ \vdots \\ \Delta A_P^{\mathrm{ref}} \end{pmatrix}, \tag{B.3}
$$

$$
\text{with} \quad Q_y = \sigma_{A_p^k} I_m
$$

It is assumed that the amplitude observations are uncorrelated. Each amplitude observation has a different standard deviation that can be estimated using the signal-to-clutter ratio. The value of the standard deviation per amplitude value depends on the physical properties of the point scatterer and its surroundings.

The least-squares estimates of the unknowns in model (B.3) are estimated using the principle of least-squares iteration (see Teunissen (2000a) and Appendix A). Using the notation $E(\Delta\underline{y}) = \partial_x A(x^0)\Delta x$ for model (B.3), the solution reeds

$$
\begin{aligned}
\Delta\underline{y} &= y - A(x^i) \\
Q_x &= \left(\partial_x A(x^i)^* Q_y^{-1} \partial_x A(x^i)\right)^{-1} \\
\hat{x} := x^{i+1} &= x^i + Q_x \partial_x A(x^i)^* Q_y^{-1} \Delta\underline{y},
\end{aligned} \tag{B.4}
$$

when the solutions iterates to the actual least-squares estimate after i iterations,.

However, model (B.3) is rankdefect. The rankdefect is 1, which can be solved by keeping the scale factor c_k for one image constant, i.e., $c_k = 1$ (set the last column of the A-matrix to zero). This way, the matrix becomes singular and converges to a solution.

This improved empirical calibration method should be implemented and tested in further research to enable a critical evaluation on the quality of this model, by performing, e.g., an analysis of the standard deviation of estimated calibration factors (by applying propagation laws to the data) or a residual analysis.

Appendix C

Implemented Matlab scripts for the ESA calibration method

In this appendix a schematic overview of the scripts for the ESA calibration procedure written in Matlab are given. The ESA calibration procedure consists of several steps of which an overview is given in Figure 5.1. Subsequently, the procedure to calibrate ERS SAR imagery includes steps to read, oversample, detect, calibrate, coregister, and write the SAR data.

The main script '`calibration_total.m`' runs all of the preprocessing steps for the ESA calibration method. Table C.1 gives an overview of all input parameters that needs to be specified in the header of this script.

Input parameters	**Description**
listfile_b	Path and filename of inputfile with orbitnumbers, ERS-mission, and f_{DC}
dir_raw	Path of directory for output raw data processing
dir_unix_run	Path of directory for inputfiles for the DORIS and cpxfiddle run
dir_patches	Path of directory to which the data patches are written after the cpxfiddle run
dir_os	Path of directory to which the oversampled data patches are written
dir_cal	Path of directory to which the calibrated data (patches) are written
dir_unix_cal	Path of directory to which the new .res are written
dir_log	Path of directory to which the log-files of the DORIS run are written
dir_doris	Path of directory in which DORIS will be run
master image	The orbit number of the master image
crop	Size of the crop of the total SAR images (beginline, endline, beginpixel, endpixel)
patch_length	Size of the patches used in the processing (default set on 1024)
ovs	Oversampling factor (default set on 2)

Table C.1: Overview of the input parameters that need to be specified to run the ESA calibration procedure.

The main script consists of eight steps with matching functions. A brief overview of all functions and sub-functions will be given in the remainder of this appendix.

1. **Raw data processing.**

   The available raw SLC SAR images are processed with DORIS using '`create_inputfiles.m`'. This file creates inputfiles per image for the DORIS run and runs DORIS to create complex '`.raw`' files for a cropped image.

2. **Create patches of limited size.**

   The '`.raw`' files are split up into smaller patches to enable further processing in Matlab. Due to the limited computational memory of Matlab the input data have to be of limited size. The script '`cxfiddle_inputfiles.m`' creates inputfiles per image for using cpxfiddle. Cpxfiddle is run to create patches of 'normal' type. This output option of cpxfiddle creates files with real and imaginary data columns.

3. **Oversampling of the images.**

   The images are oversampled using the function '`B_lasvegas_patches_ovs_main.m`'. The oversampling factor is this study is set on 2, but can be specified in the header of the main file. The output of this step is a number of oversampled patches of amplitude data. Also the phase is saved to be able to create the data format that is needed to read the data into DORIS again in a later stage. The sub-function '`B_lasvegas_patches_ovs.m`' is used in this script.

4. **Calculate ESA calibration vector per image.**

   The function '`ESA_calibration_totalvector_RPP.m`' is the first calibration function. It calculates a vector per image from the constant and range dependent calibration correction factors of the ESA method. The sub-function '`B_readkeystring.m`', '`date_calibration_parameters.m`', '`Calibration_ini.m`', '`Calibration_G.m`', and '`Calibration_K.m`' are used in this script.

5. **Calculate power loss correction**

   The function '`Powerloss_esa1504.m`' calculates the correction for power loss per pixel position. As this correction factors varies with range and azimuth position, the output is a matrix containing correction factors per pixel position.

6. **Calibrate the oversampled amplitude data per patch.**

   In the function '`ESA_calibration_patches_RPP.m`', the vector and matrix with calibration correction factors, calculated in the previous calibration functions, are applied to the oversampled amplitude data patches. This results in calibrated oversampled data patches.

7. **Create DORIS '`.raw`' files**

   The oversampled phase and oversampled calibrated amplitude data are used to create DORIS '`.raw`' files. This is done in '`calovs_2_dorisraw.m`'. These '`.raw`' files can be used as input for the coregistration by DORIS.

8. **Create new master '`.res`' files.**

   New master '`.res`' files are created for the oversampled situation, inclucing new values for adapted parameters. For the master images this has to be performed only once in '`dorisproc_ovs_master.m`'. For the master - slave combinations this is done in '`Dorisproc_ovs.m`'. After the '`.res`' files are adapted DORIS can be run again for the oversampled situation.

The used sub-functions are:

- `B_lasvegas_patches_ovs.m`: oversampling of the data by factor 2 per patch.
- `B_readkeystring.m`: extract parameters form `.log` and `.res` files.
- `date_calibration_parameters.m`: gives the processing and acquisition date of each SAR images, to enable the use of different look-up tables.
- `Calibration_ini.m`: calculates initial parameters that can be used to calculate the range dependent correction factors for incidence angle and range spreading loss correction per pixel position.
- `Calibration_G.m`: calculates the correction factor for antenna pattern gain per pixel position.
- `Calibration_K.m`: calculates the correction factor for calibration constant K per image.

The look-up tables that are used in the calibration procedure are given in Table C.2. These files are obtained from the ESA calibration document (Laur et al., 2002):

Filename	**Description**
`Calibration_constant_K_AppendixD.txt`	look-up table for the calibration constant K.
`Elevation_antenna_pattern_gain_AppendixG2b.txt`	look-up table for the correction for antenna pattern gain for ERS-1 images, VMP Products processed after 16th July 1995 and prior to v6.8.
`Elevation_antenna_pattern_gain_AppendixG2c.txt`	look-up table for the correction for antenna pattern gain for ERS-1 images, VMP Products processed with v6.8 or later.
`Elevation_antenna_pattern_gain_AppendixG3b.txt`	look-up table for the correction for antenna pattern gain for ERS-2 images, VMP Products processed prior to v6.8.
`Elevation_antenna_pattern_gain_AppendixG3c.txt`	look-up table for the correction for antenna pattern gain for ERS-2 images, VMP Products processed with v6.8 or later.
`Powerloss_ERS1.txt`	look-up table for ERS-1 SAR ADC Power Loss Correction.
`Powerloss_ERS2.txt`	look-up table for ERS-1 SAR ADC Power Loss Correction.

Table C.2: Overview of the files that include the look-up tables of the ESA calibration method (Laur et al., 2002).